LONDON'S GLOBAL UNIVERSITY

Radiation Pressure Torque and Computational Attitude Modelling of Space Debris

Hira Singh Virdee

University College London

A thesis submitted for the degree of

Doctor of Philosophy

March 2016

I, *Hira Singh Virdee*, confirm that the work presented in this thesis is my own. Where information has been derived from other sources, I confirm that this has been indicated in the thesis.

.....

.....

Abstract

Human space activity in the past 50 years has led to a plethora of man-made space debris which pose an imminent threat to global space operations. The current models of space debris orbits are not sufficient for detailed orbit prediction or for accurate tracking. This uncertainty manifests itself in Conjunction Analysis (CA) with active spacecraft, which leads to excessive orbital manoeuvres which are both expensive and reduce the lifetime of satellites. Advances in orbit modelling will lead to better prediction of debris orbits and reduce the need for collision avoidance manoeuvres, as well as minimising the future pollution of the space environment through collisions. Most existing methods for analysing the orbits of space debris do not take into account the effects of tumbling, and the attitude-dependent non-conservative forces are generally neglected.

This study models the torques and attitude motion of uncontrolled man-made objects in orbit about the Earth, which tumble due to a combination of natural influences of the near-Earth space environment and initial angular momentum acquired during debris formation. The modelling of space debris is a relatively new field and represents a huge new area of research.

The two main branches of this thesis are (a) modelling the torques that induce spin for objects in orbit, and (b) modelling the effect of certain attitude-dependent non-conservative forces on spinning objects in orbit. The main torque modelled in this study is solar radiation pressure (SRP). Simulations of the radiation-induced torques are performed and the main mechanisms that lead to the tumbling of uncontrolled objects are analysed. A novel method of presenting attitude-dependent forces and torques on space objects, dubbed "Torque Maps", is presented. Radiation torques are caused by optical geometric asymmetry and can lead to oscillatory and secular changes in attitude. They are computed for one of the largest objects in orbit: Envisat, a defunct satellite with complex geometry.

Further to these, simulations of objects spinning in orbit are used to calculate the effect of tumbling on orbital motion. The results show that the effects of non-conservative forces on tumbling objects lead to both periodic and secular variations in their orbital elements. This is contrary to previously popular assumption. Additionally, ideas for utilising modern developments in nanosatellite technology for validation of orbit prediction models are presented and calculations of the Lorentz force and its effect for uncontrolled objects are given.

Dedication

I dedicate this thesis to my late grandfather, Sardar Kartar Singh Virdee (1913-2007). He has been my inspiration and motivation.

Acknowledgements

I'd like to thank Prof Marek Ziebart for his supervision and guidance. I am grateful to Dr Santosh Bhattarai, Dr Stuart Grey and David Harrison for their support and technical discussions. I'd also like to thank my colleagues at the Space Geodesy and Navigation Laboratory.

Finally I am grateful for the support and encouragement of my parents Tirath and Gurdeep, my siblings Mann and Mala, friends and family, and my fiancée Rashpal.

This research project was undertaken as part of USAF EOARD Grand Award Number FA8655-11-1-3043. Envisat photometric data courtesy of NERC BGS Space Geodesy Facility, Herstmonceux.

> *Bliss was it in that dawn to be alive,*
>
> *But to be young was very Heaven!*
>
> -**William Wordsworth**, 1805

> For two hundred years, satellites of all shapes and sizes, from loose nuts and bolts to entire space villages, had been accumulating in Earth orbit. All that came below the extreme elevation of the Tower, at any time, now had to be accounted for, since they created a possible hazard...
>
> -**Arthur C. Clarke**, *The Fountains of Paradise*, 1979

Table of contents

List of Figures

The following conventions are used for axis labelling in figures:

- **Red**: Cartesian x-axis
- **Green**: Cartesian y-axis
- **Blue**: Cartesian z-axis

All figures and tables generated by the author unless otherwise noted. Satellite and test object visualisations generated using a tool developed by Dr Stuart Grey.

List of Tables

Glossary, abbreviations, acronyms, constants and symbols

0.1 List of abbreviations and acronyms

ιOTA	In-Orbit Tumbling Analysis tool, a 6dof tool under development at ESA in conjunction with HTG
3dof	Three degrees-of-freedom - a translational modelling method (typically cartesian x,y,z)
3U	3 Unit, a specific form factor of CubeSat with the main bus measuring 30x10x10cm
6dof	Six degrees-of-freedom - a translational and rotational modelling method (as with 3dof but additional freedom to rotate about each axis)
AAS	American Astronautical Society
ADR	Active Debris Removal
AFRL	Air Force Research Laboratory - the research and development section of the United States Air Force
AIAA	American Institute of Aeronautics and Astronautics
AIUB	Astronomisches Institut - Universität Bern, a research group
AMR	Area-to-mass ratio
AP	Argument of Perigee
BF	Body-Fixed reference frame
CA	Conjunction Analysis
CoM	Centre of Mass
CoP	Centre of Pressure
CPU	Central Processing Unit
CUDA	Compute Unified Device Architecture
DAMAGE	Debris Analysis and Monitoring Architecture to the GEO Environment, a space debris model developed at the University of Southampton
DE405	Developmental Ephemerides 405
DRAMA	Debris Risk Assessment and Mitigation Analysis, a mission compliance tool developed by ESA
ECEF	Earth Centered Earth Fixed - a reference frame

ECI	Earth Centered Inertial - a reference frame
EGM2008	Earth Gravity Model 2008
ELaNa	Educational Launch of Nanosatellites
EOARD	European Office of Aerospace Research and Development - the European arm of AFRL
ERP	Earth Radiation Pressure
ESA	European Space Agency
ESOC	European Space Operations Centre
GEO	Geosynchronous Earth Orbit - with a semi-major axis of 42,164km / altitude 35,786km
GMAT	General Mission Analysis Tool
GNSS	Global Navigation Satellite System, for example the GPS constellation
GPGPU	General-Purpose GPU
GPS	Global Positioning System, with some 31 satellites orbiting at 26,561km
GPU	Graphics Processing Unit
HAMR	High area-to-mass ratio - defined by $\frac{A}{m} > 1m^2/kg$
HPC	High Performance Computing; at UCL, there are several HPC facilities
HST	Hubble Space Telescope, an optical telescope in orbit
HTG	Hyperschall Technologie Göttingen GmbH
IADC	Inter-Agency Debris Committee
IGRF	International Geomagnetic Reference Field - a model of the Earth magnetic field used in the scientific community
IP	Intersection Point, the point at which a ray intersects the surface of an object
ISS	International Space Station
J2	The oblateness term in the geopotential expansion of the gravitational field of the Earth
JPL	Jet Propulsion Laboratory, part of NASA
JSC	Johnson Space Centre, part of NASA
LAGEOS	Laser Geodynamics Satellite, a dense LAMR metallic ball in orbit with retroreflectors for precise positioning
LAMR	Low Area-to-Mass Ratio

LEO	Low-Earth Orbit, 150-2000km altitude. See also MEO and GEO
MASTER	Meteoroid and Space Debris Terrestrial Environment Reference, a space debris model developed by ESA
MEMS	Micro ElectroMechanical Systems - miniaturized mechanical and electro-mechanical sensors
MEO	Medium-Earth Orbit, 2000km up to GEO at 35,786km altitude
MJD	Modified Julian Date
MLI	Multi-layer insulation
MODEST	Michigan Orbital DEbris Survey Telescope
MSG2	Meteosat Second Generation 2 - the second satellite launched in the MSG program
NASA	National Aeronautics and Space Administration
N/C	Non-conservative force
NERC-SGF	National Environment Research Council - Space Geodesy Facility, a satellite observation and ranging facility in East Sussex
NORAD	North American Aerospace Defense Command
OF	Orbit-Fixed reference frame
ORDEM	ORbital Debris Engineering Model, a space debris model developed by NASA
PCB	Printed Circuit Board
RAAN	Right Ascension of the Ascending Node
RK	Runge-Kutta
SGNL	Space Geodesy and Navigation Laboratory
SLR	Satellite Laser Ranging
SRO	Space-Resident Object
SRP	Solar Radiation Pressure
SSA	Space Situational Awareness, the field dealing with the modelling of objects in orbit around the Earth including their orbit and the future projection of their position and status
SSO	Sun Synchronous Orbit
TED	Technology, Entertainment, Design
TLE	Two-Line Element (can also mean Three-Line Element)

TRL	Technology Readiness Level: NASA define TRLs based on Figure 0.1. These indicate the maturity and level of particular projects or research. This thesis is aimed at TRL 1-3.
TRR	Thermal Re-Radiation
UCL	University College London
USAF	United States Air Force

0.2 Glossary

6dof Six degrees-of-freedom, a modelling system which simulates three degrees of translational and three degrees of rotational motion

Area-to-Mass Ratio $\frac{area}{mass}$: A measure of how significant non-conservative forces (usually dependent on area) are in comparison to conservative forces (usually dependent on mass)

Attitude modelling Prediction of the rotation and tumbling of objects, in order to find the evolution of their spin rate and axis

Conjunction analysis The propagation of individual object orbits in order to predict when collisions might occur. The main reason for this is to prevent early termination of a mission due to a collision, but a secondary reason is to prevent collisions that may lead to the Kessler syndrome.

Conservative force Forces for which the balance between potential and kinetic energy is reversible - for example, gravity

CubeSat CubeSats are small satellites (10x10x10cm main body, mass $< 1.33kg$) intended to open the space environment up to education and research at a much lower cost of entry. They are launched as secondary payloads to large commercial missions.

Envisat This was an Earth observation satellite, launched in 2002 and active until 2012. At $8211kg$, it is one of the largest uncontrolled objects in orbit and is known to be tumbling, making it an object of great interest in the SSA community and to the broader space community.

Force modelling The technique of calculating the distinct forces acting on an object in orbit, in order to predict the future evolution of an objects position and velocity

HAMR HAMR objects have a large area in relation to their mass. As

	a subset of space debris, these objects are impacted more by non-conservative forces which are typically area-dependent, compared to the conservative forces which typically depend on mass. HAMRs are defined by $\frac{area}{mass} > 1m^2/kg$.
Kessler syndrome	Following a major collision in space, the fragments can collide with other objects leading to a cascading runaway chain reaction of collisions that could quickly disable many operational satellites
Kicksat	A crowdfunded project to send 300 single-PCB nanosatellites into orbit, led by students at Cornell university
MSG2	An Earth observation satellite. In this projects, references to MSG2 are to the cooler cover ejected from the satellite which has HAMR properties and which also has well-defined initial conditions making it an ideal object to study
Nanosatellite	In this thesis, nanosatellite is used to describe any small satellite; particularly single-PCB satellites. There are differing definitions, some with $m = 1 - 10kg$ for nanosatellites. Single-PCB satellites typically have $m < 0.1kg$.
Non-conservative force	These forces transfer energy irreversibly, most often to heat - examples include Solar Radiation Pressure (SRP), Earth Radiation Pressure (ERP), aerodynamic drag and the Lorentz force
Pixel array	This method enables a high-precision ray-tracing approach for predicting the radiation pressure forces on an object of arbitrary shape
Radiation pressure	Photons impinging upon the surface of an object transfer momentum based on special relativity and the *de Broglie* equations. This transfer of momentum results in a force which is dependent on the area illuminated, known as radiation pressure.
Ray tracing	A technique which involves tracing the path of light through

	pixels in a plane and simulating their encounters with an object
Space debris	Any manmade objects in the near-Earth space environment which are no longer controlled, and hence their motion is subject to the natural influences of the space environment
Space Resident Object	Any object in near-Earth orbit, including both active and inactive satellites and space debris
Space Situational Awareness	The field of research which deals with cataloguing the contents of near-Earth space, how they are moving and their future position and motion
Torque map	A method for visual presentation of the torques exerted about a particular axis of an SRO, enabling quick insight into a complex array of data
Tumbling	The spinning and evolution thereof, for an object in space

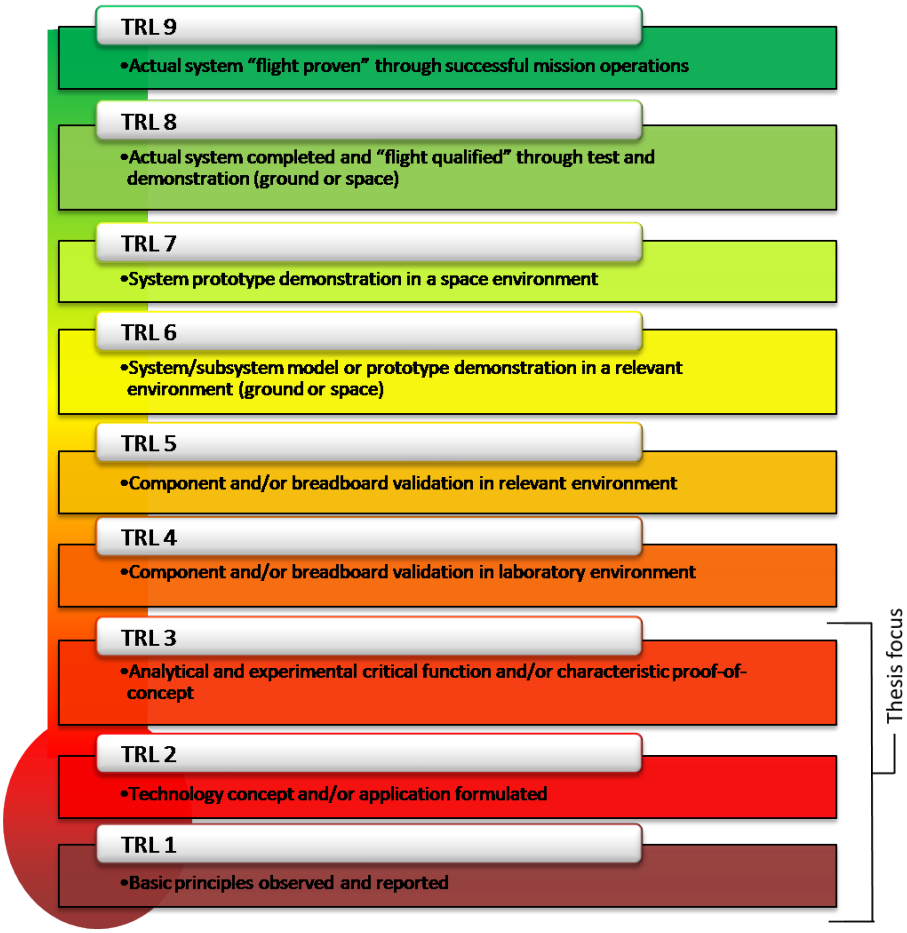

Figure 0.1: Technology Readiness Levels as defined by NASA [1]

.

0.3 List of constants

GM Gravitational constant, $= 398600.44\,km^3s^{-2}$

σ Stefan-Boltzmann constant$= 3.67 \times 10^{-8}\,Jm^{-2}s^{-1}K^{-4}$

a_E mean radius of Earth$= 6378.137\,km$

c speed of light in vacuum $= 299792458.0\,ms^{-1}$

E irradiance$= 1364\,Wm^{-2}$

0.4 List of symbols

α material absorptivity, $(1 - \nu)$

ϵ_{eff} effective emissivity

ϵ_{MLI} emissivity of MLI

$\hat{n}$ Surface normal vector

$\hat{s}$ In-plane vector, in the shear direction

μ material surface specularity

ν material surface reflectivity

Ω Right ascension of the ascending node

ω Argument of perigee

$\rho(\vec{r})$ Mass density (kgm^{-3})

θ angle of incidence between incoming ray and the surface normal

$\vec{\tau}$ Torque vector; torque about x, y and z-axes respectively (Nm)

$\vec{B}(\vec{r}, t)$ geomagnetic field strength vector, T

$\vec{F}$ Force (N)

$\vec{F}_L$ Lorentz force (N)

$\vec{r}_{COM}$ position of the centre of mass in the spacecraft body frame

$\vec{r}_{COP}$ position of the centre of pressure in the spacecraft body frame

$\vec{r}_{IP}$ position of the intersection point in the spacecraft body frame

a Semi-major axis (km)

A area illuminated

a_L Lorentz acceleration vector, ms^{-2}

B magnetic field strength vector, Tesla

e	eccentricity
E	electric field vector, Newtons per Coulomb (NC^{-1})
I	moment of inertia, kgm^2
i	inclination of the orbital plane
M	Total mass
$P_n^m(\theta)$	associated Legendre polynomial of degree n and order m
q	surface charge, Coloumbs (C)
v	velocity vector, ms^{-1}
$V(\vec{r}, t)$	scalar gravity field potential function, Vsm^{-1}
$\vec{r}(t)$	position vector m

1 Introduction

This study deals with the problem of modelling the orbit and attitude motion of uncontrolled man-made objects in orbit about the Earth, which tumble due to the natural influences of the near-Earth space environment. A mathematical, physics-based and computational approach is taken to model the forces and torques that drive the orbit and attitude evolution of such objects. The main influence modelled here is solar radiation pressure (SRP), which is the interaction of solar electromagnetic radiation with the surface of an object, and which leads to both forces and torques that influence the orbital and attitude motion. Other influences, such as the gravitational field of the Earth, are also modelled.

This thesis develops a method for modelling the torque and attitude on uncontrolled objects, extending previous methods for force modelling and orbit prediction to include tumbling. The reasoning behind this is threefold:

- to set a framework for computational attitude modelling, also known as a 6 degrees of freedom (6dof) model; the six degrees of freedom are three translation and three rotation
- to improve orbit prediction through better application of non-conservative forces which are attitude-dependent, and
- to better predict an acquisition window for an uncontrolled object being observed from a ground tracking station, as observability is attitude-dependent.

The primary contribution of this work is the extension of the pixel-array computational method, for radiation pressure force modelling, to calculate radiation pressure torques. The secondary contribution is the computational propagation of tumbling motion, embedded within a full orbit simulation. There are additional contributions to the field of Space Situational Awareness (SSA), such as suggestions for tracking and validation using nanosatellites and computation of the Lorentz force.

1.1 Motivation

> Clear skies with a chance of satellite debris.
>
> -**Ryan Stone (Sandra Bullock)**, *Gravity*, 2013

Modern society has become heavily reliant upon space technologies for a wide variety of services, including communication, banking, weather prediction, Earth observation and global positioning [16]. Since the first manmade satellite became operational in 1957 [17], there have been over 5000 space launches [18] which have resulted in a plethora of both operational and non-operational Space Resident Objects (SROs). The evolution of the number of SROs is visualised in Figure 1.1. The current constellation of over 1000 operational satellites [19] is at serious risk of collision with some 20,000 large space debris and countless smaller debris [20, 21]. A rendered image of the active satellites and all catalogued debris is given in Figure 1.2. In the event of a few collisions, a cascading runaway effect could lead to the rapid cluttering of near-Earth space which would cause collisions and breakup of many active satellites in a short space of time. This is known as the Kessler syndrome [22]. The broad field which deals with the observation and modelling of the near-Earth space environment is known as SSA.

Before decisions can be made as to a method for the remediation of this problem, the current scenario must be better understood. This part of the problem can be approached in two ways: through observation, and through modelling. The former utilises recent improvements in remote sensing techniques such as Satellite Laser Ranging (SLR) [23], bistatic radar [24], optical observation networks [25, 26] and potentially space-based observation [27], which enable more accurate tracking of the contents of near-Earth space. The latter involves taking such observations and applying laws of physics to predict the future movements of debris, and then comparing these predictions to later observations for validation of the modelling techniques. The two approaches must be combined to give accurate predictions on what will happen in the future, and such a combination of observation and modelling is crucial in finding how to minimise the impact of space debris on the

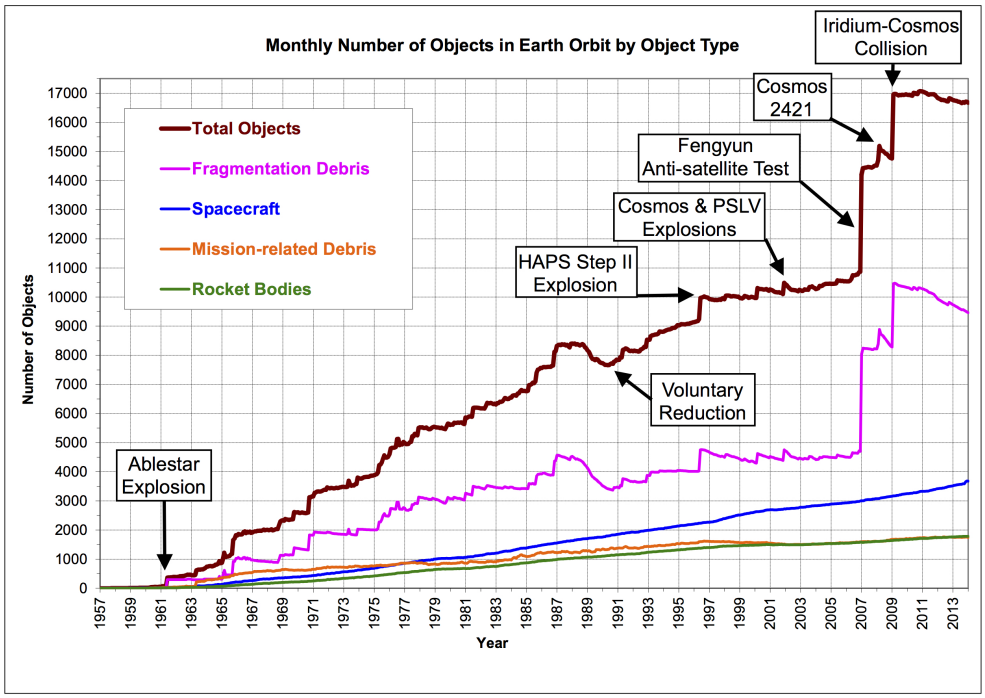

Figure 1.1: An historic graph of the quantity of objects in orbit with a characteristic size above $10cm$; figure courtesy NASA Orbital Debris Quarterly Newsletter [2].

near-Earth space environment. Failure to deal with this problem could lead to a widescale breakdown of global infrastructure with dramatic impact to modern society.

This is widely recognised as a growing problem [20, 21, 28, 29, 30]. Finding the contents of near-Earth space and how they are moving is a difficult task - primarily due to the large number of physically similar objects and the vast volume within which these objects are orbiting.

The problem of SSA has been highlighted as a key issue for future space activity, both by the United States Air Force (USAF) [31] and by the European Space Agency (ESA) [32, 33]. Initiatives such as ESA CleanSpace [34] will lead to Active Debris Removal (ADR), which aims to de-orbit larger debris to prevent further cluttering of near-Earth space. ESA aim to remove Envisat around 2021 as part of the CleanSpace initiative [35], as it is a large and heavy satellite and so poses a significant risk for collision and cluttering of near-Earth space. Understanding of its tumbling motion is of the utmost importance for such a mission to be successful.

The current predictions for the future evolution of space debris orbits are based

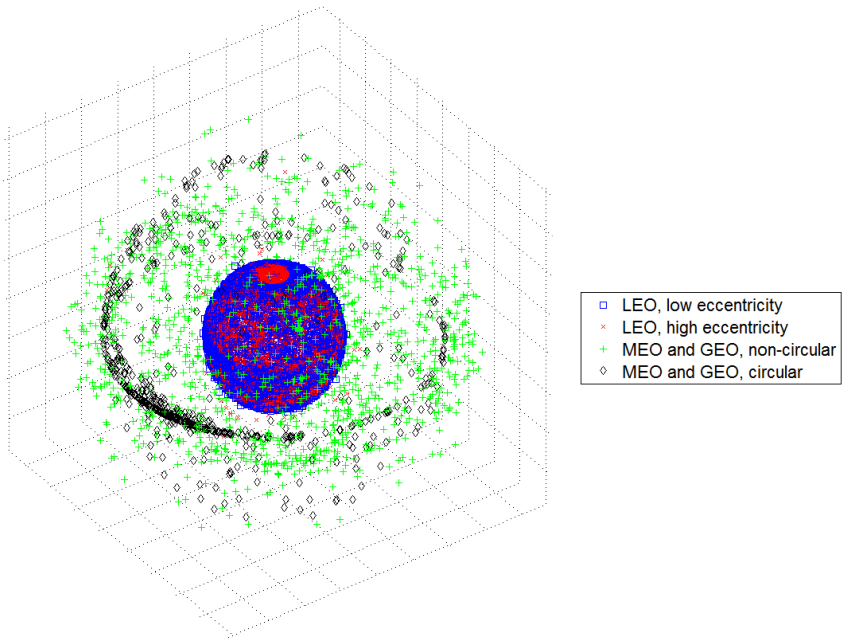

Figure 1.2: A plot of the debris catalogue from the SpaceTrak database, coloured by orbit type

on simple force models and analytic studies of tumbling. A gap in the current research on this problem is the modelling of attitude for specific objects with a rigorous physics-based method; the gaps in current research are outlined in Chapter 3.

1.2 Preliminary problem statement

This thesis works towards the calculation of radiation-induced torques on SROs of generic shape, and also analyses the effect of tumbling on the evolution of parameters that describe orbits. The problem statement is given in detail in Chapter 4.1, and broken down into specific aims and objectives, after a brief scientific introduction to the field (Chapter 2) and in the context of prior research in the field, as presented in Chapter 3.

1.3 Thesis outline

The problem of modelling the orbits of space debris must be tackled in stages. The structure of this thesis reflects the progressive stages of research involved in conducting the study. It begins with a broad introduction and context of the problem of space debris in Chapter 1. This is followed by an overview of the scientific theory required to understand the previous research in the field in Chapter 2. A review of previous studies of the problem of space debris (historic to present day state-of-the-art) is given in Chapter 3, and gaps in prior studies are also described. These lead into the problem statement which gives detailed aims and objectives for the research in Chapter 4.1. Based on the context, previous work and objectives of research, the methods developed to fulfil the aims are presented in Chapter 4. The verification of the method using basic test objects and initial results are presented in Chapter 5. This leads into the key results of the devised methods in Chapter 6 which gives their application to test scenarios. Chapter 7 gives additional studies that have been undertaken as part of this research, but which are not part of the main two paths of research. The real-world application of the results is discussed in Chapter 8. Finally, a summary of the thesis is given along with overall conclusions in Chapter 9. The appendices (Chapter 9.3.4) contain contributions to the field in the form of papers presented.

2 Scientific background

Chapter outline

This section starts with a more detailed motivation and background than in the introduction. The broader theory behind the research is then presented, with a focus on details surrounding the method that is given in chapter 4.

2.1 Space Situational Awareness

Space situational awareness is the field of research which aims to catalogue the contents of near-Earth space and to predict how this constellation of objects will evolve. This encompasses observation, orbit determination, orbit prediction and conjunction analysis for the purpose of collision avoidance in space operations. Klinkrad 2006 [36] is a good resource for a detailed description of models surrounding every aspect of space debris analysis, including debris generation pathways, legal ramifications, international guidelines on mitigation and conjunction analysis.

2.1.1 A brief history of space debris

Since 1957, with the launch of Sputnik 1, humankind has left a heavy footprint on the near-Earth space environment. Space debris comprises the set of man-made objects in orbit about the Earth which are no longer under human control. These include defunct satellites, fragments of satellites and mission-related objects which have been discarded.

The problem of manmade space debris was first recognised in the 1970s [37]. This was a time of intense and ambitious space technology development, with cold war achievements being a matter of national prestige. Space programs sought to uphold national honour above all, and budgets were aligned with these aims. There was little consideration of the consequences of such activity [29].

This period of high space activity led to a rapid deterioration of the near-Earth environment. A series of collisions and explosions between 2000-2010 further exacerbated the problem and led to the current scenario which is described in Table 2.1, and which was graphed in Figure 1.1. Space technologies underpin most

aspects of modern society, from communication and banking, infrastructure and transport, through farming and weather prediction amongst others.

The risks to modern satellite infrastructure from space debris are severe [38]. Due to the wide variety of objects in a broad range of orbits, this problem currently has no solution. Active satellites including the International Space Station (ISS) perform routine orbital maneuvers to avoid space debris, and these are becoming more frequent; see Figure 2.1.

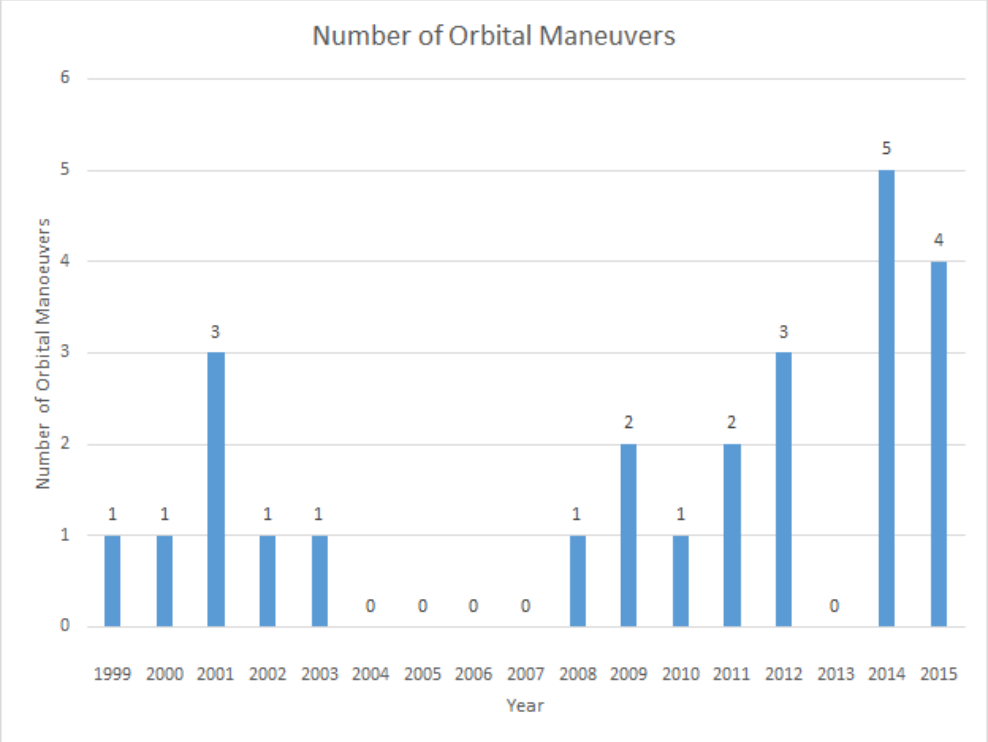

Figure 2.1: A graph of International Space Station (ISS) collision avoidance manoeuvres 1999-2015. Data courtesy NASA Orbital Debris Quarterly Newsletter [2]

Debris size	Number of objects	Total mass in orbit (kg)
0.1-1cm	170,000,000	25,000
1-10cm	740,000	50,000
10cm+	29,000	6,500,000

Table 2.1: Estimates of orbital debris populations categorised by size; number of objects courtesy [11] and total mass courtesy ESA MASTER software and [12]

Space debris is generated through three main pathways [36]:

1. Operational and mission-related debris - for example, instrument covers, explosive separation bolts and tools dropped by astronauts
2. End-of-life debris and defunct satellites - for example, Envisat, which is a complete satellite still in orbit but without communication or control
3. Unplanned debris, from explosions and collisions - for example, the debris from the Fengyun-1C anti-satellite weapons test or from the Iridium-Cosmos collision

Each of these pathways leads to debris with a particular and distinct set of physical characteristics. Mission-related debris are small in size and in number, end-of-life debris are small in number but usually large in size, and accidental/unplanned debris vary widely in size and are high in number. Each type of debris must be dealt with differently both from the perspective of spacecraft shielding design and for the design of capture and de-orbiting mechanisms. It is also worth noting that tumbling is an important consideration for rendezvous and capture of any Active Debris Removal (ADR) systems - the way an SRO is tumbling determines what methods can be used to physically capture it.

The size of space debris is given by a single number representing its characteristic size, defined by the sum of its dimensions:

$$Size = \frac{height + width + depth}{3} \tag{1}$$

This research focuses on manmade debris with a size over $10cm$, as these are observable from ground-based tracking stations and they also pose the greatest threat to space operations. This is because there are so many objects of this size that collision avoidance manoeuvres would be too frequent and costly, and yet debris of this size cannot be shielded against due to the high momentum carried at orbital speeds (typically kilometers per second). Also, a large proportion of the total orbital debris mass is contained in this part of the constellation ($10cm+$), and so collisions between objects of this size would lead to high quantities of resulting debris.

There have been recent proposals to classify space debris based on their physical characteristics [39]. One such classification is based on the area-to-mass ratio of objects. High-area-to-mass (HAMR)[1] objects are perturbed more by non-conservative forces[2] and are therefore well suited to computational analysis using the suite of surface force models developed over many years at UCL [40, 41, 42, 43, 13]. Objects from each size category of debris can be HAMRs - for example, a small paint fleck all the way up to a large sheet of multi-layer insulation (MLI). Models which predict HAMR SRO dynamics correctly are also suitable for other classes of object. Non-conservative forces are important in the studies of the debris constellation because by the very nature they change the overall mechanical energy of components of the system, thereby introducing secular variations to the orbital elements. Motion dominated by conservative effects may oscillate, but it is less prone to cause orbital decay and hence drift into other operational spaces. The HAMR debris population was first observed by Schildknecht *et al.* [44]. Given the sheer quantity of objects and the limited resolution of sensors, accurate area-to-mass ratios are difficult to obtain [45]; observational studies and their conclusions are covered in Section 3.1.1. The following sections describe the physics behind modelling the orbit and attitude of debris.

2.2 Astrodynamics and orbital mechanics

The theory of orbital mechanics started with Johannes Kepler's analysis of the astronomical observations of Tycho Brahe. A more general treatment of mechanical forces was given in Isaac Newton's Principia Mathematica in 1687. This contained the three basic Newtonian laws of motion:

1. An object remains at rest unless acted upon by a force $\vec{F}$. An object in motion remains in motion at a constant velocity unless there is an external force.
2. The acceleration $\vec{a}$ of a body is directly proportional to, and in the same direction as, the net force acting on the body; that is, $\vec{F} = \frac{\partial \vec{p}}{\partial t} = m\vec{a}$

[1] HAMR objects are defined by $(\frac{area}{mass} > 1m^2/kg)$

[2] Non-conservative forces include Solar Radiation Pressure (SRP), Thermal Re-Radiation (TRR), Earth Radiation Pressure (ERP), aerodynamic drag and the Lorentz force

(under the assumption that mass remains constant)

3. When two bodies interact, the force on each body is equal in magnitude and opposite in direction

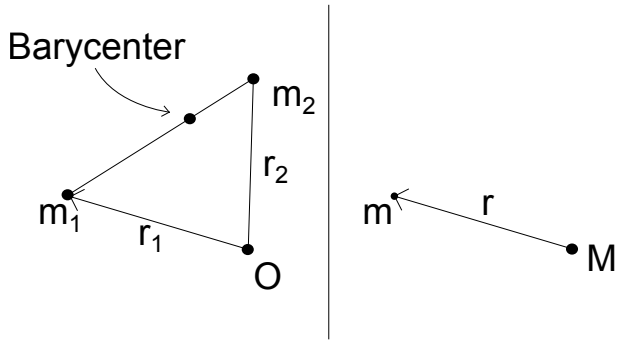

Figure 2.2: The two-body problem.

The left diagram shows the full two-body problem with two interacting masses. This problem is greatly simplified under the assumption of a large mass M at the origin, influencing a much smaller mass m, as shown on the right; $M >> m$.

Applying these laws to the interaction of two masses is known as the two-body problem. This is the interaction of two masses m_1 and m_2, as shown in Figure 2.2. For modelling SROs, the assumption $M \gg m$ where M is the mass of the Earth, and m is the mass of the SRO simplifies the problem greatly. This is because we can place the larger mass at the origin of the inertial reference frame and thus reduce the problem from that of two moving objects to a stationary object with the less massive in orbit. The most massive objects in orbit, such as the ISS, weigh $10^7 kg$, compared to the Earth at $6 \times 10^{24} kg$ so this assumption is reasonable [46].

The observations described by Kepler can be derived from Newton's laws. Kepler's laws are:

1. Gravitational orbits are elliptical with the more massive body at one of the foci
2. The line from the smaller to the more massive body sweeps out equal areas in equal time intervals (a corollary of this is that the object speed is greater when it is closer to the large body). This is shown in figure 2.3
3. The square of the orbital period is proportional to the cube of the semi-major axis of its orbit (that is, $T^2 \propto a^3$ or more completely $T^2 = \frac{4\pi^2}{GM} a^3$ for an Earth-orbiting satellite)

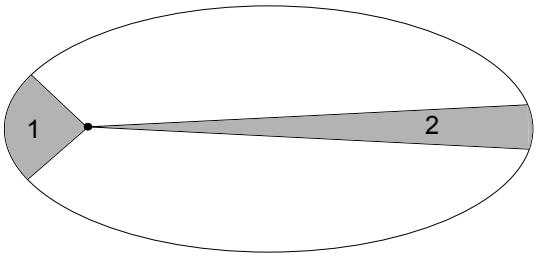

Figure 2.3: Kepler's Second Law
As the SRO gets closer to the Earth, its velocity increases and as a result, the area swept out in a fixed time interval stays constant. The shaded regions 1 and 2 have the same area.

These are the first-order starting point of any physics-based analysis of satellite orbits. A first order monopole gravity model describing the force of gravity on a small mass m in the vicinity of a large point mass M, is given by:

$$\vec{F_g} = -\frac{GMm}{|\vec{r}|^3}\vec{r} \tag{2}$$

We can use the monopole gravity model to find the elliptical orbit of a satellite around a central body. At any point we can use the object's position to calculate the gravitational force and thus the gravitational acceleration, and use this along with the object velocity to predict the resultant motion [47].

Of course, gravity is not the only force acting on an SRO. There are many forces which must be modelled in order to accurately predict the future motion of an SRO. These include:

- Atmospheric drag, to model interactions with sparse molecules of air and plasma around the Earth
- Higher-order gravity terms to account for the oblate spheroid shape of the Earth and other departures from a point mass model
- Third-body gravity terms for the Sun, Moon, and some other planets
- Radiation pressure, from the Sun and from the Earth, whereby the reflection or absorption of photons yields a net momentum transfer
- Electromagnetic interactions - forces on charged objects moving within magnetic field of the Earth

In astrodynamics, the complexity of the physical models involved in orbit pre-

diction and orbit determination preclude the use of analytical solutions of the respective differential equations. Indeed, only the classical two-body problem and some restricted classes of three-body problems can be solved in that way. For any detailed assessment of orbital dynamics, it is necessary to utilise numerical techniques.

Given a first-order differential equation:

$$\frac{dy}{dx} = y' = f(x, y) \tag{3}$$

and initial conditions

$$y'_0 = f(x_0, y_o) \tag{4}$$

there are numeric methods to obtain the value of y at other points. The differential equation which needs to be solved for orbital dynamics is of the form

$$\frac{d\vec{v}}{dt} = f(\vec{r}, \vec{v}) \tag{5}$$

where $\vec{v} = \frac{d\vec{r}}{dt}$.

Due to the two time-derivatives involved, a second integration step is required. A method for computing the solution to a differential equation is the Runge-Kutta integrator. This uses intermediate points within a single step to better approximate the function at the end of the step. The order p of a Runge-Kutta integrator describes the order of magnitude of the error term:

$$y_{n+1} = y_n + \sum_j c_j k_j + O(h^{p+1}) \tag{6}$$

where c_j are the fractional coefficients, k_j are the terms which evaluate the differential equation, and h is the step size. The common fourth-order method is shown in Figure 2.4 and the equations used are given in Equations 7-**??**.

$$y_{n+1} = y_n + \frac{h}{6}(k_1 + 2k_2 + 2k_3 + k_4) \tag{7}$$

$$x_{n+1} = x_n + h \tag{8}$$

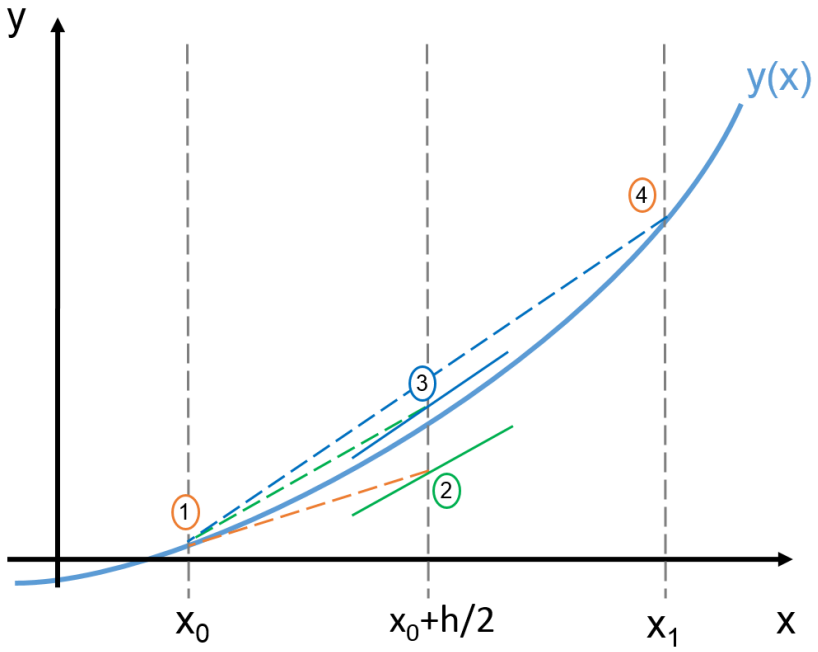

Figure 2.4: Runge-Kutta fourth-order method for numeric integration

$$
\begin{aligned}
k_1 &= f(x_n, y_n) \\
k_2 &= f(x_n + \frac{h}{2}, y_n + \frac{h}{2}k_1) \\
k_3 &= f(x_n + \frac{h}{2}, y_n + \frac{h}{2}k_2) \\
k_4 &= f(x_n + h, y_n + hk_3)
\end{aligned}
\tag{9}
$$

2.3 Describing an orbit

2.3.1 Keplerian elements

There are many ways to represent the orbit of an object; two of the most widely used are Cartesian position (xyz) and velocity (uvw), and Keplerian elements ($aei\omega\Omega\nu$).

Cartesian position and velocity are useful in computational methods, as they lend to computing the force on an orbiting object at a given point in its orbit, and then propagating to the next position and velocity.

For a simple orbital model using a monopole gravitational force, the orbit is elliptical. Keplerian elements are a description of the size and orientation of this ellipse, as well as the position of an object on the ellipse.

The six elements, as shown in Figure 2.5, can be split into three groups. The first two define the size and shape of the ellipse:

- a, semi-major axis (km). This gives the size of the ellipse
- e, eccentricity (dimensionless). This gives the elongation of the ellipse compared to a circle

The next two give the orientation of the orbital plane with respect to the reference plane (usually the Earth's orbital plane around the Sun):

- i, inclination (degrees). This gives the angle between the orbital plane and the equatorial plane
- Ω, Right ascension of the Ascending Node (degrees), the angle from a reference direction (the Point of Aries) to the point at which the satellite moves from the Southern Hemisphere to come above the Earth-Sun plane

The last two give the orientation of the ellipse within the orbital plane, and the position of the orbiting object on the ellipse for the given epoch.

- ω, argument of perigee (degrees).
- ν, true anomaly (degrees).

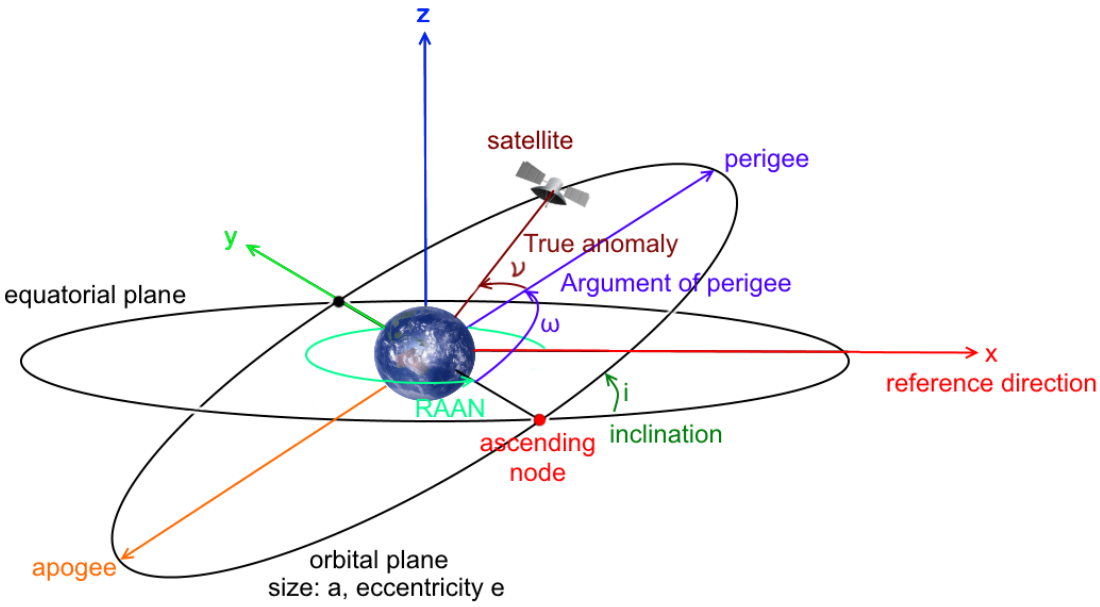

Figure 2.5: A diagram of the six Keplerian elements required to describe an orbit of a satellite

2.3.2 Two-Line Elements (TLEs)

Catalogues of Keplerian elements for the known objects orbiting the Earth are maintained. The main catalogues are given in a format known as Two-Line Element (TLE) sets. The format is summarised in Table 2.2. The format gives the satellite epoch data in the first line, and the Keplerian elements are given in the second line. An example of the TLE as it would appear in a data file is given in Table 2.3 along with sample data for the International Space Station (ISS).

It is worth noting that there are a number of limitations to the TLE data format. The data format was initially written in the 1960s when computer memory and data transmission limitations were severe. The limitations on data storage and transmission are trivial on modern computers, but the data format remains as the astrodynamics community gradually built their software around it.

The main limitation of a TLE is the Simplified Perturbations Model which is used to generate a TLE orbits from observations. The initial orbit determination error is $1km$ and this error grows by $1-3\,km$ per day [48]. This necessitates

Line / Field	Columns	Content	Example
1 / 1	01-01	Line number	1
1 / 2	03–07	Satellite number	25544
1 / 3	08–08	Classification (U=Unclassified)	U
1 / 4	10–11	International Designator (Last two digits of launch year)	98
1 / 5	12–14	International Designator (Launch number of the year)	067
1 / 6	15–17	International Designator (Piece of the launch)	A
1 / 7	19–20	Epoch Year (Last two digits of year)	08
1 / 8	21–32	Epoch (Day of the year and fractional portion of the day)	264.51782528
1 / 9	34–43	First Time Derivative of the Mean Motion divided by two	- .00002182
1 / 10	45–52	Second Time Derivative of Mean Motion divided by six (decimal point assumed)	00000-0
1 / 11	54–61	BSTAR drag term (decimal point assumed)	-11606-4
1 / 12	63–63	The number 0 (Originally this should have been "Ephemeris type")	0
1 / 13	65–68	Element set number. Incremented when a new TLE is generated for this object.	292
1 / 14	69–69	Checksum (Modulo 10)	7
2 / 1	01–01	Line number	2
2 / 2	03–07	Satellite number	25544
2 / 3	09–16	Inclination [Degrees]	51.6416
2 / 4	18–25	Right Ascension of the Ascending Node [Degrees]	247.4627
2 / 5	27–33	Eccentricity (decimal point assumed)	0006703
2 / 6	35–42	Argument of Perigee [Degrees]	130.5360
2 / 7	44–51	Mean Anomaly [Degrees]	325.0288
2 / 8	53–63	Mean Motion [Revs per day]	15.72125391
2 / 9	64–68	Revolution number at epoch [Revs]	56353
2 / 10	69-69	Checksum (Modulo 10)	7

Table 2.2: The TLE data format, with example values for the ISS

```
1 25544U 98067A 08264.51782528 -.00002182 00000-0 -11606-4 0 2927
2 25544 51.6416 247.4627 0006703 130.5360 325.0288 15.72125391563537
```

Table 2.3: An example of a Two-Line Element for the International Space Station

a continuous update of TLEs from new observations. TLEs are considered to be valid for a few days to a few weeks [49]. This is because the effect of all orbital perturbations cannot be represented accurately by a small set of numbers such as those given in TLEs.

Other limitations of the format include:

- Year of launch. This is given in line 1 field 4 in the International Designator (see table 2.2). As this is given as two numbers in the YY format, problems will arise in the future in distinguishing between 1957 and 2057, for example.
- Limited catalogue size. The satellite number field (line 1 field 2) is limited to 99,999 objects. This is not a large enough catalogue to store information about smaller debris objects, under 10cm.
- The International Designator gives upto 999 launches per year in line 1 field 5. This is sufficient for current launches, as the maximum number of launches in a given year was 129 in 1984. This might not be sufficient in the future, or to track space debris generation events.

The semi-major axis of an orbit is calculated from the mean motion using Kepler's third law as follows:

$$a = \left[\frac{GM}{(2\pi n)^2}\right]^{1/3} \tag{10}$$

where n is the mean motion. The true anomaly can be calculated from the mean anomaly [4], and the other Keplerian elements are given explicitly in the TLE.

The abbreviation TLE can also refer to three-line elements, whereby an extra initial line gives a text description of the satellite. For the example TLE given, the initial line is "`ISS (ZARYA)`". For computational analysis, this line is used to identify an object in a more user-friendly way or simply discarded. A quantitative analysis of the current debris constellation is given in Section 2.4.

2.4 Current space debris catalogue

There are several current catalogues of the space debris constellation, which amalgamate data from many observation sites. The main catalogues, as tracked by NORAD, are maintained in TLE data sets through the SpaceTrack [3] and CelesTrack [4] databases. These give the Keplerian elements of some 14,500 orbital objects. This data gives a good indication of the coarse orbital regimes where debris poses a threat to operational space. TLEs are, however, of severely limited use for precise orbit prediction - there is simply not enough information contained in such simple elements to make full use of the high fidelity of current models. The limitations of this data format were discussed in Section 2.3.2. The TLEs lack information on object size, shape and mass which are all necessary for advanced force and torque modelling. These limitations mean that this data is primarily suited to crude long-term simulations (months to years), where the data is used to get an idea of the future scenario, rather than a precise orbit to be compared to future observations or for the purpose of tracking objects. For the short-term simulations (days to weeks), it is better to use direct observations or to use many historic TLEs to extract more precise orbital elements and the underlying orbital data.

This data was rendered as shown in Chapter 1: Figure 1.2. For quantitative analysis of the information that is contained within the obtained TLEs, a set of histograms were plotted. The first of these was to get an idea of which SROs are described by the dataset. As the obtained elements have three lines, the description line was extracted and a word cloud plotted. This is given in Figure 2.6. The size of the font gives an indication of the frequency of appearance of a given word in the dataset.

The most frequent entry is “DEB” which indicates a piece of debris. This is followed by “COSMOS” and “FENGYUN 1C”, both of which indicate fragments of satellites which exploded whilst in orbit. The orbits of these are given in Table 2.4.

[3] https://www.space-track.org
[4] http://celestrak.com

Figure 2.6: A word cloud of the text contained in the description line of the TLE database

Satellite	Semi-Major Axis (km)	Eccentricity	Inclination (deg)	RAAN
Cosmos	7161	0.0018	74.00	283.7
Fengyun 1C	7210	0.0015	99.00	102.7

Table 2.4: The orbits of the Cosmos and Fengyun-1c satellites prior to collision/explosion

The next most common entry is “R/B” which are rocket bodies - these are also debris but are not included in the set labelled “DEB”. The rocket bodies are generally larger than the other debris and have much shorter orbital lifetimes. The next most common entries such as “DELTA”, “ARIANE”, “SL-8”, “SL-16” and “CZ-4” are types of launch vehicle and rocket used to put satellites into orbit. The DELTA rocket system appears more frequently due to a combination of a greater number of DELTA launches compared to other rockets, and a couple of rocket explosions causing debris.

There are 3,681 unique object types amongst the 14,586 in the database. The twelve most common of these are given in Figure 2.7. It is noteworthy that the

number of tracked pieces of debris from the collision of the Iridium and Cosmos satellites is different - there are 1323 tracked objects from the Cosmos-2251 satellite but only 459 from Iridium-33. This is most likely because of the difference in weight between the two satellites - Cosmos-2251 weighed 900kg whereas Iridium-33 weighed 689kg. Both the word cloud and the bar chart are included as the word cloud highlights visually which categories are prominant in the dataset, and the bar chart gives a numeric breakdown.

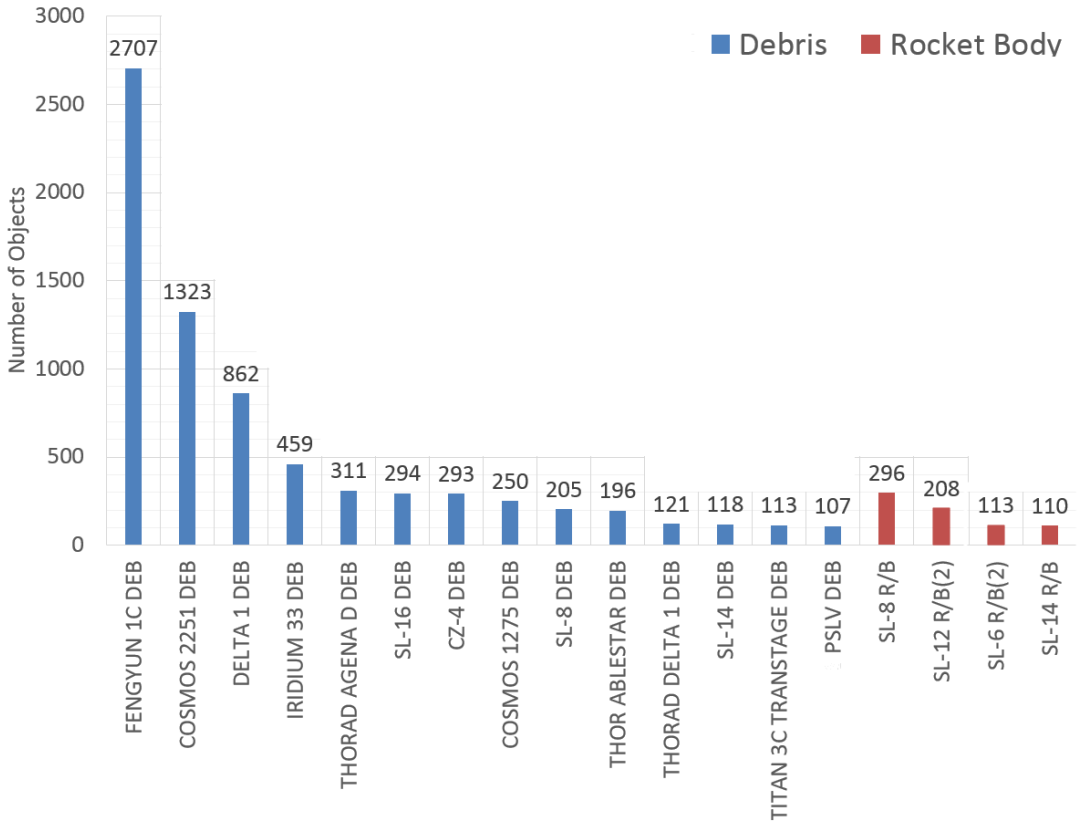

Figure 2.7: A bar chart showing the most common SROs in the TLE database, coloured by object type

Histograms were plotted to visualise the distribution of orbital element data contained in the TLE dataset. These are given in Figures 2.8 through 2.11. The majority of objects are in near-circular low-Earth orbits, as shown by the large numbers of objects with low semi-major axis and low eccentricity in Figures 2.8 and 2.9. They are predominantly in highly inclined orbits, with inclinations from 60-100° as seen in Figure 2.10. There also seems to be a trend in the orientation of

the orbital planes, as shown in Figure 2.11. This Figure shows that more objects enter the northern hemisphere in the 180° to the east of Greenwich than in the 180° to the west of Greenwich. This could be due to collision events in some orbital planes of this orientation. The argument of perigee distribution is near-uniform (Figure 2.12). The distributions are corroborated by other analyses as given in Figure 2.13.

This distribution of objects influenced the choice of test object - one LEO and one near-GEO object were chosen as a reflection of areas of dense debris population and to reflect areas of particular interest and importance to the space community.

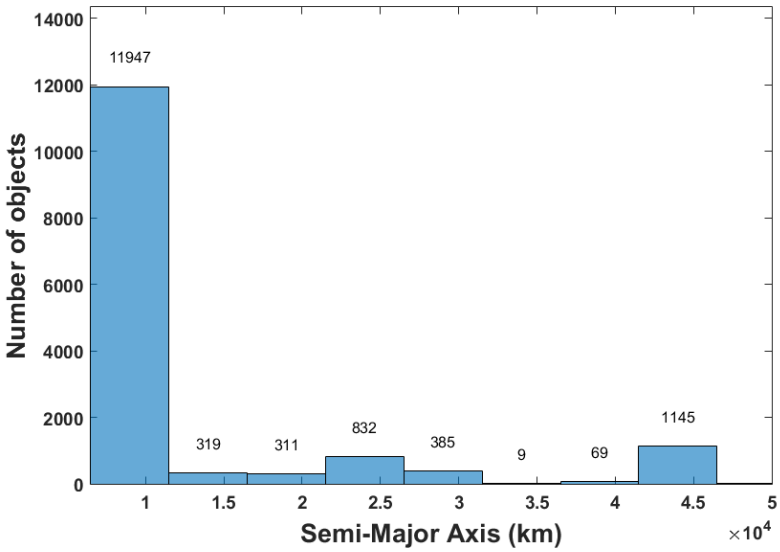

Figure 2.8: A histogram of the distribution of semi-major axes in the TLE database. The majority of objects are in LEO (100-2000km altitude / 6471-8371km semi-major axis). There are further groups at MEO (16,000-20,000km altitude / 22,371-26,371km semi-major axis) and finally a group at GEO (36,000km altitude / 42,371km semi-major axis)

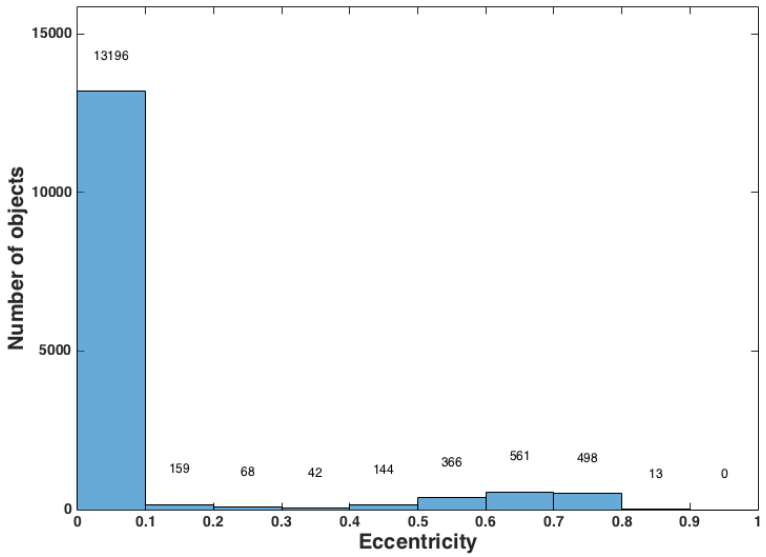

Figure 2.9: A histogram of the distribution of eccentricities in the TLE database. The majority are in circular and near-circular orbits, with a smaller group of objects in the range e=0.5-0.8

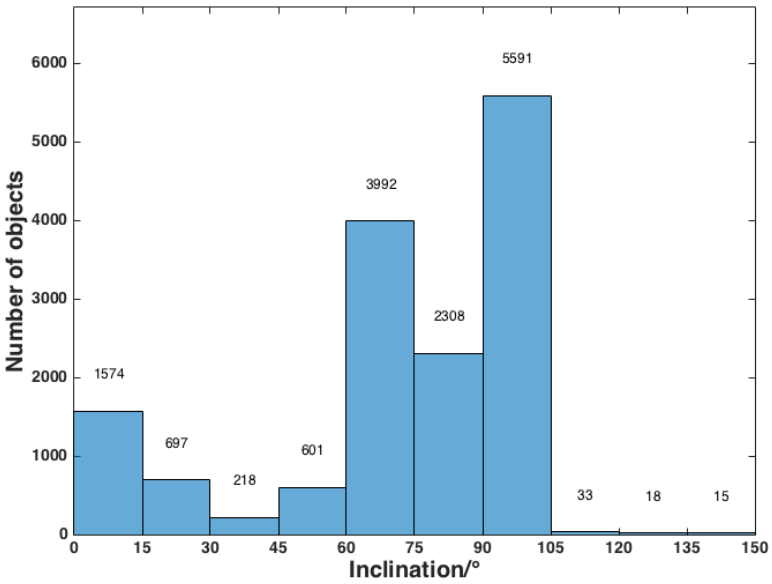

Figure 2.10: A histogram of the distribution of inclinations in the TLE database. The equatorial objects (i=0) are primarily those in the GEO ring. The majority of objects here have an inclination i=60-105°

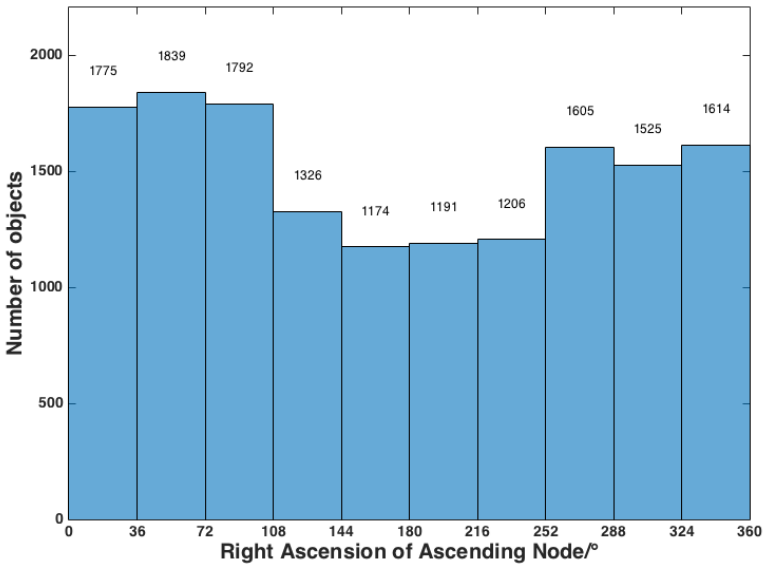

Figure 2.11: A histogram of the distibution of the RAAN in the TLE database. There is a fairly uniform distribution of RAAN values.

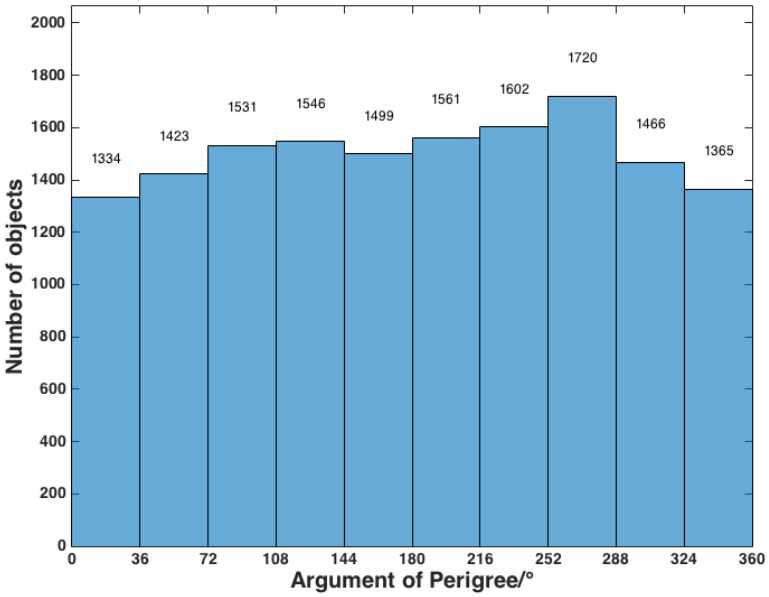

Figure 2.12: A histogram of the distribution of the Argument of Perigee in the TLE database. The distribution is fairly uniform.

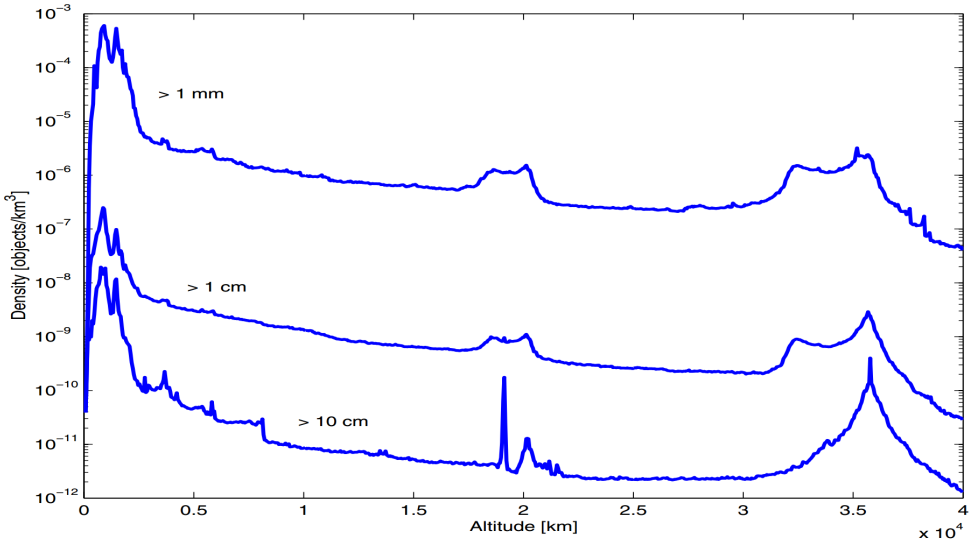

Figure 2.13: The volume density of debris against altitude, courtesy [3], showing similar results to those obtained in this analysis of TLEs

2.5 Orbit and attitude evolution

2.5.1 The orbit prediction problem

To predict the future orbit of an object, the main techniques are analytic, semi-analytical and numerical. The analytic method uses a single step to calculate the position and velocity of a satellite based on the initial conditions. The advantage here is the low computational complexity, but the disadvantage is the lack of accuracy even over the short-term. Predictions diverge from observations even over a few hours.

This is because only the most simple physics are captured with this method. The use of analytic propagation is limited to coarse, long-term simulations and the computational simplicity enables simulation of large numbers of objects simultaneously. Numerical methods use physics-based equations with many steps for numerical integration, with the advantage of high accuracy depending on the complexity of the physics and computational processes implemented, albeit at the cost of computational power - it is very time-consuming and computationally intensive to run such simulations. Semi-analytical methods sit between analytical and numerical methods in that the analytical method is extended to include a low-order numerical integrator for other forces and can therefore model some of the secular and long-term periodic effects.

In this work, numerical methods are used to capture the nuances of the physics driving attitude motion, in order to analyse the effect of attitude change on the overall orbital motion.

2.5.2 Force and orbit modeling

Force modelling is the method of calculating the effect of physical influences on the future position of an object. Using models of known forces and Newtonian mechanics, we can predict the future position. In the space industry, force modelling is used in satellite design and operation and influences the physical design of satellites.

The forces and torques acting on an SRO are shown in Figure 2.14 and in 2.15.

The former is a depiction of the influences of the natural space environment, and the latter shows which are included in the model.

- Atmospheric drag, to model interactions with sparse molecules of air and plasma around the Earth
- The J2 gravity term to account for the oblate spheroid shape of the Earth and higher order terms for other departures from a point mass model
- Third-body gravity terms for the Sun, Moon, and some other planets
- Radiation pressure, from the Sun and from the Earth, whereby the reflection or absorption of photons yields a net momentum transfer
- Electromagnetic interactions - forces on charged objects moving within magnetic field of the Earth

The following figures were generated using the models that were developed in this method. They show the forces (Figure 2.16) against altitude. The justification for the forces and torques which are included in the model is based on these graphs.

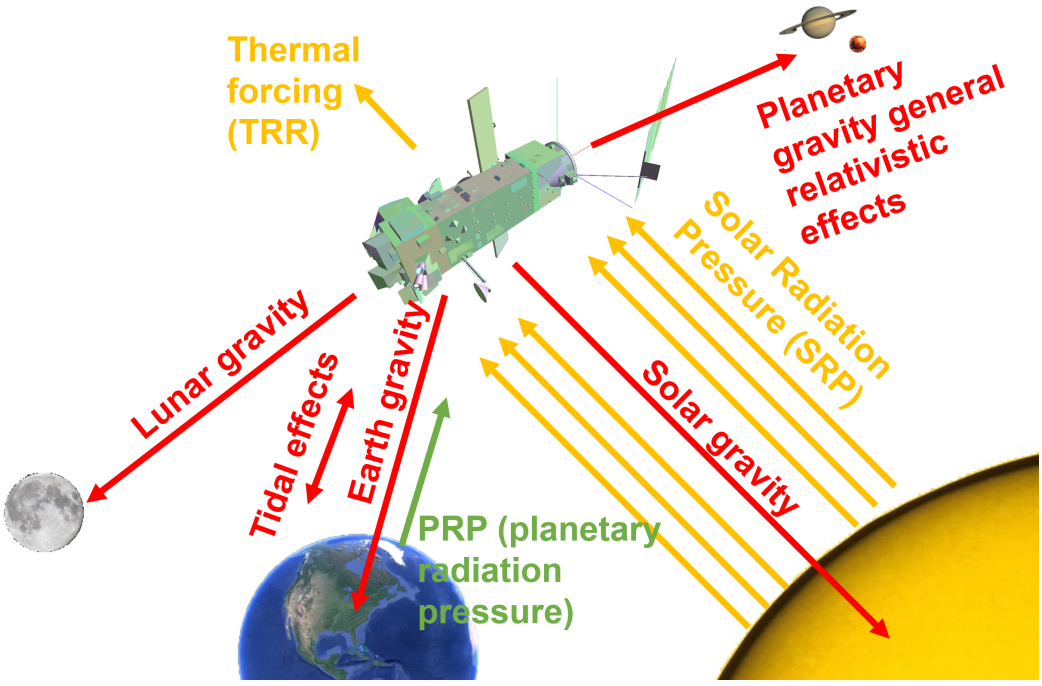

Figure 2.14: A diagram of the forces and torques acting on Envisat as an example of an SRO

Current force modelling techniques are generally optimised for operational satellites, including the UCL codebase.

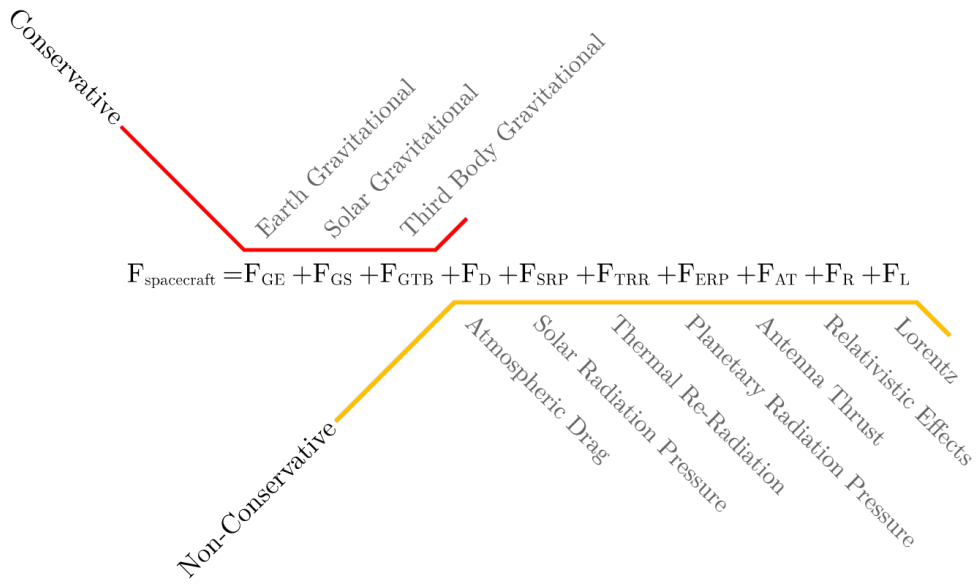

Figure 2.15: The physical forces which act on a spacecraft

This project applies such techniques to space debris orbit prediction, and this change of intended use requires a few notable changes. Most spacecraft have both orbit and attitude control mechanisms which compensate for periodic, sporadic and unmodelled forces to keep a satellite in its desired orbit, and pointing in a particular direction. Periodic, sporadic and unmodelled forces might include the solar wind, Lorentz force and radiation pressure. Control systems do not exist for space debris which are by definition passive, and so a more in-depth analysis of the forces and torques on such objects is required to predict their future motion.

Force models previously applied to the problem of space debris include the following [50]:

- Geopotential modelling with degree and order of 30 or more
- SRP modelling, with a box-and-wing or pizza-box approach rather than high-fidelity
- Atmospheric drag modelling
- Third body gravity

These are less sophisticated than the models used at UCL, particularly for SRP. The models are generally applied to long-term simulations for the purpose of coarse conjunction analysis of the whole debris constellation rather than for precise

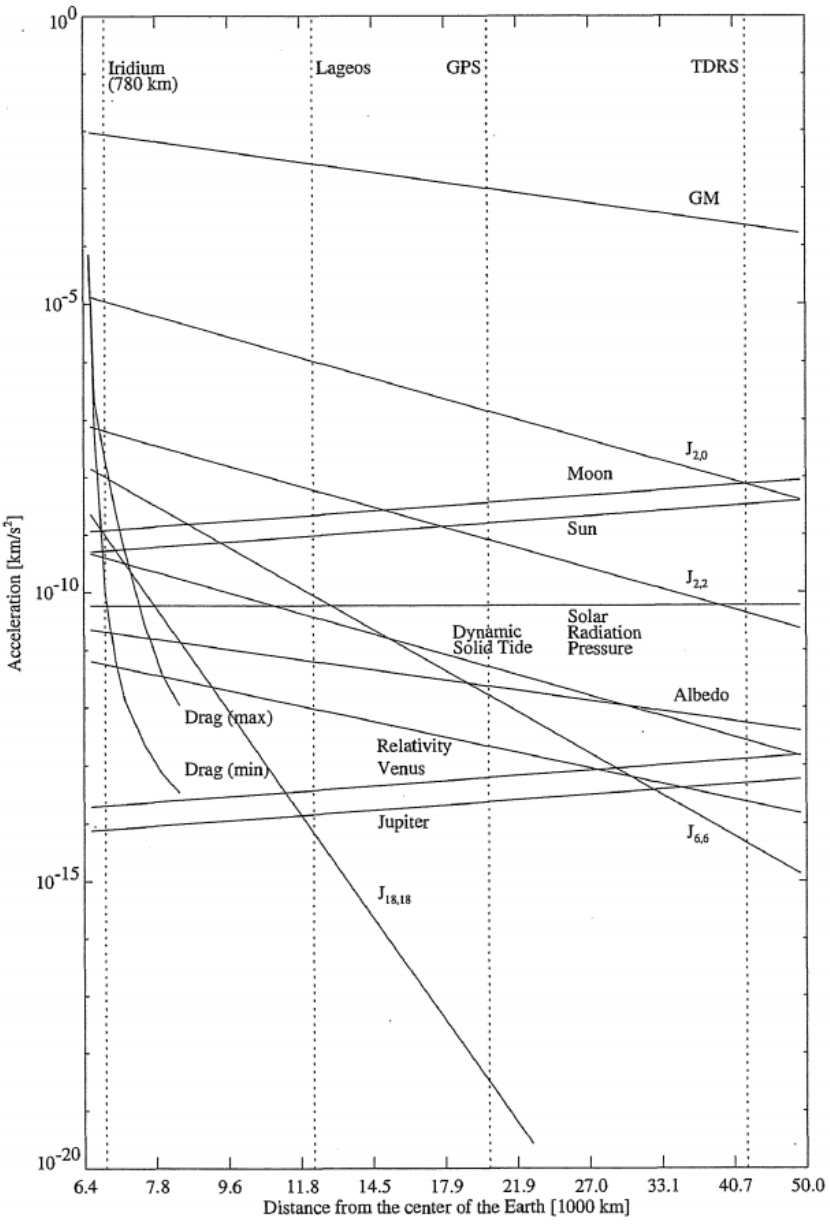

Figure 2.16: A graph of forces acting on a satellite against its altitude, courtesy Montenbruck and Gill [4]

single-object orbit prediction. The former is the focus of other research groups, whereas the latter is the primary focus of this project.

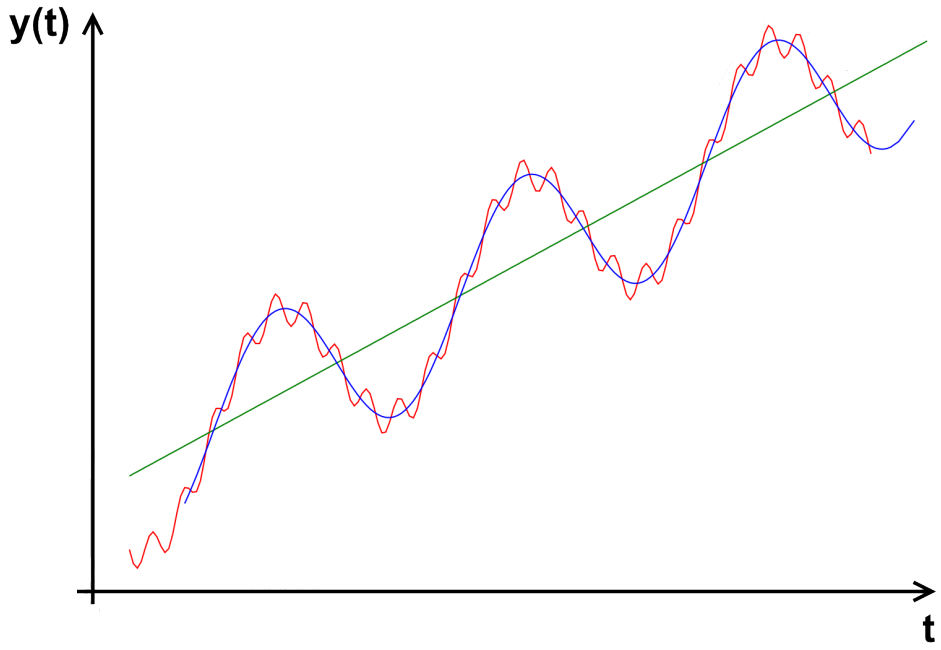

Figure 2.17: A comparison of secular, short and long periodic effects. The green line shows secular effects that give a net change over time. The blue line shows the combination of secular and long-term periodic effects, and the red line shows the additional effect of short-term periodic effects

There are three main variations to be modelled; secular, short-term periodic and long-term periodic. These are shown in Figure 2.17. The secular variations are ones which can shift SROs into different orbits, and are of the largest concern for space debris. The periodic variations are split into long- and short-term and their relative amplitudes are important, but the main difference is that periodic effects cause variations which can be averaged out, in comparison to secular effects which can change the orbital regime and cause objects to drift into other orbits.

The forces and torques exerted by radiation are complex to model. The direction of these is dependent on the radiation source - the Earth reflects Solar radiation and so the orbit geometry can have a significant impact on how the two radiation sources (Earth and Sun) interact wth the orbiting body. The effects of shadowing and of umbra/penumbra/full-phase transitions are also complex.

A good example of periodic radiation forces is in the Hubble Space Telescope

(HST), which required replacement parts on a 1993 service mission. This was due to vibrations caused by the transition from shadow into the full phase region, which led to vibrations of the satellite solar panels being transmitted to the spacecraft body and resulting in blurry images. The service mission replaced solar panel support poles, which were expanding and contracting resulting in the vibrations. Additional sleeves were added, and the problem of blurry images was fixed.

When radiation intersects a physical body, there is a net momentum transfer associated with the energy of absorption or reflection. This momentum transfer, acting on an orbiting body, perturbs the orbit. There are many sources of radiation which impact an SRO: solar radiation (SRP), Earth radiation (ERP - both thermal and reflected solar radiation), and the thermal emission of the object itself.

The Space Geodesy and Navigation Laboratory (SGNL) research group have a prestigious heritage in radiation pressure modelling [41], specifically in modelling non-conservative forces on spacecraft. These models utilise high-fidelity models of satellites with more realistic representations of satellite geometry. This will be extended to calculate both the force and the torque due to radiation pressure. The torques are potentially important because they influence the spin evolution of SROs. Consequently, a better understanding of the time variation of SRO spin is important in both the detection and identification of SROs by ground-based tracking technology.

There are also unmodelled forces which are generally ignored or which have been considered to be negligible. An example of this is the Lorentz force. Previous work on modelling the Lorentz force is limited to solar sails and artificially charged satellites, with a surface charge that is assumed to be constant[51]. For space debris, previous analysis of magnetic interactions is limited to the spin damping effect of spent rocket stages through Eddy currents [52]. The current generated in the large metal rocket body, by the magnetosphere, acts to oppose its rotation. This contrasts with the direct Lorentz force on a charged object leading to perturbations in the orbit. The Lorentz force has not previously been considered as a significant perturbation for general SRO orbits, but initial studies were presented at an astrodynamics conference.

2.5.3 Gravitational forces and torques

The most simplistic model of the Earth's gravity field is a point mass (monopole), as described in equation 2.2. In reality, the complex gravitational field of the Earth varies with both latitude and longitude. The monopole model can be extended to an oblate spheroid using the J2 term, which captures the dominant effect of the latitudinal variation in gravity, through spherical harmonics.

The gravity model that was previously described assumes a point mass. In reality, the mass of the Earth is not uniform and this assumption is therefore inaccurate. To provide a reference surface describing the Earth, we assume that shape of the Earth is an oblate spheroid where the radius at the poles is less than that at the equator. In order to model the physical mass distribution of the Earth more accurately, we use a spherical harmonic expansion of the Earth's geopotential energy. The coefficients for such a model are given in Table 2.5. After the monopole term, the oblateness coefficient J2 (2,0) is 10^{-3} times smaller, and the other coefficients are 10^{-4} times smaller than J2. In this study, a J2 model is used due to the relative sizes of the contributions given in Table 2.5.

From the gradient of this model with respect to space we can estimate gravitational accelerations. Considerable research and measurement technology has gone into improving such models over the last twenty years and for much of the analysis required for space debris, the gravity field model is effectively a solved problem. The recent Earth Gravitational Model 2008 (EGM2008) [53] is complete to degree and order 2159.

For satellites, the gravitational attraction of planets other than the Earth is simple to calculate, although we move away from the two-body problem into a problem with many bodies. The third-body gravitational forces can be calculated computationally, as long as the ephemerides are available. The JPL (Jet Propulsion Laboratory) DE405 (Developmental Ephemerides) will be used [54].

The most significant third-body forces are those of the Sun and Moon [55]. Once a given third-body force is included in the model, additional third body forces are relatively simple to include. Thus the balance between speed of computation and

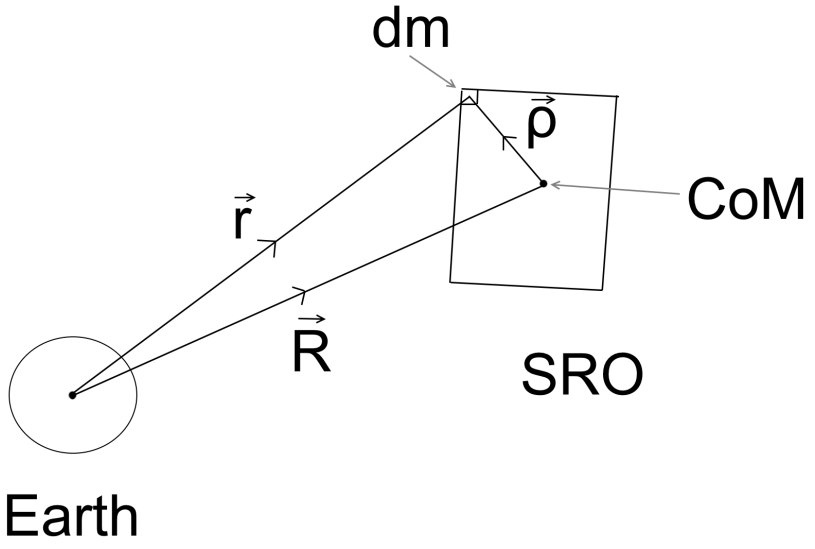

Figure 2.18: A diagram of the torque exerted on an SRO due to gravity gradients

the number of additional gravitational terms can be decided once the code is in place.

degree,order	$\frac{dU}{dX}$	$\frac{dU}{dY}$	$\frac{dU}{dZ}$	$\lvert\frac{dU}{dR}\rvert$
1,0	1.18E-01	2.50E-01	-5.48E-01	6.14E-01
2,0	-3.58E-05	-7.58E-05	5.50E-05	1.00E-04
2,1	-1.35E-10	6.31E-11	8.93E-11	1.74E-10
2,2	-1.69E-07	8.17E-08	3.16E-09	1.88E-07
3,0	2.69E-08	5.71E-08	-1.63E-08	6.52E-08
3,1	1.39E-08	-5.97E-08	1.51E-07	1.63E-07
3,2	-3.85E-08	1.95E-08	4.78E-09	4.34E-08
3,3	1.22E-08	4.14E-09	1.59E-08	2.05E-08
4,0	4.48E-09	9.48E-09	1.63E-09	1.06E-08

Table 2.5: A comparison of the relative strengths of gravity models for increasing degree and order spherical harmonic coefficients. Adapted from Ziebart [13]. Here, the $|dU/dR|$ column was calculated in order to give an indication of the relative magnitude of the radial component for each spherical harmonic acceleration coefficient.

As a brief introduction to the gravity gradient torque, take a satellite of mass m with its centre of mass at distance $\vec{R}$ from the centre of the Earth. This satellite can be split into mass elements, each a distance $\vec{\rho}$ from the CoM. This is shown in Figure 2.18. Note that $\vec{r} = \vec{R} + \vec{\rho}$. The force on each mass element can be written:

$$d\vec{F} = -GM\frac{dm}{r^3}\vec{r} \tag{11}$$

The torque about the CoM due to this mass element is:

$$d\vec{L_g} = -\vec{\rho} \times GM\frac{dm}{r^3}\vec{r} = -\vec{\rho} \times GM\frac{dm}{r^3}(\vec{R} + \vec{\rho}) \tag{12}$$

$$= -GM\frac{dm}{r^3}\vec{\rho} \times \vec{R}$$

$$r^2 = (\vec{R} + \vec{\rho})(\vec{R} + \vec{\rho}) = R^2\left[1 + \left(\frac{\rho}{R}\right)^2 + 2\frac{\vec{R}.\vec{\rho}}{R^2}\right] \tag{13}$$

where $|\vec{R}| = R$. Under the assumption that $|\vec{\rho}| << |\vec{R}|$, we can use the Taylor expansion to simplify

$$r^{-3} = \frac{1}{|\vec{R}|^3}\left[1 + \left(\frac{\rho}{R}\right)^2 + 2\frac{\vec{R}.\vec{\rho}}{R^2}\right]^{-3/2} \approx \frac{1}{|\vec{R}|^3}\left[1 - 3\frac{\vec{R}.\vec{\rho}}{R^2}\right] \tag{14}$$

Thus,

$$\vec{L_g} = -\int GM\frac{1}{r^3}\vec{\rho} \times \vec{R}dm = -\int \frac{GM}{R^3}\left[1 - 3\frac{\vec{R} \cdot \vec{\rho}}{R^2}\right](\vec{\rho} \times \vec{R})dm \tag{15}$$

This can be integrated (see [56]) to give:

$$\vec{L_g} = \begin{cases} \frac{3GM}{2R^3}(I_z - I_y)sin(2\phi)cos^2(\theta) & \text{about } x \\ \frac{3GM}{2R^3}(I_z - I_x)sin(2\theta)cos(\phi) & \text{about } y \\ \frac{3GM}{2R^3}(I_x - I_y)sin(2\theta)sin(\phi) & \text{about } z \end{cases} \tag{16}$$

2.5.4 Rotating frames

It is important to consider the wide variety of reference frames needed in the modelling of a rotating object in orbit. The four frames useful for this research are Earth-Centered/Earth-Fixed (ECEF), Earth-Centered Inertial (ECI), Orbit-Fixed (OF) and Body-Fixed (BF).

Reference frames and orbital elements are chosen to most conveniently reflect a given scenario and bring out the desired dynamics in their simplest form. There are two main subsets of reference frame - Earth-centered and object-centered. Earth-centered frames fall into two categories: inertial (non-rotating) and rotating frames. The reference frame which gives us the least complex motion for an object in orbit is the Earth Centered Inertial (ECI) frame. This is a cartesian xyz frame, in

which the xy-plane is chosen as the equatorial plane. Orbits are most conveniently expressed in Keplerian elements. Under a monopole gravitational model, the Keplerian elements do not change with the exception of ν which describes the position of an SRO within the ellipse. The orbit of an SRO is calculated in the ECI frame as this is where Newtonian laws are valid. The rotating frame is required in order to implement J2 and higher order gravity models. The force models include both the J2 Earth oblateness term and the forces from other celestial objects (Moon, Sun, other planets). J2 is calculated in the ECEF frame, whereas the positions of celestial objects are defined in the ECI frame. Transformations are required between all of these frames and representations of state. The necessary transformations are described in [57].

Of the object-centered frames, the two main ones are orbit-fixed (OF) and body-fixed (BF). The OF x-axis is approximated by the velocity vector; the out-of-plane vector is the y-axis and the nadir vector pointing towards the Earth centre is the z-axis.

$$\vec{O_z} = \vec{r} \tag{17}$$

$$\vec{O_y} = \vec{r} \times \vec{v} \tag{18}$$

$$\vec{O_z} = \vec{O_y} \times \vec{O_z} \tag{19}$$

This frame moves with the SRO centre of mass and is independent of the object attitude - it does not model tumbling. The BF is fixed to the SRO - for example, the z-axis is fixed with an antenna which is intended to be pointing in the nadir direction. As the SRO tumbles and its attitude changes from the "ideal" or intended scenario, the BF deviates from the OF. These transformations are described in [58].

The convention which is used in this method, is to model the Euler angles from the ECI frame to the BF. That is, the BF is translated onto the Earth centre, and the resulting angles between the BF and ECI frame are computed and logged as the simulation progresses.

2.5.5 Torque and attitude modeling

The influence of the natural space environment on uncontrolled objects in orbit cause torques that lead to their tumbling. Whereas active satellites have control mechanisms to periodically adjust their orbit and attitude, debris are by definition passive. The forces and torques exerted by the natural space environment therefore have a more direct and irreversible effect on the orbit and attitude of debris. The varying attitude of debris modifies the way in which non-conservative forces apply to such objects. These are particularly important for HAMR objects such as space debris. Changes in attitude lead to changes in surface force, such as SRP, which result in perturbations that change with attitude. Further analysis in this area could lead to improved models of the spatial distribution of space debris, enhancing SSA. It could also lead to innovative methods for influencing future debris with a view to safe and timely de-orbiting. Furthermore, the attitude of an object determines its visibility to ground-based tracking methods and so it is important to integrate such models with observation systems to enable optimal acquisition. The focus of this work is primarily a study of the influence of SRP torques on the attitude and orbit of HAMR debris.

For actively controlled satellites, the problems of orbital motion and known attitude motion are treated as separable. This is a reasonable simplification, as the active systems which control a satellite orbit and attitude are often separate. For passive debris, this is not a suitable simplification. The orbit and attitude are interdependent through the mechanism of non-conservative torques, which act to modify the attitude, and are also linked to the non-conservative forces which are attitude-dependent.

In this study, rigid body dynamics are assumed. Rigid-body dynamics are a precise application of Newton's Second Law of Motion, but at the same time, they ignore the Second Law of Thermodynamics. The lesson from Explorer 1 was that rigid-body dynamics are not always a good assumption [56]. Explorer 1 started off tumbling about its axis of minimum moment of inertia, but this soon changed to tumbling about the maximal moment of inertia axis. This was because the

antennae were "whipping" and dissipating angular momentum but total angular momentum is conserved, and so it was dissipated into tumbling about the other axes.

A torque is found by summing the moment of each contributing force about the center of mass of an object:

$$\vec{\tau} = \sum_i \vec{r_i} \times \vec{F_i} \tag{20}$$

This torque vector has three elements, which are the torques about the x-, y- and z-axes respectively. An example of the cross product torque calculation is given in Figure 2.19. In this figure, the red arrow represents a force on the satellite. This force is applied about the centre of mass on a moment arm (green arrow), and results in a torque that causes the object to rotate (blue arrow). The blue arrow is represented by an out-of-plane vector.

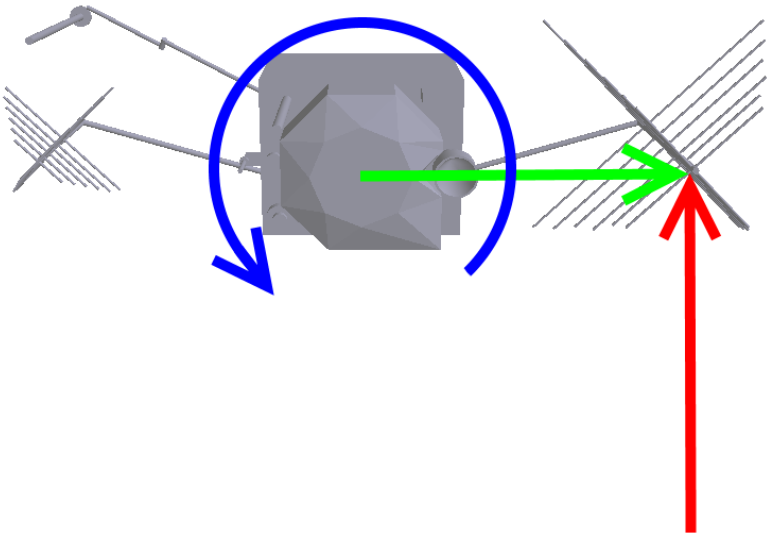

Figure 2.19: The torque cross product; the blue arrow represents a vector coming out of the page

A right-handed convention is used, so a positive torque induces a clockwise rotation when looking along a given axis Figure 2.20.

In rotational mechanics, the equation of motion for rotation about the centre

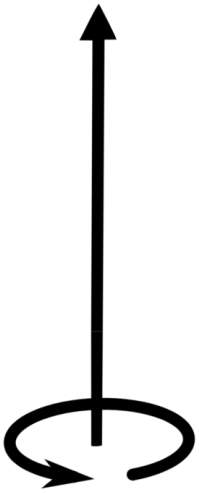

Figure 2.20: The right-handed convention for torques

of mass is given by Euler's dynamical equation; see equation 21; there are parallels between force and torque equations of motion

$$\vec{\tau} = I\vec{\omega} = I\ddot{\vec{\theta}} \tag{21}$$

$$\vec{\omega} = \dot{\vec{\theta}} \tag{22}$$

where:

$\hat{\tau}$ represents the torque exerted on an object about a given Cartesian axis

I is the moment of inertia

$\vec{\omega}$ is the angular acceleration vector

$\dot{\vec{\theta}}$ is the angular displacement vector

This is analogous to Newton's second law in classical (translational) mechanics:

$$\vec{F} = m\ddot{\vec{x}} \tag{23}$$

Numeric integration is the technique used to computationally solve the second-order ordinary differential equations which predict orbit and attitude motion. The technique is used to propagate this attitude and predict its future value, giving the evolution of the angular displacement from the initial attitude.

The centre of mass $\vec{R}$ and moment of inertia about axes I can be calculated from the geometry and physical properties of the object:

$$I_x = \sum_i m_i(y_i^2 + z_i^2) \tag{24}$$

$$I_y = \sum_i m_i(x_i^2 + z_i^2) \tag{25}$$

$$I_z = \sum_i m_i(x_i^2 + y_i^2) \tag{26}$$

The center of mass of complete satellites is variable, due to fuel tanks emptying over the course of their operation and due to the sloshing of fuel. Manned missions also have the factor of crew movements which can impact the attitude motion. Some satellites also have spinning momentum wheels which contribute to the gyroscopic stabilization of attitude. For the purposes of this work, these effects are ignored, as the models are intended for application to HAMR debris rather than active satellites.

The physical characteristics (mass, area, center of mass, moment of inertia) are difficult to obtain for debris in orbit. Some characteristics may be obtained through fragmentation experiments, or derived from observation. The MSG2 cooler cover and Envisat were chosen as test object as they are known to be tumbling, and because we have a good knowledge of their physical characteristics as they are intact as far as is known. Torques on SROs are caused by asymmetries in physical geometry and asymmetric forces - the key factor being a physical imbalance. Uniform moments on an object tend to cancel. Torques are also induced on objects which have a centre of mass that is not at the geometric centre of the object. Space operators usually seek to minimise the torque in the design phase.

The effect of gravitational torques are normally the largest and, broadly speaking, act to align the SRO axis of minimum moment of inertia with the zenith vector (i.e. the local vertical) [56]. The axis of maximum moment of inertia is aligned normal to the orbital plane through combined gravity gradient and centrifugal effects, and the intermediate moment axis is then in the direction of the velocity vector. Gravity gradient stabilisation makes use of this phenomenon to constrain

the attitude of an SRO to a low precision and has been utilised since some of the earliest manmade satellites [58]. The torque exerted by gravity is perturbed by the momentum exchange of incident photons, including both SRP and ERP. The SRP is directed from the Sun onto the object, and the ERP is in the zenith direction (to first order). The forces and torques exerted by these depend on the satellite shape and geometry; the orbit of a HAMR SRO has a greater perturbation, and a highly asymmetric SRO experiences a greater torque. This effect can be exaggerated briefly in the penumbral transition, due to the non-uniform solar photon flux. The drag force arises in the interaction of the sparse atmosphere at orbital altitudes with the satellite surface. It perturbs the satellite attitude to minimise drag; that is, the satellite experiences a drag torque unless it is in an aerodynamically favourable attitude. A restorative torque is exerted when the SRO is in an energetically unfavourable attitude. There are additional torques which need to be considered in a complete model of attitude evolution, such as the Lorentz torque. A force is exerted by the electromagnetic interactions of SRO surface charge and residual magnetic dipoles with the geomagnetic field [59]. This is known as the Lorentz force. The charge distribution is non-uniform, and this combines with the different surface material properties (such as capacitance and conductivity) to exert a torque.

These torques combine to give complex influences on the attitude of SROs. For active satellites, there are stabilization mechanisms which counteract external influences and allow a desired satellite orientation. For passive SROs, the torques lead to tumbling which perturbs the orbit and which also influences their observation. For application to HAMR debris at altitudes above 1000km, the gravitational and drag torque are small in comparison to radiation torques. The gravitational torque is small due to the small size and low moment of inertia of HAMR debris, and the drag torque is small because the atmosphere is so sparse at higher altitudes. This study focuses on the radiation pressure torque caused by solar illumination of an HAMR SRO at a high altitude. An example of this is the MSG2 cooler cover, which is a flat plate near the geostationary ring.

Modelling the effect of these torques on an object is a difficult problem of itself.

Whereas the evolution of position is intuitive, the evolution of attitude is more counterintuitive and requires a more detailed mathematical framework. This is because successive changes in attitude are non-commutative - the order of rotations is important, whereas for position the order does not matter. This leads to Euler parameters and quaternions to describe consecutive changes in attitude. If the changes in attitude are infinitesimal, then consecutive rotations do commute.

The equations of motion for torque modelling are similar to those for force modelling. In torque modelling, the differential equation of motion is given by Euler's dynamical equation (Equation 21). The torque is found by summing the moment of each force about the centre of mass, just as linear forces are summed to find an acceleration. There are three main torques on SROs in the literature: gravitational, aerodynamic drag and radiation [56]. An additional force which could be analysed is the torque due to differential surface charging and the Lorentz force:

$$\vec{\tau} = \vec{\tau}_{grav} + \vec{\tau}_{drag} + \vec{\tau}_{rad} + \vec{\tau}_{Lorentz} \tag{27}$$

The force due to radiation pressure, in the case of total absorption, is:

$$\vec{F} = pA_p\hat{S} \tag{28}$$

where p is the photon flux radiation pressure, A_p is the area presented to the photon flux and $\hat{S}$ is the normalised Poynting energy flux vector. HAMR objects have an increased influence from radiation pressure due to their greater area to mass ratio in comparison to smaller and denser SROs. The torque is calculated using the difference between the centre of pressure (CoP) and the centre of mass (CoM) [58]. The centre of mass is determined by solving

$$\frac{1}{M}\int_V \rho(\vec{r})\left(\vec{r} - \vec{R_{CM}}\right)dV = 0 \tag{29}$$

where $\vec{R_{CM}}$ is the centre of mass, M is the total mass, V is the volume of the object and $\rho(\vec{r})$ is the density. Analogously the centre of pressure is determined by

the integral of the force per unit area exerted by each ray

$$\frac{1}{A}\int_{A}\left[\left(\vec{r}-\vec{R_{CP}}\right)\times\hat{F}\right]dA=0 \tag{30}$$

The vector from the CoM to the CoP is $\vec{r}_{mp}$ and the torque is then

$$\vec{\tau}_{rad}=\vec{r}_{mp}\times\vec{F}=pA_p\left(\vec{r}_{mp}\times\hat{S}\right) \tag{31}$$

These equations are the basis for computational analysis of torque and attitude modelling.

Two objects were chosen to demonstrate the codebase. These are Envisat, a large but now defunct satellite in low-Earth orbit, and the MSG2 cooler cover which was ejected when an Earth observation satellite was deployed. Envisat was chosen as an example of a very low area-to-mass ratio object and for low-Earth, and the MSG2 cover as a HAMR object near GEO; see Table 2.6.

Object	Semi-Major Axis (km)	Eccentricity	Inclination (°)
Envisat	7134	0.00011	98.4
MSG2 Cooler Cover	41,917.2	0.00023	2.5

Table 2.6: Orbital parameters for the objects chosen to demonstrate the debris toolset

Chapter Summary

This chapter presented the theoretical background in order to ensure consistency in terminology and to provide some detail on the science behind this analysis into the problem of space debris.

3 Review and Data Sources

Chapter Outline

In previous chapters, the importance of the space debris problem have been highlighted, along with a brief theoretical introduction to SRO force and torque modelling. In this chapter, prior studies around space debris observation, orbital modelling and the current models for force and torque modelling are given based on published literature. This serves two primary purposes: to set the scene of work that has already been done, and to highlight the gaps which are to be addressed in the method. This is followed by a description of the data sources available for use in the study.

> Houston, we have a trash problem!
>
> -**Sean Cooper**, *Wired Magazine*, 2007

3.1 Review

3.1.1 Space debris observation

Any modelling of the near-Earth space environment should be combined with observations in order to do meaningful analysis and to draw useful conclusions. In this section, observational studies of debris are described. Firstly, observational methods are compared. This is followed by specific studies that have identified debris characteristics which are useful for this thesis. Finally, observations of debris tumbling and the evolution of their tumbling are compared.

Space debris is typically observed optically using astronomical telescopes or via radar, usually with research or defense systems. Optical measurements are mostly for debris in higher orbital regimes and for the analysis of individual objects, due to the high angular slewing required to observe Low-Earth Orbit (LEO) objects optically which most telescopes cannot achieve [60]. In contrast, radar is more useful in characterising the entire debris population but cannot be used for higher altitudes due to power limitations. Optically, the observations take the form of

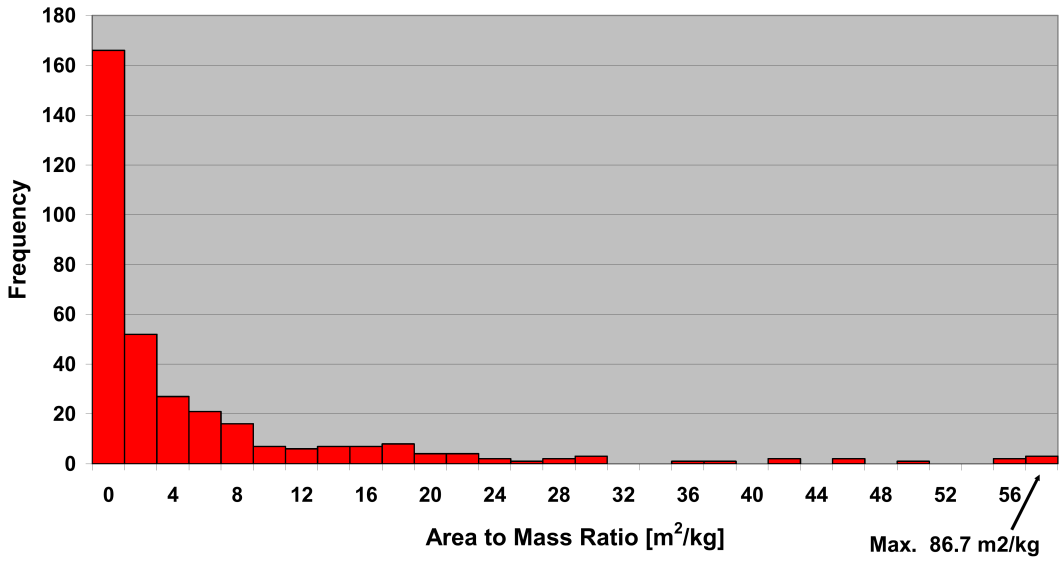

Figure 3.1: A histogram of the area-to-mass ratios of 345 observed debris, courtesy Schildknecht *et al.* [5]. Roughly half of all objects observed have AMR $> 2m^2/kg$ and are therefore classified as HAMRs

light curves. These give the apparent magnitude and its variation with time. Time-variation in apparent magnitude can be attributed to tumbling. Another use of optical observations is that they give information on the wavelength regime (colour of debris) and a better estimate of size than radar [25, 60].

Loftus and Potter [61] give a detailed chronology of events which generated space debris from 1961-1998. This is before some of the recent events such as the Iridium-Cosmos collision and the Fengyun-1C anti-satellite weapons test which both contributed significantly to the debris constellation in orbit today.

High Area-to-Mass Ratio (HAMR) debris were first observed by Schildknecht *et al.* in 2004 [44]. Their results were unexpected - these objects had not previously been observed, and objects with such high AMRs had not been seen before. The orbits of these objects are significantly perturbed by non-conservative forces such as radiation pressure, due to their HAMR properties [44]. Schildknecht *et al.* conclude that HAMR objects at high altitudes are strongly perturbed by solar radiation pressure, and that their observations suggest a strong attitude motion. This study shows that there are debris with HAMR properties, which are strongly perturbed by radiation pressure forces, and which are tumbling. A later conference paper presented a histogram of estimated area-to-mass ratio (AMR) values, which

is given in Figure 3.1 [5]. This figure shows that the AMR values for debris in the GEO region are mostly high ($> 1m^2/kg$), with some extremely high values ($> 10m^2/kg$). The AMR of specific debris are compared later in this chapter.

The origin and nature of the HAMR objects around GEO is not well known [62], and the mechanisms of their production are also unknown [5]. This leads to a difficulty in modelling due to uncertainty in the physical characteristics of such objects, and so the selection of appropriate objects to study is important.

Jehn *et al.* found 2790 uncorrelated objects in the GEO ring over 1000 hours of optical observations from 2001-2004 [63]. Based on these observations, they conclude that there were 450-540 uncatalogued debris with a brightness above magnitude 18.5 (corresponding to 25cm and larger) in the GEO ring.

Schildknecht and Fruh [64] use the CelMech orbit estimation tool [65] to determine the orbits of objects with a variety of AMRs based on their observations. They take sample objects from the debris catalogue and calculate the perturbations of orbits when radiation pressure modelling is considered using simple spherical calculations. These predictions are compared to observations. The authors conclude that the order of magnitude variation in the AMR value does not correlate to the order of magnitude variation in its error, and hence that the objects have a higher AMR than previously observed objects. This is an example of new debris characteristics being detected via ground-based observation, and a verification of the HAMR properties of a subset of the debris constellation.

Anz-Meador and Potter [66] focus on the area-to-mass ratios of orbital debris in two ways: firstly, fitting a distribution to data obtained by measurement of the orbital debris population, and secondly using results from laboratory experiments. An example given is that of Kosmos 1484, which was observed to have fragmented on 18 October 1993. The German TIRA / FGAN radar did not show any additional tracked objects in the vicinity, while other methods of analysis revealed approximately 79 new objects resulting from the sudden change in mean motion. This shows the uncertainty inherent in observation and the difficulties in accurate characterisation of the debris constellation, particularly after breakup events.

Skinner *et al.* [62] summarised the observations of HAMR objects around GEO,

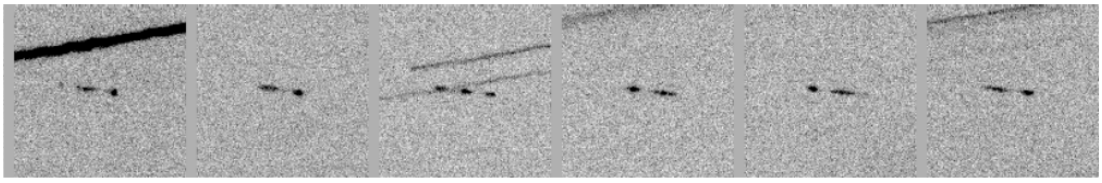

Figure 3.2: A series of optical tracks of an object near GEO, showing glints that indicate tumbling. Courtesy [6]

including the MSG2 cooler cover and MSG2 baffle cover .

Wirnsberger *et al.* [23] found an order-of-magnitude improvement in position determination accuracy through the use of bistatic satellite laser ranging (SLR), compared to regular SLR. This order-of-magnitude improvement in position determination also improved orbit prediction accuracy by an order of magnitude.

Tumbling of space debris has been observed, from LEO up to GEO. Seitzer *et al.* [6] have observed the tumbling of small objects near GEO. Previous optical GEO studies using 1m-scale telescopes run into problems due to the large apertures. The aim of Seitzer *et al.* was to observe the distribution fainter than magnitude R=20 (that is, debris under 10cm in diameter). The goal was to find the faintest magnitude observable from the ground. The 6.5m Magellan telescopes in Chile have observed 7cm diameter debris in GEO and characteristics of their tumbling through analysis of glints in the optical track.

An example of an optical track showing glints is given in Figure 3.2. Each portion of the image corresponds to an exposure of equal length - some have two "bright" peaks whereas the third image shows three peaks. 25% of observed GEO debris show glints in their optical tracks.

Objects of roughly 7cm in GEO can be observed assuming albedo 0.125. The authors [6] then looked for Titan debris 1968-081. These were found, clustered in RAAN-INC space, which means that they have a distinct pattern and link between their RAAN and inclination (showing that they are in broadly similar orbits). The tumbling of objects roughly 5 times per second (tumbling period 0.2s), gives "glints" or varying brightness in a given exposure. Objects visible in May 2012 include the MSG2 cooler cover. It is also noteworthy that the spectra for the test objects do not match any theoretical spectra - the authors suggested potential rea-

sons for this including rapid tumbling ($< 30s$ tumbling period), complex surfaces, shadowing, and errors in observation.

Optical surveys of GEO debris have been conducted by Seitzer *et al.* using the Michigan Orbital DEbris Survey Telescope (MODEST) 0.6m telescope [6]. The colours of debris were determined to be mainly red, presumably due to the material properties. Brightness variations were analyzed but the data is not of much use as the colour information was taken at different times. Later simultaneous observations of both colour and brightness [60] indicated that there is no correlation between the variation in magnitude and the variation in colour. The brightness of an object would relate to the observation geometry for HAMR objects, whereas the colour might indicate which facet of an object is being observed. Based on this, one might expect the magnitude and colour to be linked for a tumbling object - for example, a piece of MLI having different colours on different sides. However, Seitzer *et al.* found no correlation in their study.

Radiation pressure modelling and attitude propagation provide ways of simulating both magnitude and colour as viewed by an observer, which are important for improving understanding of HAMR debris, their tumbling and their orbits.

Boehnhardt *et al.* [67] analyse the change in rotation and tumbling period of the rocket body of Intercosmos 11, for the first two years after launch. The orbital and physical characteristics (Keplerian elements, dimensions, weight, etc.) of the rocket body are well defined, making this a good object to study.

A set of models were developed by Williams *et al.* [68], but due to the low area-to-mass ratio (LAMR) of the rocket body only basic force models were used, as the trajectory is near-ballistic. The optical observations agree with the model. It was found that the tumbling period initially accelerates from 5s to 1.2s due to outgassing of rocket propellant, over a period of 40 days. This is followed by a deceleration that appears to be linear, decreasing from 1.2s to a 20s period over 800 days. It also worth noting that they calculate the precession period of the orbital plane of an abandoned geostationary spacecraft to be 54 years.

Williams and Meadows [68] have shown that for orbital heights above 160 km this deceleration of the rotation is mainly induced by eddy current moments on the

conducting hollow cylinder due to the magnetic field of the Earth. Only below 160 km air drag moments on the satellite are comparable to the eddy current moments. Both of these effects become smaller with altitude and so will be ignored as other influences are more prominent.

Kirchner *et al.* [28] have performed experiments for bistatic SLR to debris, and multistatic SLR is being investigated for accurate 3d positioning of debris. The tumbling rate of debris can be derived from analysis of the specular or diffuse nature of the returned photons. Envisat, which died shortly before the observations were made, was found to be spinning along its orbit direction, at 0.0809 Hz or a 14.1s period.

Based on the changes in tumbling rate, we can conclude that the natural space environment exerts a torque on SROs. It is suggested that this torque is due to radiation pressure, but there has been little analysis of this theoretically. There is a need for modelling of attitude and tumbling, which may have a significant impact on the trajectory of debris. Once modelled, the improvement in prediction capability will give a better knowledge of how the constellation will evolve in the future. This can be validated against observations.

Finally, recent developments in observation technology are improving our knowledge on many characteristics. These include bistatic radar and bistatic SLR. In SLR, a pulsed laser beam of a particular frequency is bounced off of an SRO, and the returned photons are captured by an optical telescope [69]. The round-trip time between transmission and detection of the photons enables an accurate calculation of the distance of the SRO from the station.

Historic observations and modern developments in observation techniques must be combined with computational analysis in a validation step in order to give confidence that the computational approach is grounded in the physical reality of the system.

The papers described above show that observational data is available for the tumbling rates and the evolution of these, but there has been little analysis of this theoretically. This gap is the main focus of the research project. There is a need for modelling of attitude and tumbling, which may have a significant impact on

the trajectory of debris.

Previous studies on the effect of gravitational torques are limited to theoretical studies [70], and analytic studies of highly symmetric SROs [71]. These studies provide a good insight into the general physics of torques in the space environment, and the results are useful in characterising different modes of tumbling under gravitational torques alone. However, real SROs rarely possess such convenient symmetry, and they are also influenced by other torques. The extension of gravitational torque modelling into the computational realm enables study of specific SROs.

Tumbling of space debris has been observed [6, 14, 67, 68]. The focus in previous studies of space debris attitude and tumbling is predominantly on observation. Modelling is somewhat limited, and the studies that do exist have shortcomings which this thesis aims to address. One such study [72] uses an average over all attitudes in the non-conservative force modelling. This is inaccurate as a tumbling object should be modelled as such, and if drastic simplifications are needed, then the attitude should be averaged about its axis of rotation to retain some information on spin evolution dynamics.

A paper by Kelecy and Jah is one of the key papers in the attitude and tumbling of space debris [14]. This paper considers a statistical approach to modelling the evolution of spin states of SROs. The "normal" forces analysed on spacecraft (SRP, thermal emission, "potential electrostatic surface charging") perturb the orbits of SROs on the timescale over tens of days. This study considers these along with longer-term forces which act over weeks to years. The sample object for tracking is a spacecraft cover plate, from the MSG2 satellite, with well-defined physical parameters (mass, size and shape) and well-defined initial conditions (initial rotational state and initial orbital parameters) in order to validate and confirm the model. The cover was tracked in the first two months of 2012. The observed Keplerian elements are given in table 3.1.

The residual ratios match up exceptionally well between optical measurements and simulations. This is in part due to the statistical multi-hypothesis approach used in the analysis. The authors conclude by saying that analysis of the rotational

dynamics for HAMRs sampled over longer periods could lead to improvement in orbital determination and prediction accuracies. This is the basis of the method of this thesis. They also mention the NASA-AFRL General Mission Analysis Tool (GMAT), and that it could lead to a more rigorous estimation of orbital parameters for debris.

3.1.2 Modelling of space debris

Element	Value
Semi-major axis	41,917.2 km
Eccentricity	0.00023
Inclination	2.5°
RAAN	96.3°
Argument of Perigee	103.2°

Table 3.1: Keplerian elements for the MSG2 cooler cover as observed in Jan-Feb 2012 [14].

There is a vast body of research on space debris, dating back to the pioneering work of Kessler in the 1960s [22]. The initial studies dealt with the concept of space debris, as a growing concern for the booming space industry during the cold war. Most of the studies of space debris dating from 2000 onwards focus on mitigation of future debris generation, conjunction analysis for active missions, analysis of the current constellation and prediction of its future evolution. This work falls within the latter two sections, and so to set the context of this work and how it fits in with the literature a brief review of each of these is useful.

Loftus *et al.* [73] discuss the design requirements of spacecraft for protecting against the increasing flux of meteoroids and space debris. Protection against debris leads to increased mission and operating costs [38, 74, 75].

Skinner *et al.* [62] used solar radiation pressure techniques to model debris orbits in the geostationary ring. Their model assumes a set of flat plate surfaces, with both reflective and absorptive coefficients, specular and diffuse reflection, and allows for the variation in solar flux based on distance from the Sun as well as Earth eclipse. The key with models such as these, with regards to space debris modelling, lies in the initial conditions. The AMR is estimated as a whole, assuming a fixed

mass and a "radiation pressure coefficient" (C_r) of 1. Thus, any error in AMR results in an incorrect estimation of mass, incorrect estimation of area, or in a change in calculated attitude which causes a different area to be presented to the various radiation fluxes. Two of the tracked objects were the well-known MSG2 cooler and baffle covers. The other tracked objects had no a priori information. An interesting outcome of the optical measurements is the large periodic variation in the brightness, over a short timescale. These are not apparent in the IR data due to the averaging, and might actually be on a shorter time scale than is available with the optical data due to the exposure and integration times. The optical light curves indicate that the rotation period of the objects is of the order of many seconds or faster.

Anselmo and Pardini analyse the orbital trajectories of HAMR debris in two separate papers. Firstly in MEO, around GPS orbits [76], then in HEO [77].

In [76], the authors conclude that HAMR debris with AMR $20 - 40m^2/kg$ can survive for lifetimes upto 100 years in MEO, although above $45m^2/kg$ the orbital lifetime decreases rapidly to just a few months. They also note the complex interplay between SRP, geopotential and luni-solar resonances but with caveats on initial conditions.

Two major space agencies working on orbital debris modelling are ESA and NASA. Each developed their own models of the constellation.

The ESA software toolkits are ESABASE [78, 79], MASTER (Meteoroid and Space Debris Terrestrial Environment Reference) and DRAMA (Debris Risk Assessment and Mitigation Analysis) [80, 81]. The ESABASE package is a set of tools involving spacecraft geometry, kinematics and orbit determination. The common framework allows a variety of simulations to be carried out, including simulation of debris and meteoroid analysis. The current version of MASTER was released in 2009 [82].

Another toolkit has been developed by the NASA Johnson Space Center. This software is known as ORbital Debris Engineering Model (ORDEM), and a new version (v3.0) was released in 2012 [83]. This model combines in-orbit observations with post-mission estimates of debris size. The post-mission estimates come from

two main sources. The first of these is the analysis of space shuttle windows and other bodies after re-entry for evidence of small debris, and the second is data from in-orbit experiments which exposed banks of soft material such as aerogel to the space environment. Both of these give data on small object size and velocity. This means that ORDEM is useful in spacecraft design from the perspective of shielding against debris of size $10\mu m$ - $1m$, but as the propagation techniques are analytic, the software is not suited to precise prediction of individual object position and velocity.

These toolkits aim to provide satellite designers and operators with estimates of the quantity of debris for a given orbit, from the perspective of analysing the requirements for spacecraft shielding.

The Aeronautics research group at the University of Southampton have developed the DAMAGE (Debris Analysis and Monitoring Architecture to the GEO Environment) software package [84]. This software is semi-analytic, and is intended for quick long-term simulation of the entire constellation, to gauge how the debris environment might evolve over the course of decades to hundreds of years. These predictions are useful from a policy and international guideline perspective, but they are not accurate enough to predict the specific locations or attitudes of individual objects for the purpose of ADR.

3.1.3 Tumbling of space debris

The approaches taken in the literature towards attitude modelling are somewhat limited, particularly for the purposes of SSA. Previous work is mainly restricted to satellite modelling, from a view of operational constraint. Satellites maintain attitude through systems such as thrusters, momentum wheels and gravity gradient booms, and thus the external influences on attitude are absorbed by such mechanisms. The application of attitude modelling to space debris is important as debris is uncontrolled and passive, and so any changes in attitude have ramifications for both the object trajectory and the non-conservative force modelling such as radiation pressure and drag modelling. An object that is tumbling about its orbital path has a spin-stabilised orbit, and its tumbling may have an effect on

the chances of survival during re-entry [85].

Much of the previous academic work on tumbling can be split into two categories:

- Analytic calculations of tumbling for generic, simple objects
- Torques on specific, attitude-controlled satellites due to natural influences

Neither of these methods are well-suited to the calculation of tumbling of uncontrolled objects - the first because the near-Earth space environment is not so simple as to give realistic results from a purely analytic study for real-world debris, and the second because the torque calculations for attitude-controlled objects is from a control system perspective rather than an attitude evolution perspective.

Lin and Zhao [86] analyse the drag and eddy current torques on rocket bodies, using finite element methods to find a numeric solution to the boundary problem of charge distribution. Their work shows that eddy current torques are bigger than drag torques for rocket bodies. Whilst this work is important because it shows that electromagnetic effects are more important than drag on LAMR objects, the methods used are analytic and the larger torques (gravitational and radiation) are ignored. The conclusion in this work was that eddy current torques seek to align the rotational axis of a rocket body with the axis of maximum moment of inertia.

Two satellites which have been observed tumbling are LAGEOS (Laser Geodynamics Satellite) [87]. These are extremely low area-to-mass ratio satellites. LAGEOS I and II are a dense metallic ball with retroreflectors which enable precise positioning due to the stability of its orbit. Rotation has been observed but the cause of this rotation is unknown [88].

The effect of gravity gradient torques on generic space objects has been analysed [89], including the effect of the oblateness of the Earth [90]. In their analysis of orbit and attitude effects of drag and radiation, Klinkrad and Fritsche [91] conclude that *"good models of non-gravitational perturbations are a pre-requisite in precise orbit determination applications, predominantly for navigation constellations... and satellite programs with geodetic mission objectives ... The dominant surface forces... are due to direct radiation, indirect radiation and spacecraft emitted thermal radiation"*. This highlights the importance of non-gravitational pertur-

bations and of radiation modelling. The limitation of that study is again the semi-analytic method. The ESA ANGARA software package enables non-gravitational force calculations but is limited in its treatment of both object geometry and of surface interactions of photons and molecules.

Highlighting the importance of studying the tumbling of debris, a very recent study has been funded by ESA in collaboration with AIUB and HTG GmbH. This study, dubbed ιOTA [92], is to characterise the tumbling of debris for the purposes of rendezvous and is part of the ESA CleanSpace initiative for ADR. The first preliminary results were presented in March 2016 at the Astrodynamics Symposium in Darmstadt [93]. The test objects include Envisat and rocket bodies. The software is currently under development, although the project proposition is ambitious in its aims; the software is a 6dof propagator including "all relevant forces and torques, including aerodynamic drag, solar radiation pressure, gravitational influences of the Earth, Sun and Moon, eddy current damping, impulse and momentum transfer from space debris or micro meteoroid impact, as well as the optional definition of spacecraft specific influences like tank sloshing, reaction wheel behaviour, magnetic torquer activity and thruster firing". Analysing, modelling, coding and verifying each of these is a significant task, and integrating them all into a modular software suite has not been done before. The project is likely to last many years but the results of this thesis are in agreement with initial results of ιOTA as described in Chapter 6.

3.2 Data Sources

In order to run simulations of space debris, initial conditions and object-specific data are required. The main source of initial conditions for SRO orbits are the TLEs, as described in the scientific background along with their limitations. For the object-specific data, there are four main data sources:

1. Design data. For Envisat, the original spacecraft design plans give detailed specifications on the dimensions, mass distribution and mass history over the course of the designed lifespan.
2. Observational data. Observations give initial conditions for simulations,

but there are errors associated with different forms of observation which must be taken into account.

3. Experimental data. There have been experiments which recreate high-velocity impacts as expected in the space environment. Through the analysis of fragments from these controlled collisions, there are useful conclusions that can be made on the broad spectrum of object properties but very little useful specific data.
4. Simulated data. Objects can be "designed" to maximise the effects of certain influences of the near-Earth space environment, such as radiation torques. This is covered in more detail in section 5 - the key idea is to show what the maximum effect of a particular physical influence might be on a tumbling object in orbit.

Of these four data sources, design data and observational data will be used as inputs.

3.2.1 TLE database

The current space debris catalogue, as tracked by NORAD (North American Aerospace Defense Command), is maintained in Two-Line Element (TLE) data sets through the SpaceTrack and CelesTrack databases. These give the Keplerian elements of some 14,500 orbital objects. This data gives a good indication of the course orbital regimes where debris poses a threat to operational space. These are analysed in Section 2.4.

3.2.2 Test objects

A selection of the objects in the TLE database is useful for further analysis, and as validation of models which are developed. Two have been chosen - the MSG2 cooler cover (NORAD object ID 29676) and the now-defunct Envisat satellite (NORAD object ID 27386).

3.2.3 MSG2 / Meteosat-9 cooler cover

The MSG2 mission is a geostationary Earth-observation satellite. As part of the deployment procedure for the mission, a cooler cover was ejected from the satellite prior to its entry to the geostationary ring. This was done through the use of explosive bolts. The cooler cover has since been observed to be tumbling.

3.2.4 Envisat

The European Space Agency Envisat satellite was an Earth observation mission launched on 1st March 2002. It had an expected mission lifetime of 5 years. The satellite is large and heavy, and when communication was lost with the satellite in April 2012, concerns were raised. Envisat became a large piece of space debris as it could no longer be controlled. Observations of the satellite from April 2012 into 2013, included radar imaging, in-orbit optical imaging, ground-based optical imaging and satellite laser ranging. From these observations, it was determined that the satellite had not been in a significant collision and that it was physically intact. Figures 3.3 and 3.4 show imaging via radar and from a high-resolution optical Earth observation satellite respectively. They also show the approximate panel orientation which will be used in simulations. It has been observed to be tumbling. The AOCS (Attitude and Orbit Control System) consisted of thrusters, reaction wheels and magnetorquers [94].

Based on [93], the drag torque for Envisat is in the range $10^{-4} - 10^{-6}$ Nm, whereas radiation torques are slightly larger at $10^{-3} - 10^{-5}$ Nm.

Chapter Summary

This chapter provided the key literature which the research builds upon. Previous observational studies have led to the conclusion that a subset of space debris have HAMR properties, and have been observed tumbling with a period of 0.2s-30s. However, the origin and nature of these objects is uncertain. Their spin behaviour affects their orbital motion strongly, due to non-conservative forces. Previous analysis of uncontrolled SROs is focused on force modelling, with a recent announcement of 6dof analysis from ESA. The gaps identified are therefore:

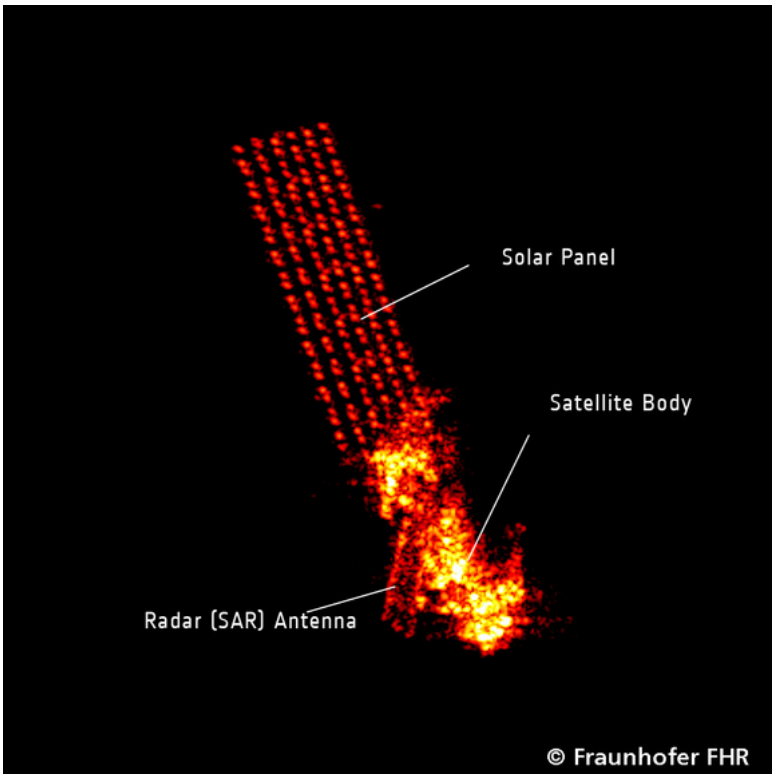

Figure 3.3: A radar image of Envisat taken by the FHR TIRA radar station in Germany, courtesy [7]

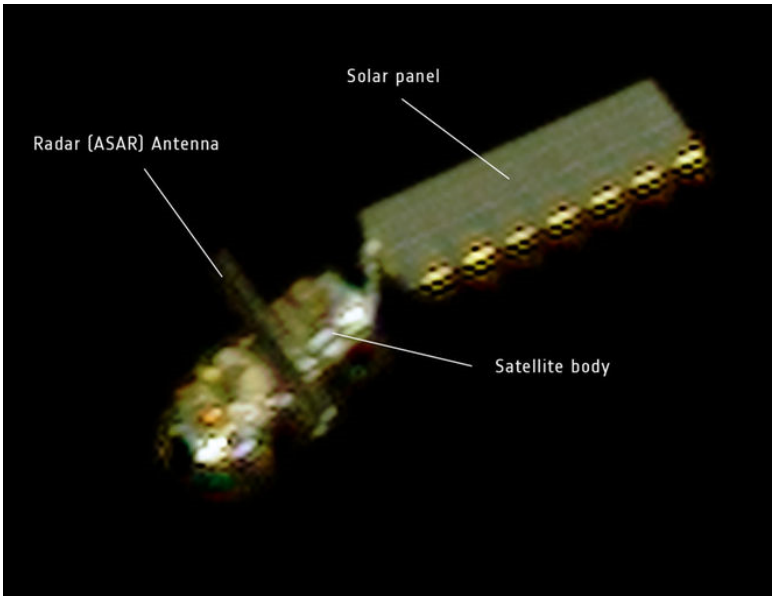

Figure 3.4: An optical image of Envisat taken by the Pleiades satellites, courtesy [8]

- High-fidelity modelling of radiation forces on HAMR objects,
- Torque and attitude modelling to explain the tumbling behaviour (and evolution thereof) for HAMR debris, and enable better application of non-conservative forces.

An analysis of the current debris catalogue has also yielded some useful conclusions regarding the distribution of debris. This analysis has influenced the choice of test objects for the main simulations.

4 Method

Chapter Outline

The previous chapters outlined the scientific theory and gaps in current research on orbit and attitude modelling of space debris. This chapter begins with a detailed problem statement, followed by a description of a method for calculating radiation torques using a pixel array method. The over-arching aim here is to develop the capability to model radiation torques on complex, realistic models of space vehicles and space debris. This is followed by an attitude model for computationally simulating objects tumbling in orbit, in order to meet the aims and objectives of the research. The methods were implemented in code (C++ and Matlab). New modules were written and added to the pre-existing radiation pressure modelling suite with appropriate interfacing between the two. While the specific code is not covered in detail, the algorithms and procedures used to simulate tumbling objects are given.

The two main aspects of this thesis are (a) modelling the torques due to radiation, and (b) investigating the effect of tumbling on orbital motion. The first half of this chapter describes how radiation torques are modelled using the pixel array method. The method used for investigating the effect of tumbling on orbital motion can be broadly split into the following (see also, Figure 4.7):

- Inputs and transformations
- Force and orbit modelling
- Torque and attitude modelling
- Propagation methods
- Visualisation

The second half of this chapter is structured around each of these. Verification, results and analysis of the implementation are covered in the following chapters.

4.1 Problem Statement

4.1.1 General aims

The broad aims of the research, based on the initial project proposal, are summarised below.

Aims

- Carry out a programme of basic research on the orbital behaviour of space debris, Technical Readiness Level (TRL) 1-3,
- Utilise non-conservative force and torque modelling techniques to predict the orbit and tumbling evolution of space debris with sufficient accuracy for the dual purposes of acquisition and tracking analysis, and for long-term orbital evolution analysis on the scale of decades,
- Carry out research that contributes to secured access to space over the next 50-100 years in the context of both the short-term and the long-term evolution of orbital debris, through computational simulation of their orbits.

These aims are explored computationally, with the starting point being previously available code; this includes an orbit propagation suite and the SGNL radiation force modelling software which implements the pixel array method.

4.1.2 Detailed objectives

These aims have been split into detailed objectives, and from these the specific research tasks can be defined (in approximate order of priority):

Objectives

- Build a software toolkit for orbit simulation, to include the following forces: Earth gravity, Lunar and Solar gravity, Solar radiation pressure (SRP), and the electromagnetic Lorentz interaction.
- Develop and test high-precision modelling techniques to calculate radiation pressure torques for space debris, ranging from simple fragments up to the scale and complexity of space vehicles.
- Expand and test the orbit computation toolset to include attitude mod-

elling and torque calculations for Space Resident Objects (SROs).

- Carry out trajectory analysis of a number of SROs to determine the impact of object torque and spin characteristics on orbit evolution.
- Develop visualisation methods to verify and characterise the computed torque models .
- Acquire and analyse a database that is representative of the orbits of the current constellation of space debris in order to understand the scale of the problem domain and from which to select relevant sample SROs for analysis.
- Develop novel ideas for instrumentation to further test the space environment's impact on the tumbling behaviour of SROs and for validation of the simulation methods developed.

4.1.3 Scope of study

The scope of this research is to model objects which will stay in orbit for years to decades. Non-conservative forces which cause de-orbiting (such as aerodynamic drag) will be neglected in light of this. The objectives will be applied to SROs with a view to analysing changes in orbital regime - for example "Zombie satellites" which are placed in a graveyard orbit above GEO and which are at risk of re-entering the busy operational space at GEO. This research does not apply to SROs with a short lifetime (months to years), but to those which will continue to orbit for many years.

4.2 Definition of conventions

In this chapter, the following conventions will be used:

- Right-handed torque convention is used, as shown in Figure 2.20
- The body frame of the SRO is defined by its origin and axis directions. The origin is either the centre of mass (CoM) or the geometric centre of the SRO, depending on the object modelled. The latitude and longitude in the body frame are defined with the x-axis representing 0 deg latitude and longitude. Latitude goes from -90 deg on the -z-axis to 90 deg on the +z-axis, and longitude defined in the $x-y$ plane as is done conventionally for the Earth, in the range -180 deg to $+180$ deg.

4.3 Radiation torque modelling

4.3.1 Torques exerted by radiation

Radiation pressure forces can be calculated for geometrically complex objects using the pixel array method [40]. The total radiation pressure force is exerted at a particular point, the CoP, determined by the geometry of the object. For perfectly symmetric objects, the CoP is at the geometric centre of the object. For real space objects, this may be different to the CoM. This may be due to composite materials (e.g. a piece of MLI attached to an aluminium structural member, or a large solar panel attached rigidly to a satellite bus). The difference between the CoP and CoM leads to a force acting about a moment arm, causing a net torque. This torque acts to perturb the attitude of the object. As the source of torque in this study is the radiation source (primarily the Sun), the resulting effects on attitude motion may be counter-intuitive due to the specific material and geometric characteristics of the SRO, combined with the nature and position of the radiation sources.

An example of the radiation torque calculation for individual radiation pixels is shown in Figure 4.1. In this diagram, there are three sample rays. Ray 1 intersects the satellite body and exerts an anticlockwise torque about the centre of mass in the xy-plane. This torque is negative by the right-handed convention, as the y-axis points into the page. Ray 2 exerts a larger torque in the opposite (clockwise)

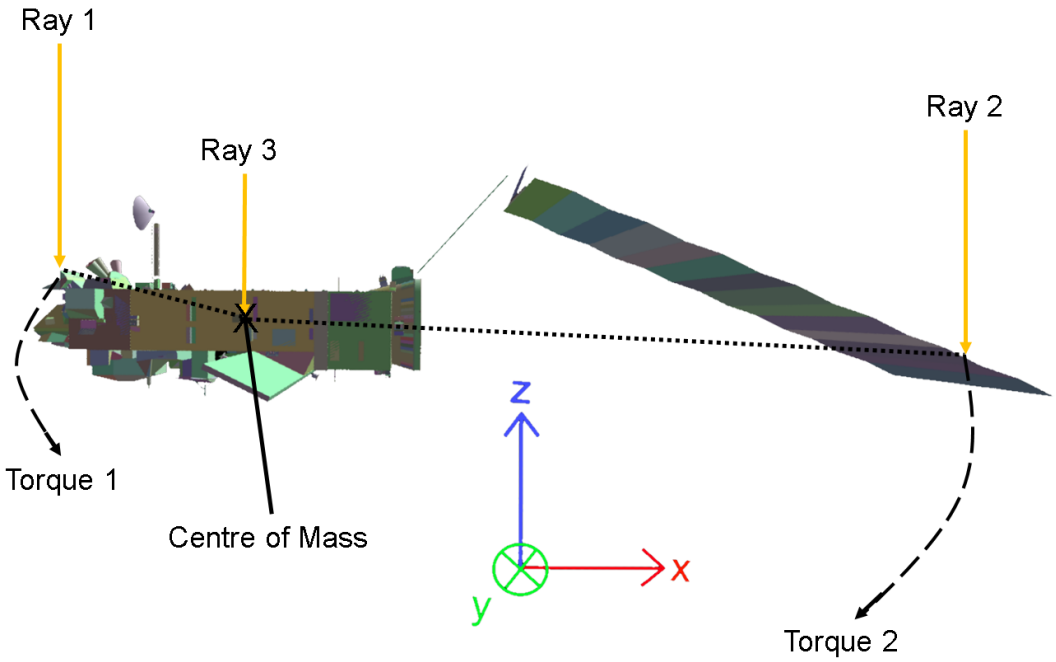

Figure 4.1: A diagram showing how individual rays exert torques

direction, as it intersects the satellite body on the opposite side of the centre of mass compared to ray 1. Ray 3 does not exert a torque as it intersects the body in line with the centre of mass; it exerts a net force. Each ray represents a single pixel in the computation stage, and the simulations use a summation over a pixel array that spans the SRO. In the above example, the sum of the three pixels would cause a net positive torque about the y-axis under the following assumptions:

- The energy, and therefore the imparted momentum, is the same for each ray
- The rays intersect components with identical optical and thermal properties
- The intersected components have identical surface normals and planar geometry.

This, in part, illustrates the complexity of the problem for real SROs.

4.3.2 The pixel array method

Figures 4.3-4.5 show the pixel array method for calculating radiation torques. There are four main factors that determine the magnitude and direction of the radiation torque:

- Orientation of the body with respect to the radiation flux
- Reflection characteristics of the intersected surfaces, which describe how incident radiation is reflected and absorbed
- SRO geometry, which determines the moments of inertia and the geometric asymmetries which lead to torques
- Shadowing and reflection effects - the effect of one part of an SRO shadowing other parts of the same object, and radiation reflected from one surface subsequently striking another component (this has been dubbed a "secondary intersection").

The geometry and material properties of a space vehicle / SRO are described in a text file using geometric primitives to define form; see Figure 4.2. The radiation source flux is described using an array of pixels. For a given orientation of the radiation source in the SRO body frame, each "pixel" of radiation is projected towards the SRO computer model and tested for intersection with the body. A successful intersection results in an intersection point (IP).

Once an intersection point is found, the moment arm for each intersection is calculated, from the CoM to the intersection point (IP). This is combined with the normal and shear forces exerted, and the torque for a given pixel is calculated:

$$\vec{\tau}_{pixel} = (\vec{r}_{IP} - \vec{r}_{COM}) \times (F_{normal}\hat{n} + F_{shear}\hat{s}) \tag{32}$$

where:

$\vec{\tau}$ is the torque for a given pixel

$\hat{n}$ is the surface normal vector at the intersection point

$\hat{s}$ is the vector in the plane of the intersected surface in the direction that the shear force acts

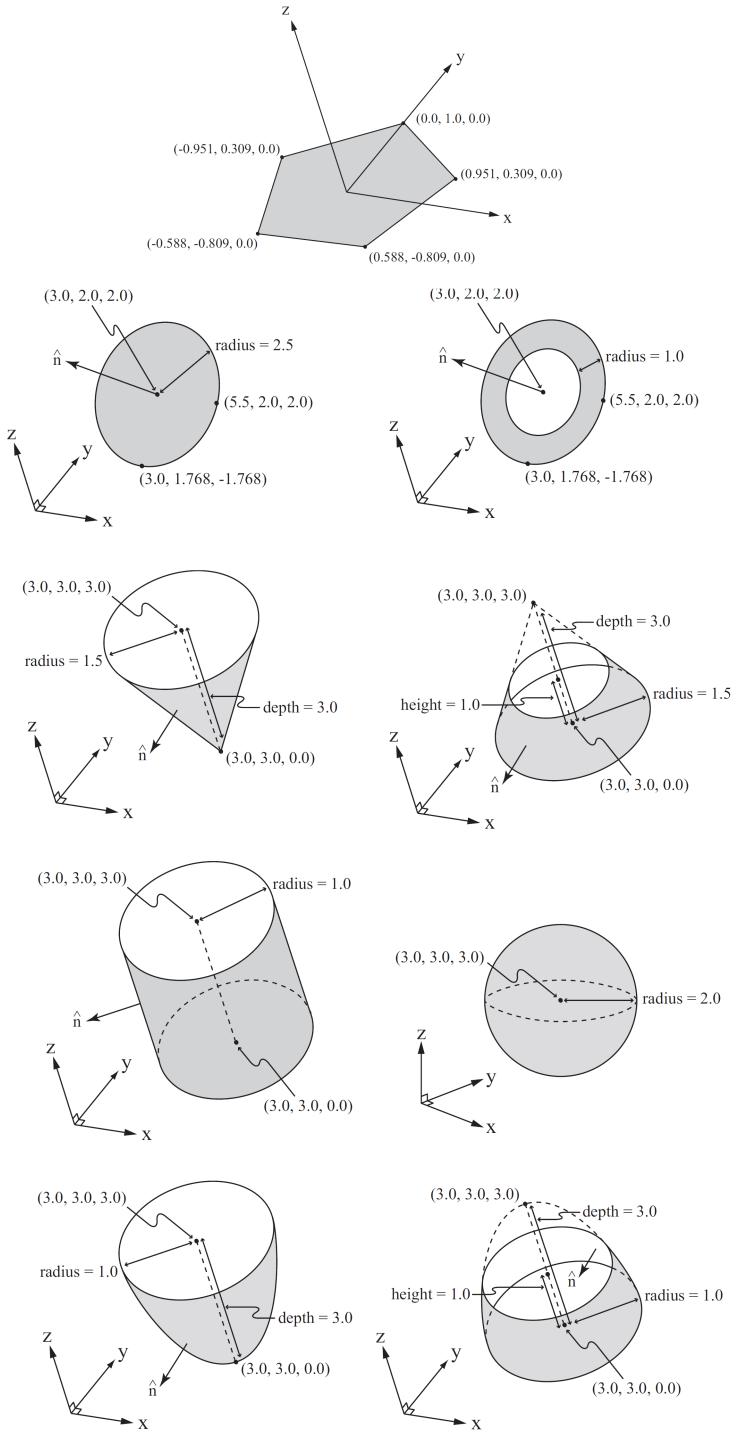

Figure 4.2: Shapes of object in the radiation modelling software - polygons, circular plates, planar rings, cones / truncated cones, cylinders, spheres, parabaloids and truncated parabaloids. Figure courtesy M Gulamali, 2006.

$\vec{r}_{IP}$ is the position vector of the intersection point in the spacecraft body frame

$\vec{r}_{COM}$ is the position vector of the centre of mass in the spacecraft body frame

The forces F_{normal} and F_{shear} are calculated using [13]:

$$F_{normal} = -\frac{EA}{c} cos(\theta)\{(1 + \mu\nu)\, cos(\theta) + \left(\frac{2}{3}\right)\nu\,(1 - \mu)\} \tag{33}$$

$$F_{shear} = \frac{EA}{c} cos(\theta) sin(\theta)\,(1 - \mu\nu) \tag{34}$$

with the following terms:

c = speed of light in vacuum = $299792458.0 m/s$

A = area illuminated on surface component

E = irradiance ($1364 W m^{-2}$)

θ = angle of incidence between incoming ray and the surface normal

ν = material surface reflectivity

μ = material surface specularity

If the material type is MLI (multi-layered insulation), an additional normal force is computed to calculate thermal emission as follows:

$$T^4_{MLI} = \frac{\alpha E cos(\theta) + \epsilon_{eff}\sigma T^4_{SC}}{\sigma\,(\epsilon_{MLI} + \epsilon_{eff})} \tag{35}$$

$$F_{MLI} = -\frac{2}{3}\frac{A\sigma\epsilon_{MLI} T^4_{MLI}}{c}\hat{n} \tag{36}$$

with the following terms:

T is the temperature (of MLI or spacecraft)

F_{MLI} is the force exerted on the MLI

$\alpha = (1 - \nu)$ = material absorptivity

σ = Stefan-Boltzmann constant

ϵ_{MLI} = emissivity of MLI

ϵ_{eff} = effective emissivity

The torques for each pixel are summed over the entire array and the resultant torque is computed. This yields the net torque about each Cartesian axis on the

SRO for the given orientation of the radiation source in the SRO body frame.

The pixel array is then rotated about the SRO. There are two schemes that can be used for placing the pixel array with respect to the SRO; conventional latitude/longitude spacing, or a spiral points method [9]. The spiral points method, visualised in Figure 4.6, has the advantage of spacing points evenly on a sphere about the SRO. With conventional latitude/longitude spacing, there is a higher density of points around the high and low latitudes, and a lower density of points around 0 latitude. The entire process is repeated for many positions of the pixel array with respect to the SRO. Typically, 5,000-20,000 orientations are used to build a detailed grid of points around the SRO. The final output is a text file containing a table of latitude/longitude of the radiation source in the body frame, along with the total torque exerted about each Cartesian axis for the given orientation. This pre-processing of the radiation pressure model enables a much quicker propagation runtime as the computationally intensive task of modelling each pixel is done in an offline step and only needs to be performed once per object.

In a typical simulation, there are 2.5×10^7 rays per incoming flux direction, and 1×10^4 different directions to give full coverage in the spacecraft body frame. This leads to 2.5×10^{11} ray/spacecraft intersections to be calculated. One full simulation takes approximately 3 days to compute on a UCL supercomputer with 2200 processing cores [95]. This method can be implemented using more modern General-Purpose Graphics Processing Unit (GP-GPU) architectures, or for broadly similar classes of space debris a set of reference models could be produced which can then be applied across a range of objects.

The output of the pixel array / spiral points algorithm is, for each axis of the SRO body frame, 1×10^4 discrete values of the computed torque. These values are then modelled in a more continuous fashion by using a modified Shepherd's method to fit a regular grid of torque values to the discrete data set. When specific torque values are required these are determined through bi-linear interpolation of the gridded values.

4.3.3 Torque maps

In order to visualise the contents of the text file containing the lookup table, a set of "torque maps" are plotted. These interpolate the output of the code onto a latitude/longitude grid. One torque map is required for the torque about each axis of an object, as these torques are mutually independent and information is lost if they are visualised together.

4.3.4 Attitude propagation through numeric integration of torques

In order to propagate the attitude of an object, the torque map is used. Based on an initial attitude, the torque is calculated based on a bilinear interpolation of the output of the pixel array torque calculations. The moments of inertia determine what change in attitude is caused by this torque, and numeric integration is used to propagate the attitude and give its time-evolution. The torque about each axis is found from the torque map for that axis separately, and each axis is propagated independently.

4.3.5 Assumptions and limitations

A limitation of this method is that the centre of mass of the satellite has to be defined in the body frame and is fixed from the beginning of the simulation, and is constant for the entire simulation. For the purposes of modelling rigid objects this is an acceptable approach, however for active satellites and spacecraft, this would require modification. This is because the mass and centre of mass change for active objects; fuel is burnt, the fuel sloshes in fuel tanks and these change the centre of mass. For space debris the assumption of a rigid body is also made.

The limitations of the solar radiation model are that the flux density is modelled as uniform and constant[5] - that is, solar cycles and spatial intensity variation are ignored. The frequency distribution of the radiation is also ignored but this is necessary as detailed frequency-dependent optical properties are not available for the modelled materials.

[5] although in application the computed torques are scaled appropriately based on the probe-sun distance

A high-fidelity model of the SRO is generated from primitive shapes, via the "USER" text input file containing the SRO geometry	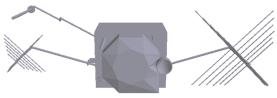
An array of pixels is generated based on the required incoming flux direction; this array spans the entire spatial extent of the spacecraft	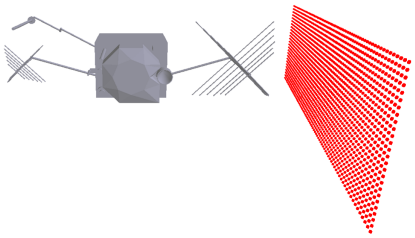
Rays are "emitted" from the centre of each pixel in the array	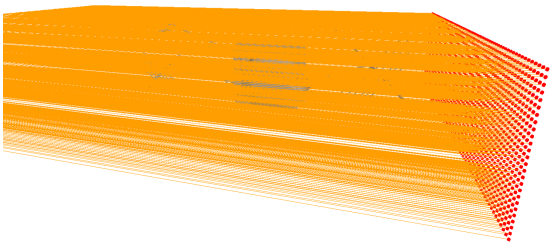
The intersection points (IPs) of each ray with the SRO surfaces are calculated	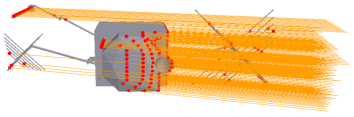

Figure 4.3: The pixel array method, showing how torques are computed

The surface properties of the SRO are read from the input file for each of the intersected components	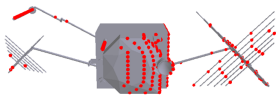
The surface normal is computed at each IP and the specular reflection components are calculated for each ray	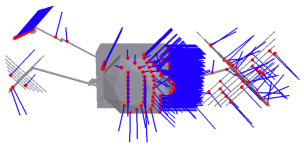
This is followed by the diffuse components for each ray, and these are summed with the specular components, the direct radiation force and the forces due to thermal emission of MLI to give the net force and hence calculate the total torque.	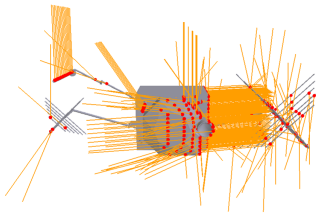

Figure 4.4: The pixel array method (continued)

4.4 Computational attitude modelling

4.4.1 Method diagram

The simplest way of presenting the overall method is visual (Figure 4.7). This flowchart shows some of the complexity involved in implementing the method. The method is broken down into its constituent components in the following sections.

The torques calculated in the previous section must be correctly implemented in an attitude propagation model to generate meaningful results that describe the attitude motion of an SRO based on the natural torques of the space environment.

4.4.2 Force and orbit modelling

The force models used in this research must enable prediction of the broad orbital motion of SROs, but the focus is not specifically on force modelling. The choice of force models must enable a comparison between different attitude models - it acts as a base upon which further research is built. Of the force models described in the scientific background, only a subset are necessary for the purposes of this

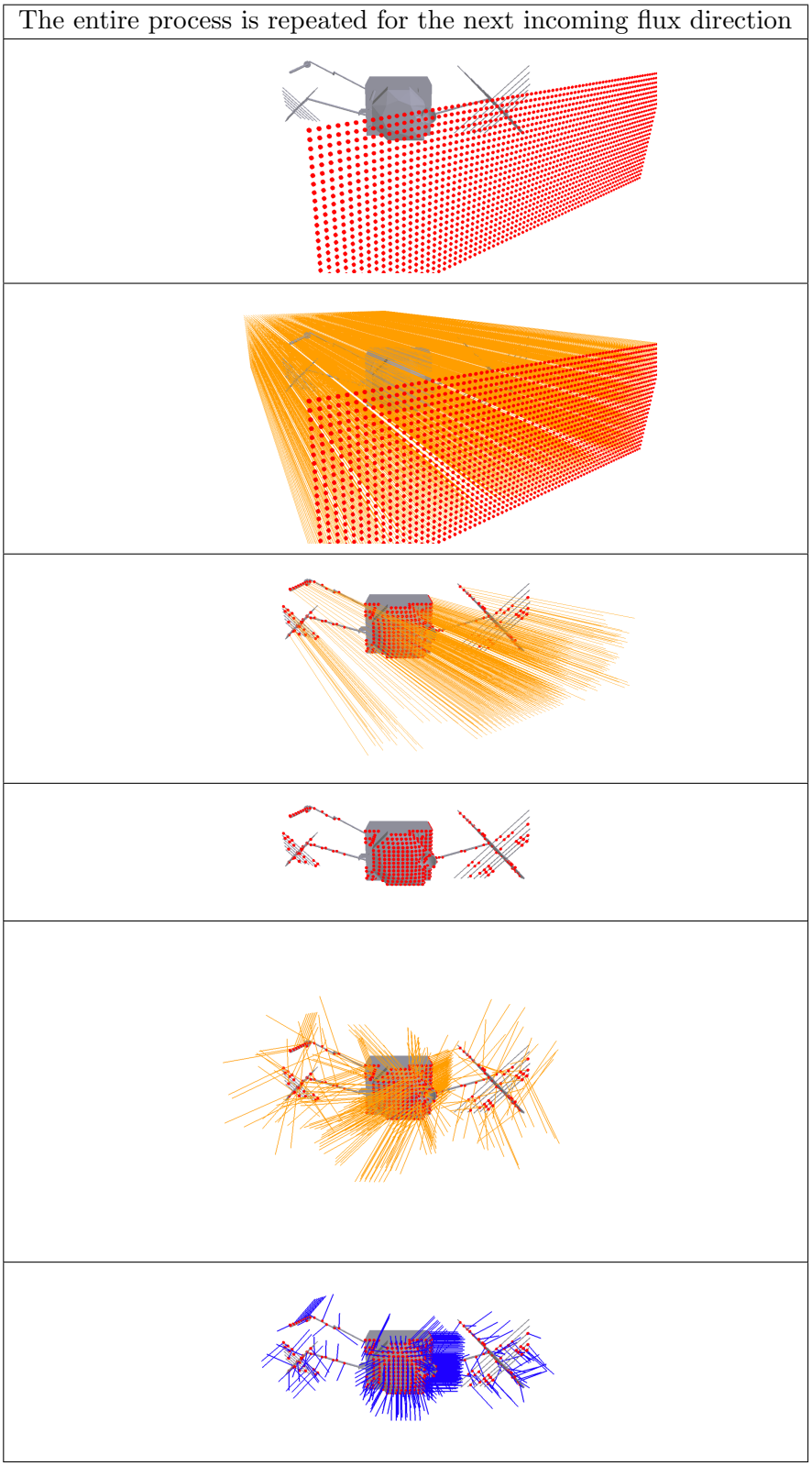

Figure 4.5: The pixel array method (continued)

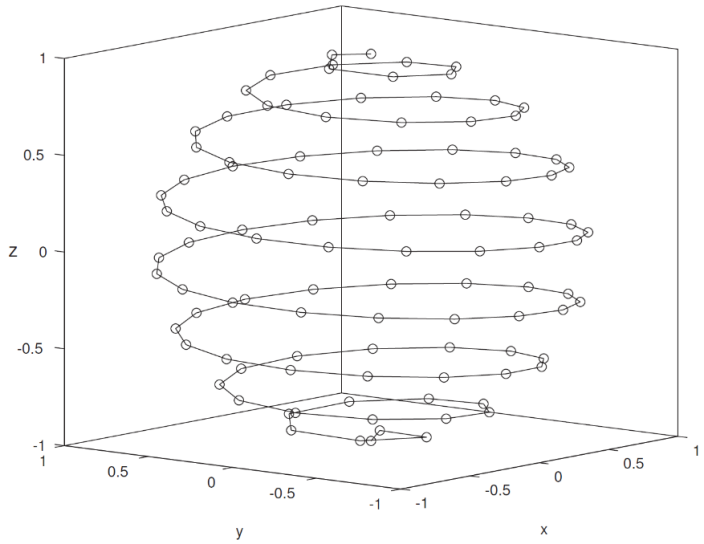

Figure 4.6: The spiral points algorithm, used to place points uniformly on a sphere. Courtesy [9]

research. A set of basic force models were chosen to enable comparison of a fixed attitude to a tumbling object. These include monopole Earth gravity, both lunar and solar gravity, and SRP.

4.4.3 Torque and attitude modelling

The approach taken here is to separate the torques into a component about each axis in the OF frame, using the BF vectors to calculate attitude-dependent forces and torques. The torques are summed to give a total torque about each OF axis. The OF is then rotated using Euler angles, and the resulting quaternions are calculated and multiplied to give one overall quaternion for the integration timestep. This gives an angle and an invariant axis for the rotation - both of which are useful in the analysis of the attitude motion. The rotation is applied and the new vectors of the BF in the OF are calculated.

From the angular acceleration about each axis, the invariant axis and angle of rotation over a single timestep are calculated. This is beneficial as we can easily log and plot the invariant axis and how this changes over time. The invariant axis and angle are used to calculate a quaternion for the rotation, and the new object vector relative to the body frame is calculated. The use of quaternions resolves the problem of gimbal locking, which is a big problem when using Euler angles,

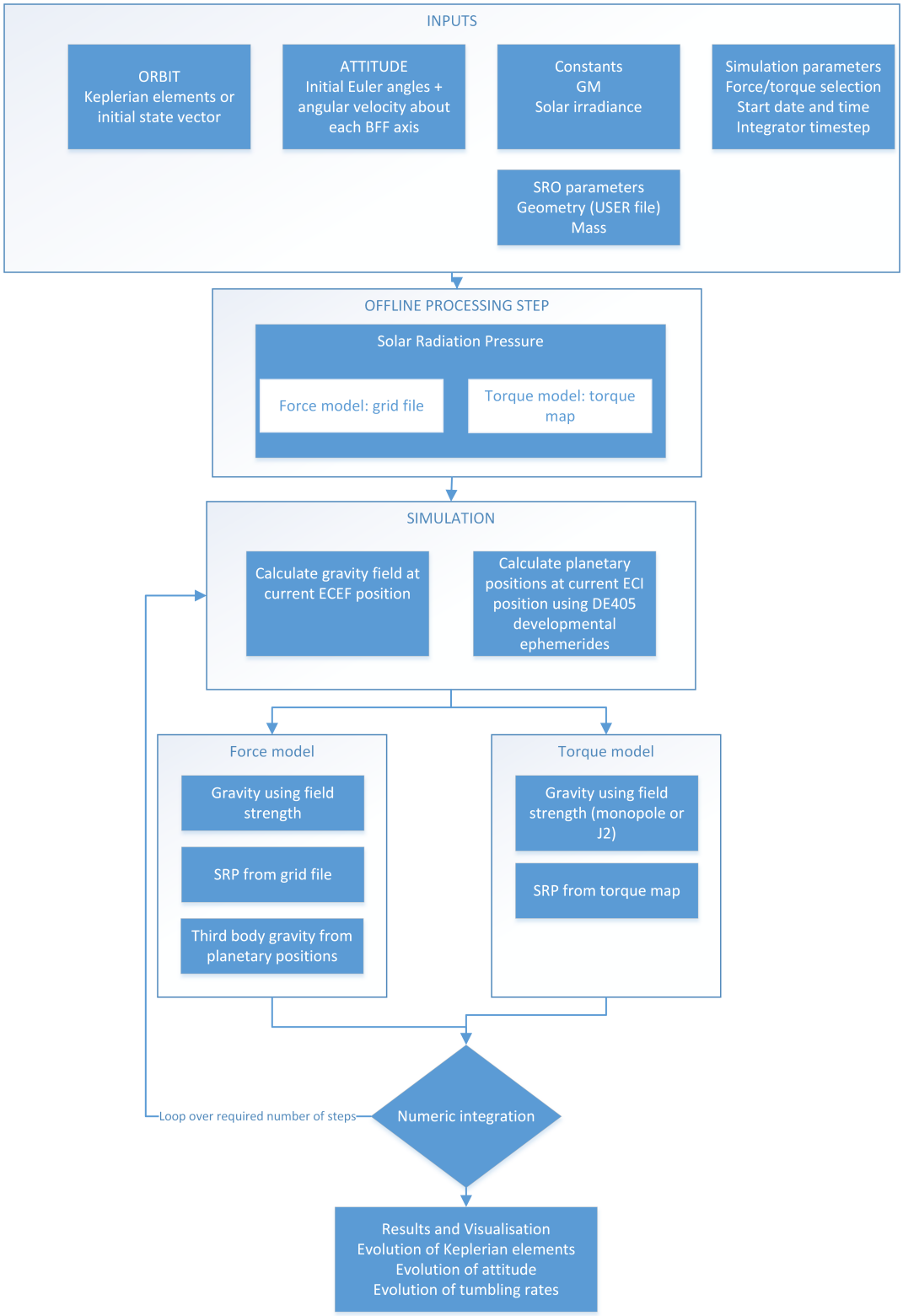

Figure 4.7: The computational method implemented for this research

and it also requires calculation of the invariant axis at each step which is useful in visualising how the object is tumbling. If an object were tumbling about a fixed axis, the invariant axis would not change.

As space debris orbits are uncontrolled, attitude and tumbling are also important in determining how these forces apply to each object. Changes in attitude lead to changes in surface force (such as SRP) and could have an impact on orbital stability. Understanding in this area could lead to improved models of the spatial distribution of space debris, which is crucial in tasking radar and optical stations for observation. It could also lead to innovative methods for influencing debris for de-orbiting. Gravitational torques arise due to the non-uniformity of the gravitational field around the Earth, which cause variations in the force acting on different mass elements of an SRO. For the main results, other torques are ignored. An analysis into the effect of the Lorentz force and potential torques associated with it was conducted, and the paper associated to this is given in appendix 9.3.4.

4.4.4 Assumptions

The assumptions made in order to simplify the torque modelling problem are:

- Rigid body - the SRO is assumed to be rigid
- Spherical earth - a monopole Earth gravity model is used
- No internal torques - the SRO is assumed to be passive with no attitude control system, sloshing of fuel or crew movements

Although more sophisticated force models could be used, such as a higher-order gravity field expansion, these have been omitted to clarify the extraction of dynamics caused solely by tumbling motion. More complicated models with many different forces would have complex dynamics which obscure the contributions from each individual mechanism.

4.4.5 Propagation methods

The key to computational orbit propagation is numeric integration of the differential equations which govern the SRO motion dynamics.

For orbit prediction through numeric integration of initial conditions, fourth-

and 7/8th-order Runge-Kutta algorithms are used here as a trade-off between accuracy, numerical stability and computational complexity [96, 97]

4.5 Orbit-attitude coupling

In the implementation of the above methods, the simplest approach is to use the same timestep for both orbit and attitude. This means that the attitude and position (as well as their time derivatives) are calculated completely in each step. The problem with this method is that the attitude dynamics typically evolve on a much shorter timescale. If an object is tumbling with a period of 5s, it is rotating by 72 deg per second. To capture this dynamic requires a timestep of 1/100s, such that each timestep corresponds to a change in attitude of less than 1 deg. In response to this, the modelled objects are ones for which the rotational timestep and orbital integration timestep are comparable, with rotation rates of $0.1 - 4\,\mathrm{deg}/s$.

Chapter Summary

This chapter has presented methods for calculating radiation torques, and for modelling spinning objects in orbit subject to the modelled torques. These methods are applied initially to specific test objects designed to validate the code; the results for this are presented in Chapter 5. The methods are then applied to real-world objects in Chapter 6 followed by analysis and discussion of these results.

5 Results I

Chapter Outline

The previous chapter described the method which has been implemented in code. In order to check that the code is correct, verification steps are necessary. There are several steps to this process - ranging from individual tests of specific code classes, numeric tests of entire modules, and functional tests of non-numeric classes such as plotting and file input/output. The focus of this section is the numeric testing of the entire software, in order to check that the code is working as expected.

Numeric tests compare manual calculations on specific test objects, against the output of the code for the same test objects. These objects are chosen to enable simple manual calculations, but also designed in such a way that their physical characteristics utilise and exploit different sections of the code. The two main tests are a null test - that is, an object for which no torque is expected gives a null output from the code, and a non-null test where the hand-calculated torque should match the output of the software.

Further to these, the results of initial simulations are presented as these give important insight into the initial conditions for the main test cases presented in the following chapter.

Finally, a numerical analysis of the current space debris constellation is given. This is to set the context of orbital regimes for current debris. This chapter is self-contained, whereas for the main results in Chapter 6 the analysis and discussion are separated.

5.1 Radiation torques

Radiation torques are a result of asymmetry in shape. To exploit this, two simple shapes have been chosen for the purposes of validation: a uniform sphere, and a set of flat painted plates with offset centres of mass. The surface properties of these have been chosen to exploit nuances in the radiation pressure modelling scheme, and both are described in detail in the following sections.

Input parameter	Value
Pixel spacing	0.01m
Spiral points	10,000

Table 5.1: Input parameters for the flat plate radiation torque calculations

5.1.1 Flat plates

For the non-null test, a set of square plates were created. Each has its geometric centre along a particular Cartesian axis, and the centre of mass at the origin. This acts to exert a radiation torque about a specific axis, based on the offset from the CoP (where the radiation force acts) to the CoM (about which the object tumbles). Of course, this is not necessarily a realistic object but for the purposes of testing it is useful. A real-world example which comes close to the test object might be a piece of MLI attached to a small but dense strip of metal - the metal causing the centre of mass to be within the strip, and with the MLI attached having a large area but very low mass. Such a simple object enables manual calculations to be compared to simulation results, which ensures that the simulation results agree with the theory.

Each plate has an area of $1m^2$ and so with the CoM at the origin, the CoP is displaced from this point by 0.5m and thus the moment arm is 0.5m. The thickness is a nominal 1cm, and both $\mu = 0$ and $\nu = 0$. The simulations for these objects are at 1cm pixel spacing. The simulation input parameters are summarised in Table 5.1. These test objects are visualised, along with the corresponding torque maps, in Figures 5.1-5.6 and a summary of the results is given in Table 5.2.

The important trend for the X- and Y-plates is that the variation in torque is only dependent on latitude. This is intuitive, as the area of the object presented to the radiation flux is the same for any longitude at a given latitude in the object body frame. The difference between the X- and Y- plates is the sign of the torque. This is explained by the geometry as shown in the plate visualisations. At high latitudes (i.e. the radiation arriving down the z-axis), the torque on the X-plate is negative based on the right-handed convention. In contrast, the torque on the Y-plate is positive in the same scenario, but about the y-axis instead of the x-axis. The torque on the Z-plate is dependent on both latitude and longitude. The torque

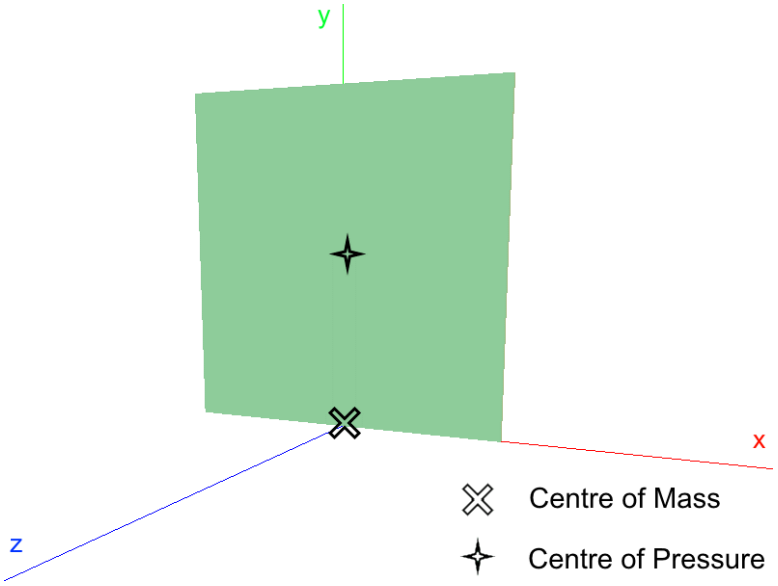

Figure 5.1: A visualisation of the plate designed to exert a torque about the x-axis

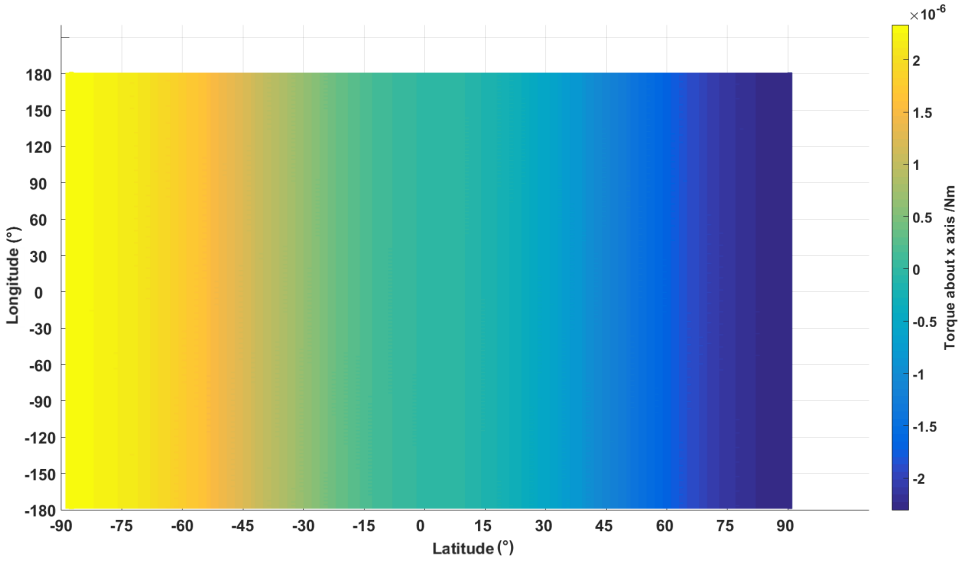

Figure 5.2: A torque map showing the radiation torques about the x-axis on the x-plate, with $\mu = 0$ and $\nu = 0$

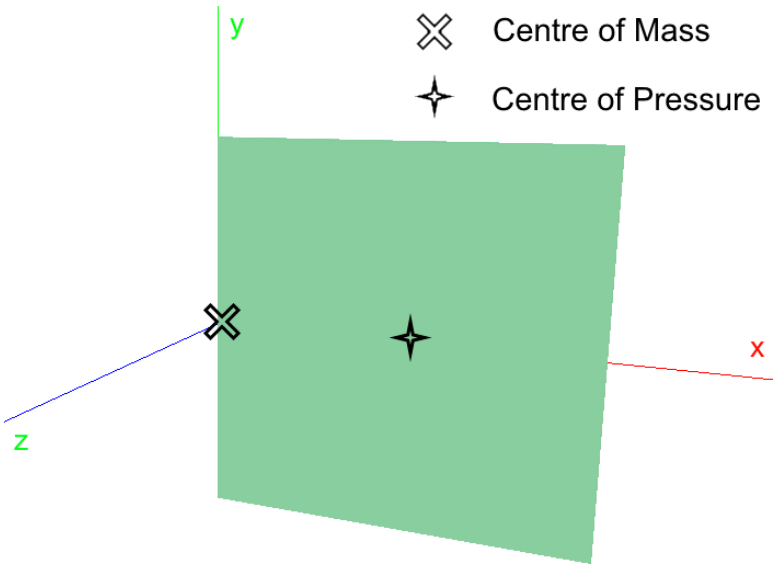

Figure 5.3: A visualisation of the plate designed to exert a torque about the y-axis

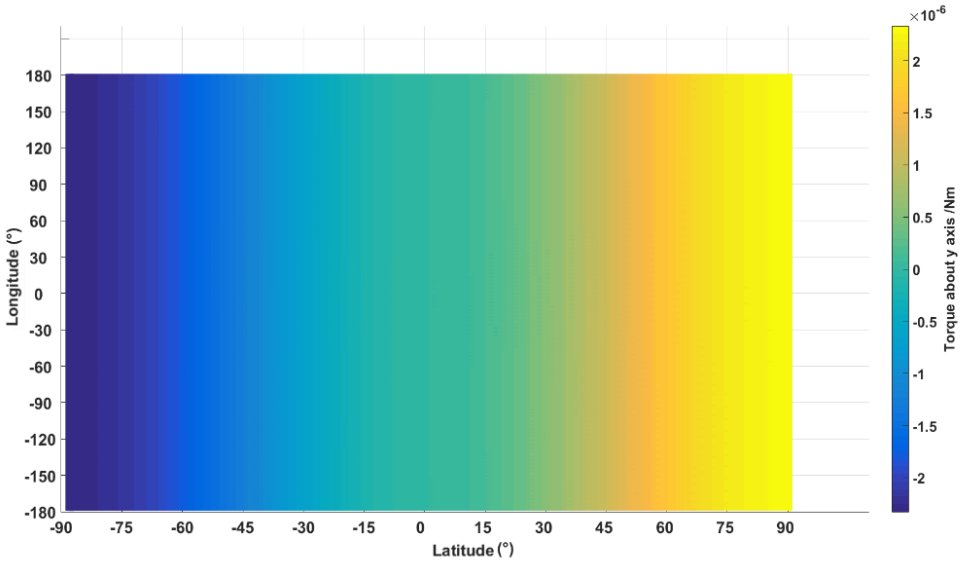

Figure 5.4: A torque map showing the radiation torques about the y-axis on the y-plate, with $\mu = 0$ and $\nu = 0$

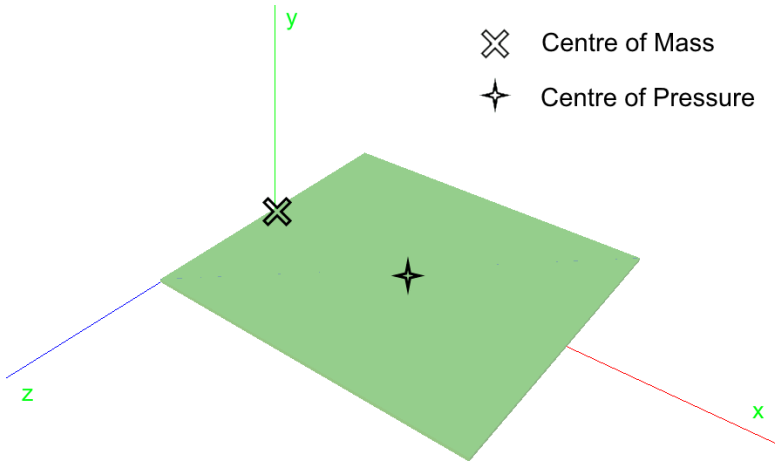

Figure 5.5: A visualisation of the plate designed to exert a torque about the z-axis

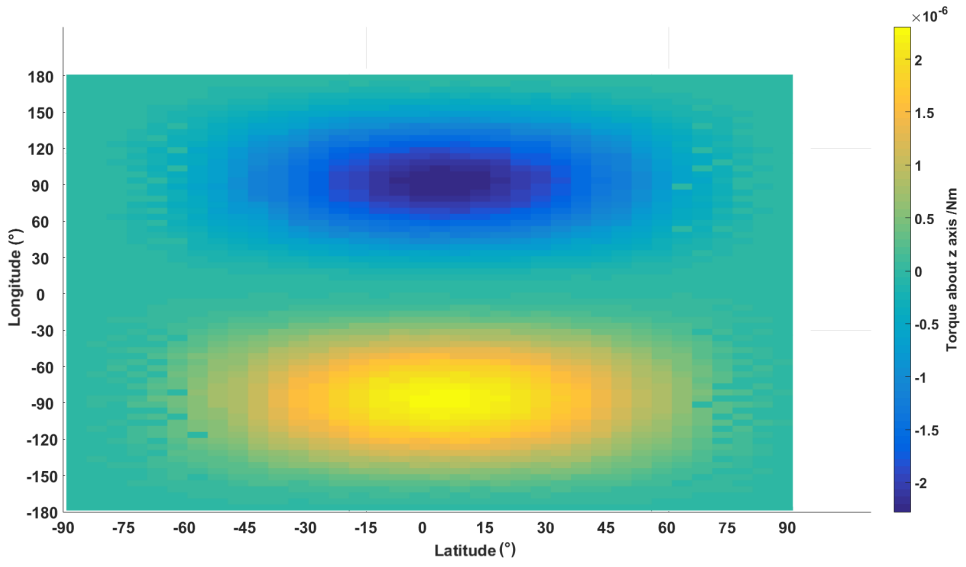

Figure 5.6: A torque map showing the radiation torques about the z-axis on the z-plate, with $\mu = 0$ and $\nu = 0$

is null for zero longitude, as the radiation source is then in XY plane where the area of the plate is negligible in comparison to the area of its main face.

Based on the theory, the force exerted on a flat plate is given by Equations 33 and 34. The torque depends only on the normal force for purely diffuse reflections, as the shear force acts in plane with the torque arm. Based on the input parameters, the torque can be calculated. θ is measured from the normal. The comparison made here is for $\theta = 0$.

From Table 5.1, and using $\mu = 0$ and $\nu = 0$:

$$F_{normal} = -\frac{EA}{c} = -1367 * 1/(2.997 \times 10^8) = -4.561 \times 10^{-6} \tag{37}$$

$$\tau = r_{CoM} - r_{CoP} \times F_{normal} \tag{38}$$

As the torque arm is 0.5m and is perpendicular to the direction of the force, and given the right-hand convention (i.e. a torque arising in a force coming in the -Z direction):

$$\tau = 0.5 * -(-4.561e - 6) = 2.28 \times 10^{-6} Nm \tag{39}$$

The computed torque in this scenario is $2.33 \times 10^{-6} Nm$. Further manual calculations were made for each plate; the results for both the square plate simulations, and the manual calculations to compare these to, are given in Table 5.2. There is a good agreement between the theoretical hand calculations and the computed results, despite the relatively coarse simulation parameters. Torque modelling errors at the 1cm pixel resolution are two orders of magnitude smaller than the torque value. Note that every computation has given a result that is larger than the expected torque - this is due to edge matching. The final column of pixels hangs slightly over the edge of the object geometry, in this instance by approximately 0.5cm, and this causes an "extra" row of pixels to exert a torque. This is described in more detail in the next section with the spherical test object.

This analysis shows that, for an object with an expected radiation torque, the software is working correctly and the differences between the code and the theory

Plate	Manual torque result /Nm		
	τ_x	τ_y	τ_z
X	**2.25E-06**	0.00	0.00
Y	0.00	**2.25E-06**	0.00
Z	0.00	0.00	**2.25E-06**
	Computed torque result /Nm		
	τ_x	τ_y	τ_z
X	**2.33E-06**	2.09E-08	1.15E-08
Y	6.05E-08	**2.32E-06**	1.45E-08
Z	2.26E-08	1.17E-08	**2.30E-06**
	Difference /Nm		
	$\delta\tau_x$	$\delta\tau_y$	$\delta\tau_z$
X	-8.00E-08	-2.09E-08	-1.15E-08
Y	-6.05E-08	-7.00E-08	-1.45E-08
Z	-2.26E-08	-1.17E-08	-5.00E-08

Table 5.2: Comparisons of manual calculations of torques on the plate test objects with simulation results for $\theta = 0$. The first table gives the manually calculated result, the second gives the output of the simulations, and the third gives the differences between the two

have been accounted for.

5.1.2 Spherical object

For the null test, a sphere was chosen. For a spherical object, with uniform surface properties and the centre of mass at the geometric centre of the sphere, we do not expect a torque to be exerted by radiation pressure. This is due to complete symmetry; for a uniform incident radiation flux, each photon impinging on the surface of the sphere is balanced by an equivalent photon intersecting at the mirror image of the first intersection point. This is true for all incident angles. In the test simulations, the sphere has a radius of $5m$. Theoretically the torque on the sphere is zero. The computed torques are small, but the result depends on the pixel spacing used in simulations. The results from radiation pressure modelling of the sphere with varying pixel size are given in Figure 5.7, and as it is a log-log plot, and the gradient is 2, the relationship between pixel spacing and the average torque is quadratic - that is, halving the pixel spacing will give a $\sqrt{2}$ decrease in the average torque due to edge matching. This is shown in Figure 5.11.

There is a trade-off between simulation runtime and pixel spacing - a smaller

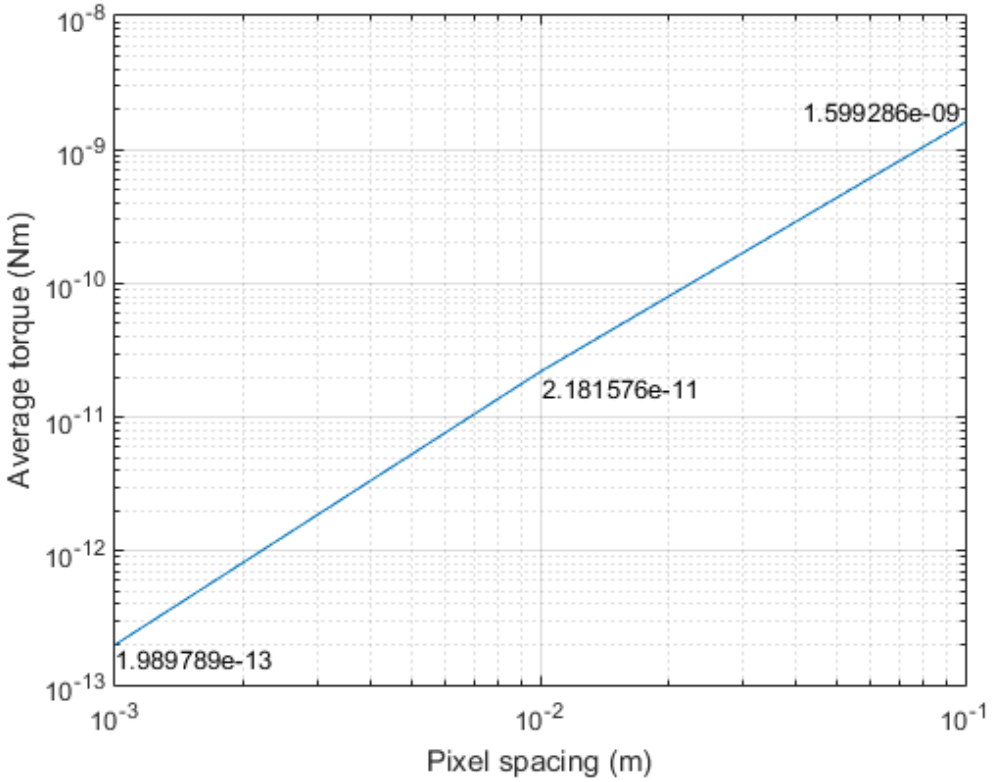

Figure 5.7: The effect of increasing pixel spacing on the torque exerted on a sphere with the average torque exerted labelled for each data point. Here, the average is taken across the three Cartesian components of torque.

pixel spacing gives a more accurate result but requires longer to compute. This is shown in Figure 5.9 and Table 5.3. A smaller pixel spacing captures the highest level of fidelity of each facet of the SRO, and minimises edge-matching errors. A typical pixel spacing for radiation force modelling is 1/1,000-1/10,000th of the largest object dimension, so for the 5m sphere a 0.5mm spacing would give good detail. Table 5.3 shows the runtimes on an i7 2720qm CPU, and these scale approximately with the inverse square of the pixel spacing.

Figure 5.9 shows a quadratic relationship ($o(n^2)$) between pixel spacing and simulation runtime. In order to simulate with 10x greater resolution in each dimension of the pixel array, there are 100x more calculations and thus the results are intuitive. To simulate a 5m sphere with 0.5mm pixel spacing would require High Power Computing (HPC) facilities in order to give a reasonable runtime, as it would take an estimated 100 days to complete 10,000 spiral points on an i7-

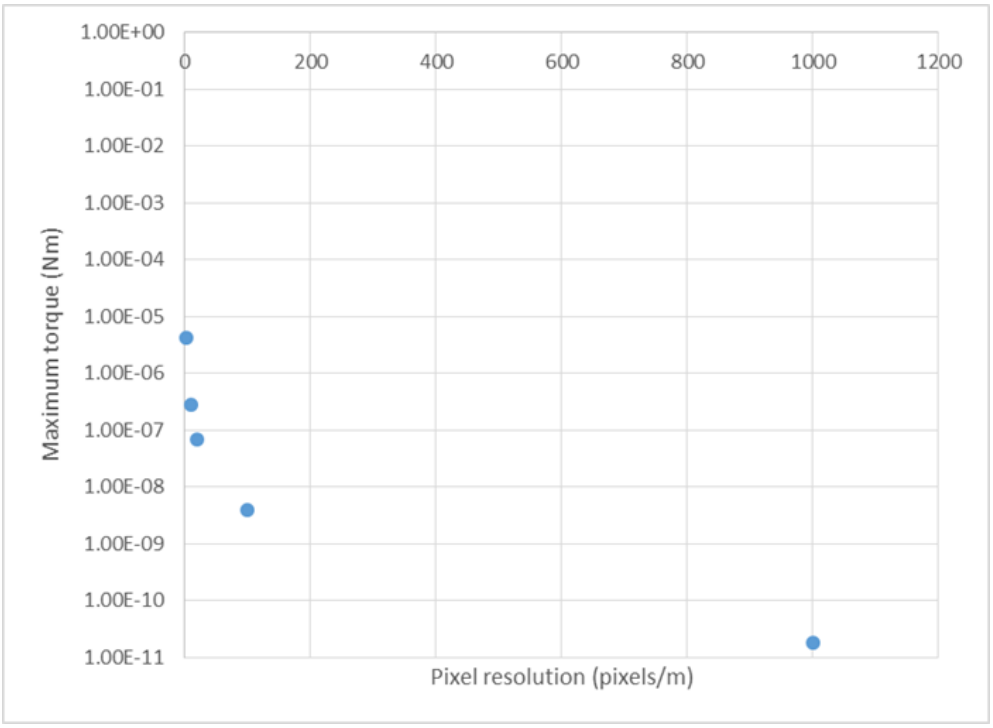

Figure 5.8: The effect of increasing pixel resolution on the maximum torque exerted on a sphere

2720qm processor. In order to strike a balance between the two, a pixel spacing of 0.01m has been selected, and 5,000-10,000 spiral points.

The radiation pressure code was run for several different pixel spacings, ranging from 10cm down to 1um. The results of these simulations are given in Table 5.3 and Figure 5.8. A comparison of the runtimes is also given in Figure 5.9.

These results show that the net torque exerted on the sphere is dependent on the pixel spacing. This is because, for lower pixel resolutions, there is a small mismatch on one edge of the pixel array. This is known as an edge matching error; an extra line of pixels on one edge contribute to the torque, where no interactions are expected. The solution to this error is to use a finer pixel spacing. Based on testing, the pixel spacing should be $\frac{1}{1000}$ of the longest object dimension.

Figure 5.10 visualises the torque on a 50cm sphere at a high resolution of 1cm and the results show small and seemingly random errors in the torque, caused by edge matching.

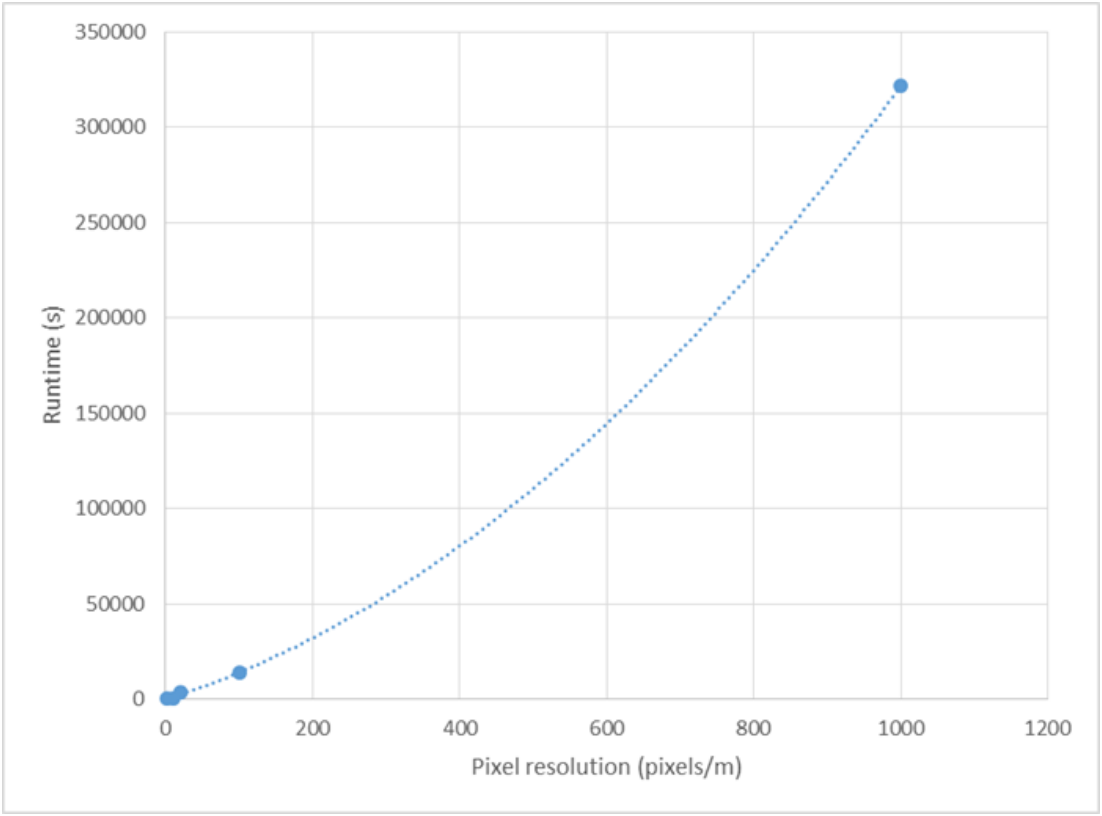

Figure 5.9: The effect of increasing pixel spacing on simulation runtime

5.1.3 Nanosatellites

Two Kicksat-style sprite satellite models were created. They are painted in such a way to exert a radiation torque - see Figures 5.12 and 5.13. The half that is painted black absorbs light, whereas the half that is painted white reflects the light, both in a diffuse manner. This difference means that there is a greater force on the white half (due to the "rebound" of light on the white half transferring more momentum than the absorption on the black half). Thus there is a net force "pushing" about the centre of mass, that is exerted in the middle of the white half of the sprite. This results in a torque. The two sprite satellite models differ in how the two sides are painted; one of them is identical on the front and back, whereas the other has opposite colours front and back. The sprite which is identical on both sides will simply oscillate under radiation torques alone, under favourable initial conditions due to the symmetry in torque. With a given attitude, if the sprite is rotated 180 deg about the y- or z- axis, the torque is the same in magnitude but opposite

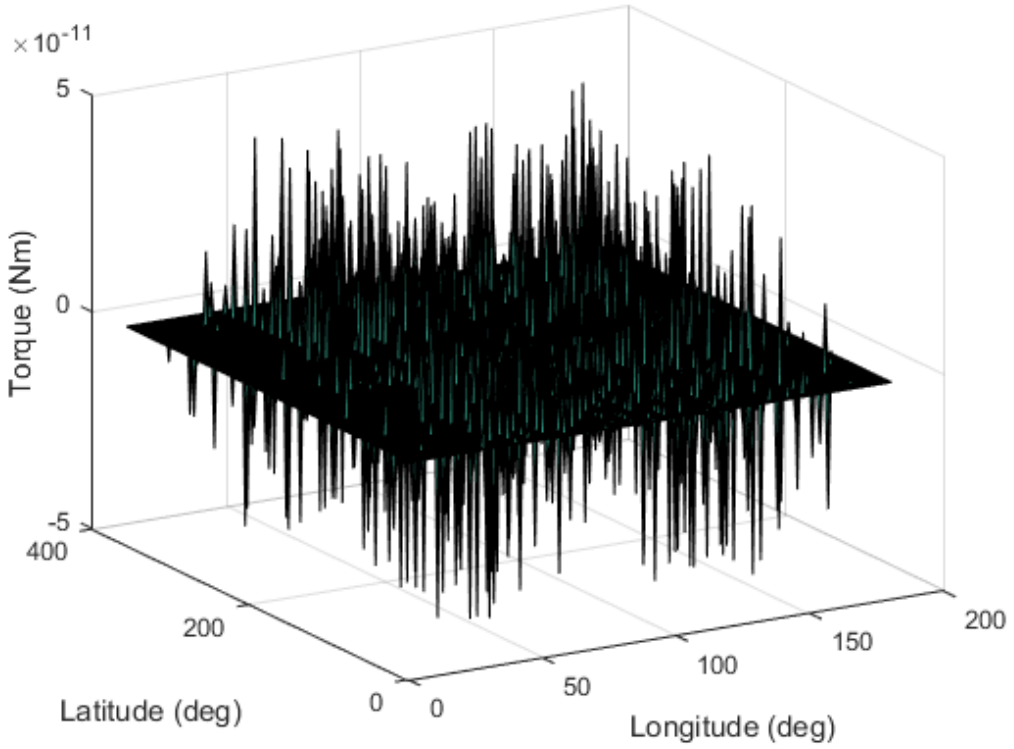

Figure 5.10: The torque map for a $50cm$ sphere at $1cm$ pixel spacing, presented in 3d to show that the results are sporadic and due to numeric precision

in direction. The sprite which is painted differently will spin faster and faster as the torque is in the same direction independent of the attitude of the sprite. The paint schemes have been dubbed "oscillatory" and "spin-up" respectively.

	Maximum torque about axis (Nm) —			Mean torque about axis (Nm)			
Pixel Spacing (m)	X	Y	Z	X	Y	Z	Runtime (s)
0.5	4.23E-06	4.22E-06	4.12E-06	-1.09E-08	4.06E-08	-2.65E-08	102.7
0.1	2.74E-07	2.75E-07	2.72E-07	-2.32E-09	3.18E-09	2.02E-09	354.4
0.05	6.85E-08	6.87E-08	6.81E-08	-4.78E-10	8.68E-10	-4.86E-10	3691.2
0.01	3.85E-09	3.85E-09	3.55E-09	1.06E-11	6.08E-11	-9.30E-11	13883.9
0.001	1.79E-11	2.18E-11	9.14E-13	3.43E-12	-1.36E-12	-2.19E-13	321498.8

Table 5.3: The effects of increasing pixel resolution on edge-matching torque errors on a sphere, and the runtimes associated with each simulation

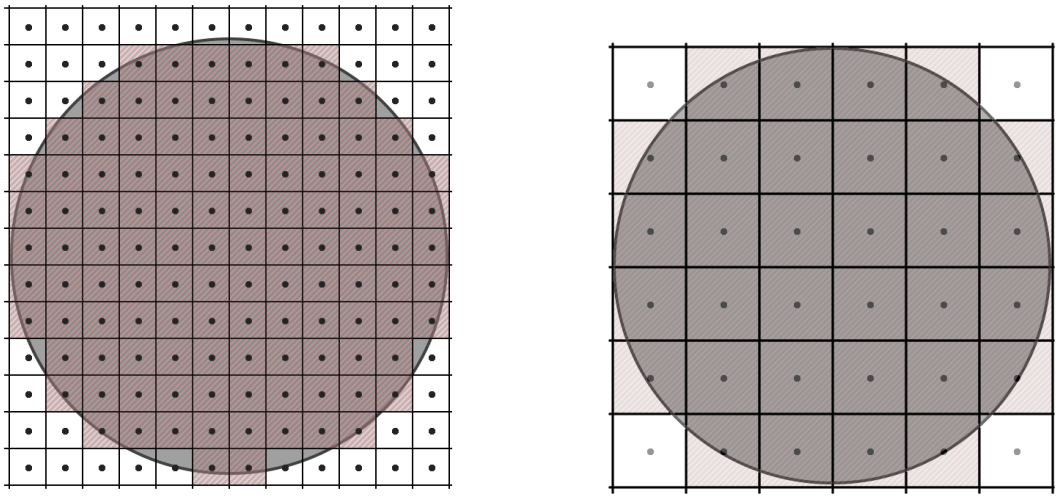

Figure 5.11: The effect of pixel spacing on edge-matching errors. A comparison of a high and low pixel resolution on the fidelity of a radiation pressure simulation. The large grey circles are the simulated body, and the dots represent each pixel bounded by the grid. The coloured pixels indicate which ones intersect the object.

Based on Figure 5.13, looking down the z-axis in the -z direction, we can split the torque calculation into the right (white) and left (black) halves. A is the total area of the sprite, and so the area of each half is $\frac{A}{2}$. θ is the angle of the incoming ray with respect to the normal (z axis as shown in the figure). As both parts of the sprite are matte the reflections are entirely diffuse; ($\mu = 0$). Based on the colour, $\nu_{black} = 0$ and $\nu_{white} = 1$ and so for each half respectively (based on Equation 33):

$$F_{black} = -\frac{EA}{c} cos(\theta) \left[cos(\theta) + \frac{2}{3} \nu_{black} \right] \tag{40}$$

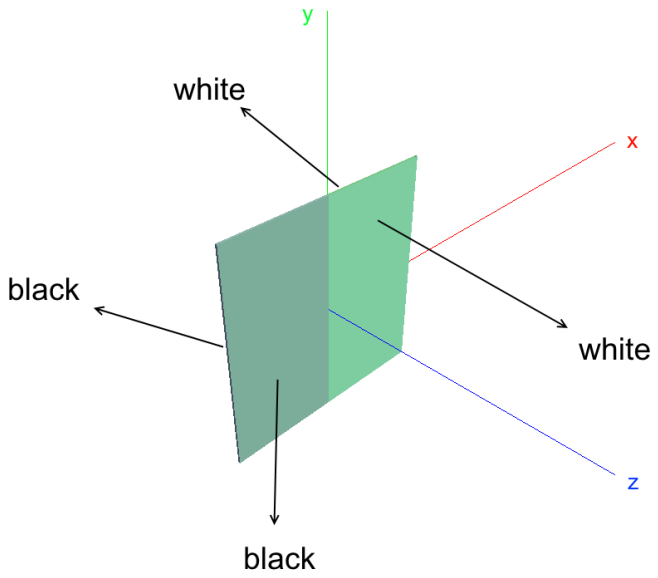

Figure 5.12: Oscillatory sprite satellite, painted in such a way that the radiation torque is dependent on which face of the sprite is illuminated causing oscillatory attitude motion

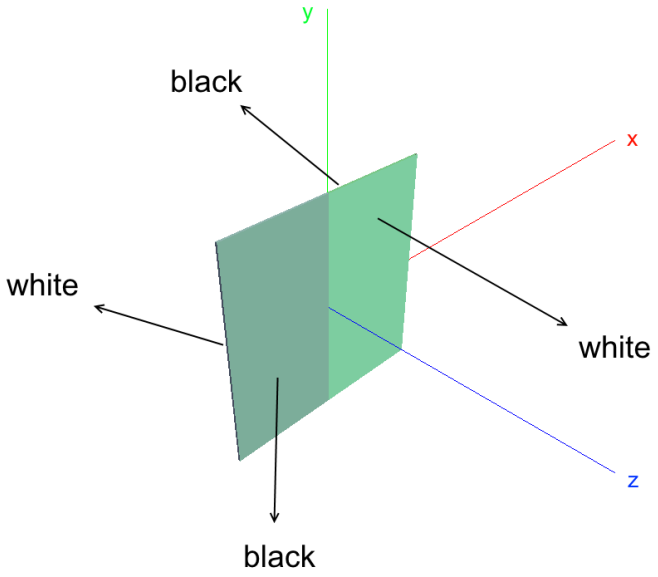

Figure 5.13: Spin-up sprite satellite, painted in such a way that the radiation torque is independent of the face of the sprite, causing continuous spin-up attitude motion

$$F_{white} = -\frac{EA}{c} cos(\theta) \left[cos(\theta) + \frac{2}{3} \nu_{white} \right] \tag{41}$$

Thus the total forces are:

$$F_{black} = -\frac{EA}{2c} cos^2(\theta) \tag{42}$$

$$F_{white} = -\frac{EA}{c} cos(\theta) \left[cos(\theta) + \frac{2}{3} \right] \tag{43}$$

The torques on each half add together to calculate the total, and the moment arm is $\frac{A^{\frac{1}{2}}}{4}$ for each half as the force is exerted in the centre of each half:

$$\tau_{black} = \left(-\frac{A^{\frac{1}{2}}}{4} \right) \left(-\frac{EA}{2c} cos^2(\theta) \right) \tag{44}$$

$$\tau_{white} = \left(\frac{A^{\frac{1}{2}}}{4} \right) \left(-\frac{EA}{c} cos(\theta) \left[cos(\theta) + \frac{2}{3} \right] \right) \tag{45}$$

$$\tau = \tau_{white} + \tau_{black} = \left(\frac{A^{\frac{1}{2}}}{4} \right) \left(-\frac{2}{3} \frac{EA}{c} cos(\theta) \right) \tag{46}$$

The net torque can thus be expressed as:

$$\tau = -\frac{EA^{3/2}}{6c} cos(\theta) \tag{47}$$

This equation was used to generate the maximum expected torques, as given in Table 5.2.

5.2 Parameters for test cases

The results of the main simulations of objects tumbling in orbit are presented in the following chapter. In order to decide what parameters should be used in the main simulations, some initial simulations were run.

An important factor for these simulations is timestep. This is used in numeric integration to have a balance between simulation precision and runtime. Figure 5.14 shows the deviation from a 0.01s timestep for a 0.1s, 1s and 10s timestep. Based on these results, a 0.01s timestep was retained for simulations.

Chapter Summary

This chapter has presented the results for initial simulations, for the purposes of verification of the code and in order to determine the input parameters for the main simulations which are presented in Chapter 6.

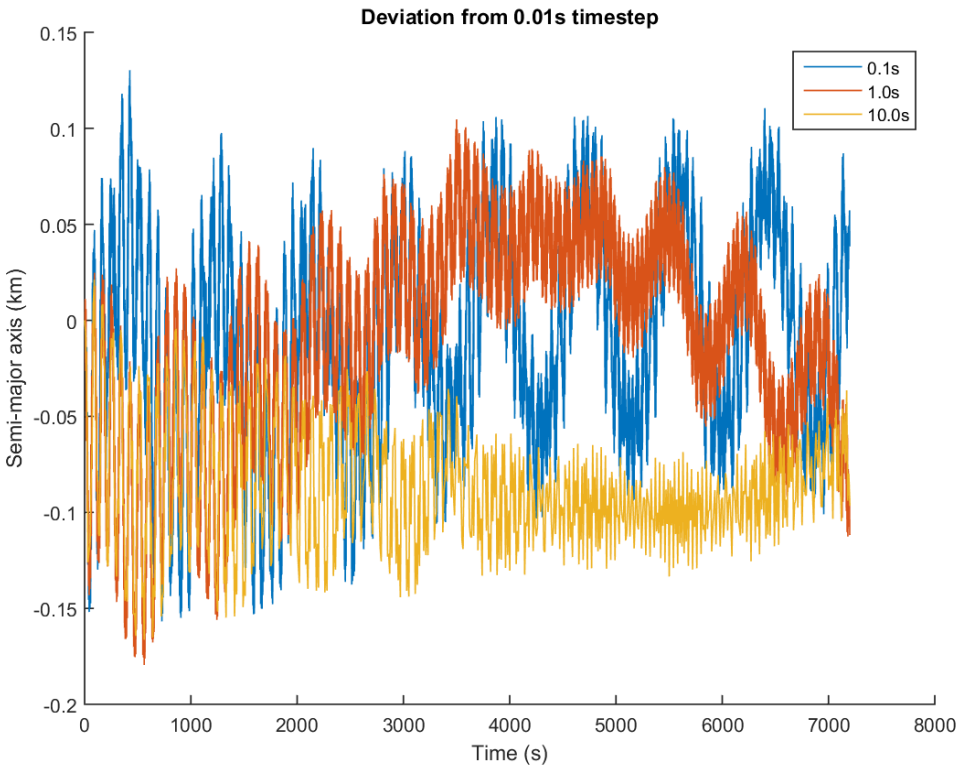

Figure 5.14: The effect of timestep on simulation accuracy and runtime

6 Results II

Chapter Outline

This section gives the results of the methods described in Chapter 4. These have been applied to specific test cases: Envisat and the MSG2 cooler cover. These are LEO and near-GEO objects respectively. The analysis and discussion of these results are given in subsequent chapters.

6.1 Envisat

Envisat is a now-defunct Earth observation satellite operated by ESA. Launched in March 2002, it operated for 10 years before communication with the satellite was lost. Weighing 8,211kg at launch and with the main bus measuring 2.5 x 2.5 x 10m, it is a large and heavy satellite and so poses a significant risk in space situational awareness. It is still in a polar low-Earth orbit, at roughly 773km altitude and with an inclination of 98°. Since communication was lost, there have been concerns that the satellite could contribute significantly to the debris population in the event of a collision.

Envisat was chosen as the first test object as we have high-fidelity models of the shape and material surface properties, which lend themselves to radiation pressure modeling. Furthermore, the centre of mass and moments of inertia are well-known. The observations after loss of communication indicate that the satellite is tumbling. Due to the large size of the satellite and its well-defined orbit, it is relatively easy to observe for additional data on the evolution of its tumbling. The panel orientation has been observed from the ground and from an imaging satellite.

Simulations of Envisat were run using the input parameters in Table 6.1 - the high fidelity of the model used is visualised in Figure 6.1, and the CoM is given in Table 6.2. This is a high-fidelity model in comparison to the box-and-wing approach shown in Figure 6.2, as the model used here is composed of geometric primitives. The end-of-life CoM was used for simulations. The moments of inertia used for attitude propagation are given in Table 6.3.

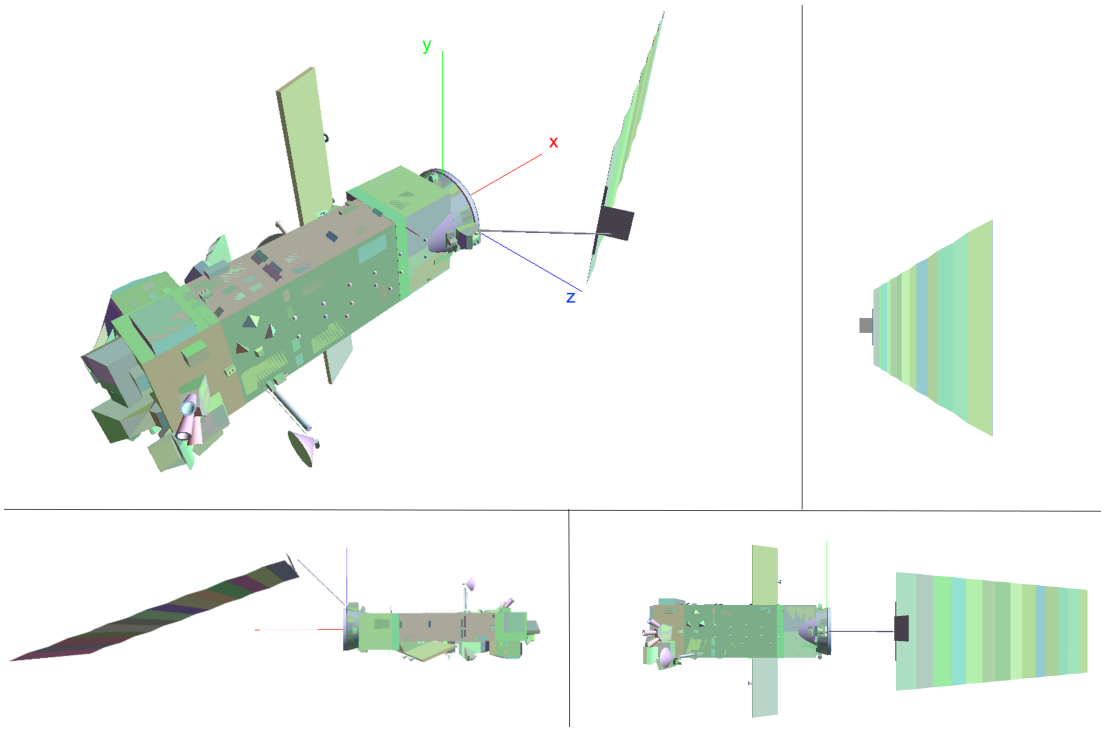

Figure 6.1: The "USER" file of Envisat visualised - clockwise from top left, perspective, view down x-, y- and z- axis respectively.

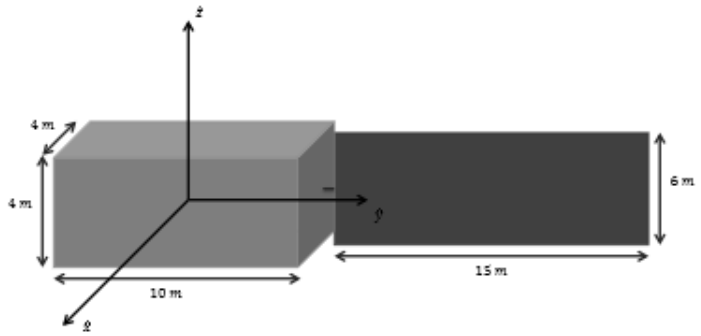

Figure 6.2: A typical Envisat model used by another research group - note that the boxes are larger than the bus and panel, in order to incorporate all antennae and transceivers into the simple box-and-wing geometry

Input parameter	Value
Pixel spacing	0.05m
Spiral points	5,000

Table 6.1: Input parameters for the Envisat radiation torque calculations

Date	Mass (kg)	Centre of Mass (m)		
		x	y	z
Initial (launch 1/3/2002)	8106.4	-4.635	-0.020	-0.039
Final (12/4/2012)	7827.9	-3.905	-0.009	0.003

Table 6.2: The Centre of Mass of Envisat [15]

6.1.1 Torque maps

The torque maps for Envisat are presented in Figures 6.3-6.5.

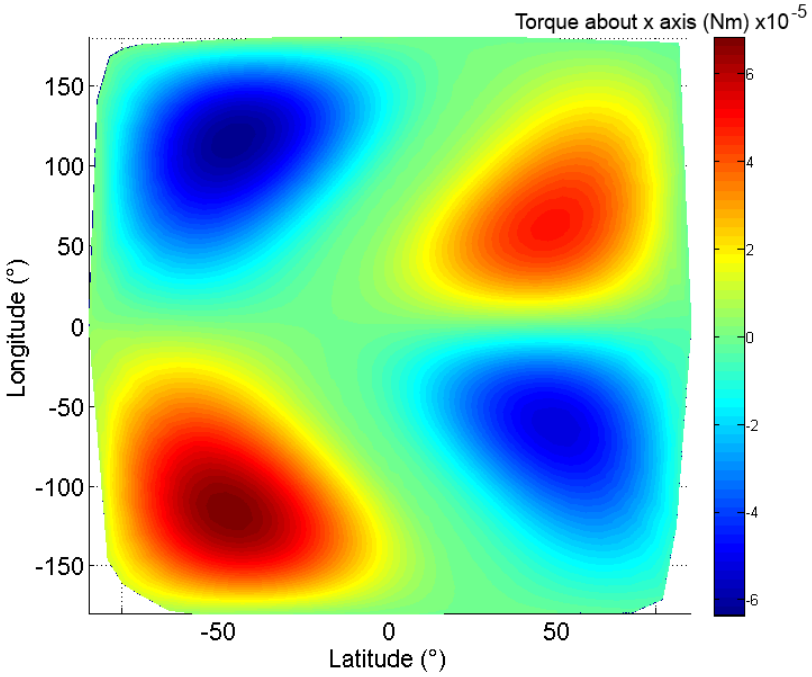

Figure 6.3: The torque on Envisat about the x-axis

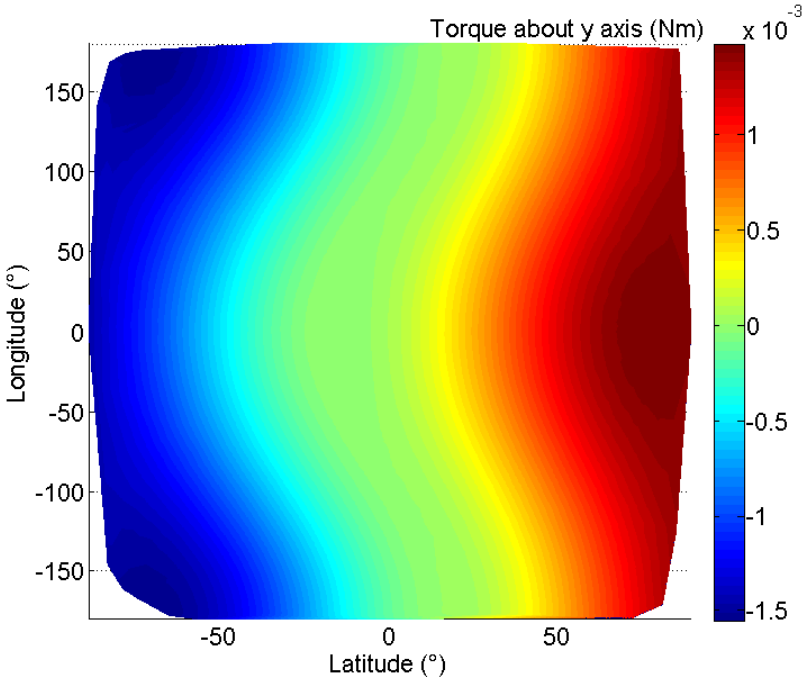

Figure 6.4: The torque on Envisat about the y-axis

Ix (kgm^2)	Iy (kgm^2)	Iz (kgm^2)
17023.3	124825.7	129112.2

Table 6.3: The Moments of Inertia of Envisat [15]

6.1.2 Attitude propagation

Using the torque maps, attitude propagation simulations were run for Envisat with zero initial angular velocity. The angular velocity increased about the y-axis, and the evolution over 2.5 orbits (4 hours) is given in Figure 6.6. The effect on tumbling rate is summarised in Table 6.4.

Based on the attitude propagation simulations of Envisat, we can see that there are both secular and periodic changes in the attitude about the y-axis, which is where the dynamics are most pronounced due to the largest torques. The periodic effects are due to the varying radiation torque as attitude changes. The torque is at a maximum when the solar panel is illuminated from either side, and the torque is smaller when radiation arrives down the $\pm x$-axis. The reason for the secular effect is down to the difference in optical properties of the front and the back of the panel, and due to the differences in shadowing. The active (front) side of the solar panel has properties $\mu = 0.85$ and $\nu = 0.25$, whereas the back has $\mu = 0.5$ and $\nu = 0.41$. As a crude approximation considering absorbed radiation only, this means that the front of the panel absorbs more light than the back; if both the front and the back have the same illumination conditions, the front experiences $\frac{(1-0.25)-(1-0.41)}{(1-0.41)} = 27\%$ more radiation force due to the difference in reflectivity ν. Another interpretation is that when the panel is illuminated from the front, the torque experienced is greater than when the panel is illuminated from the back.

Furthermore, due to the angle of the panel with respect to the satellite bus, there is a shadow cast on the back of the solar panel when the radiation arrives in the $-x$-direction. As a result, the radiation causes Envisat to tumble via a net "push" on the active side of the solar panel, which is not countered entirely by the reverse side of the panel. This is another reason for the secular change in attitude. The periodic effect is caused by the variation in torque with attitude; when the panel is not illuminated, due to the angle of incoming radiation, the torque is small

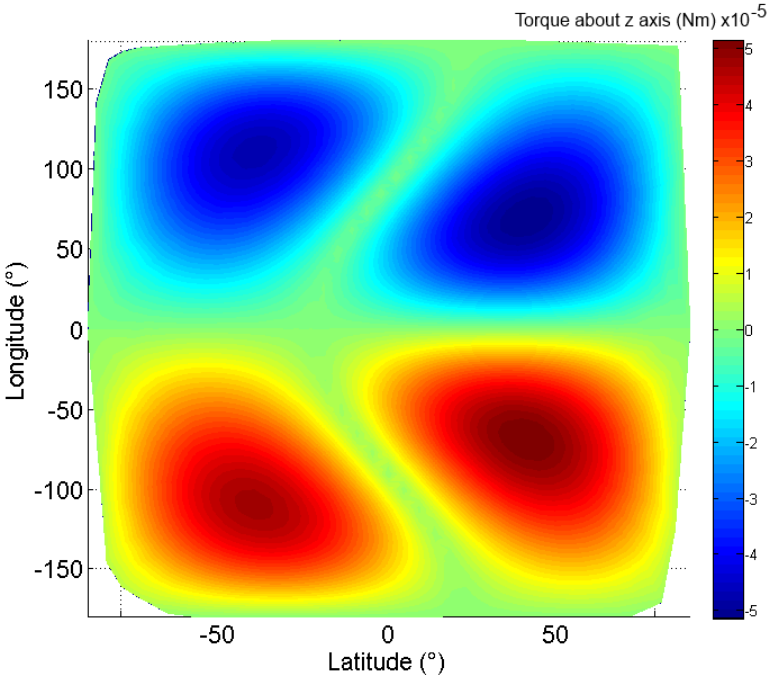

Figure 6.5: The torque on Envisat about the z-axis

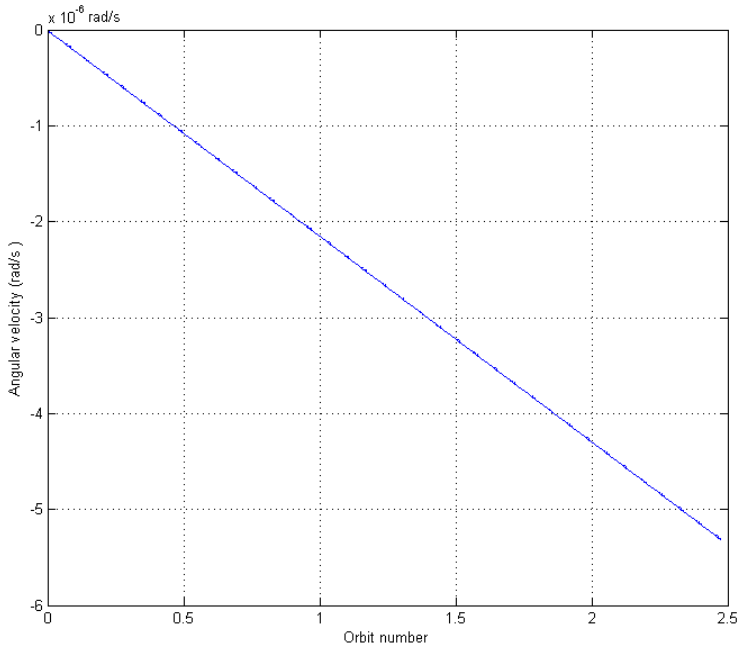

Figure 6.6: The attitude evolution of Envisat under radiation torques alone, over a two hour period.

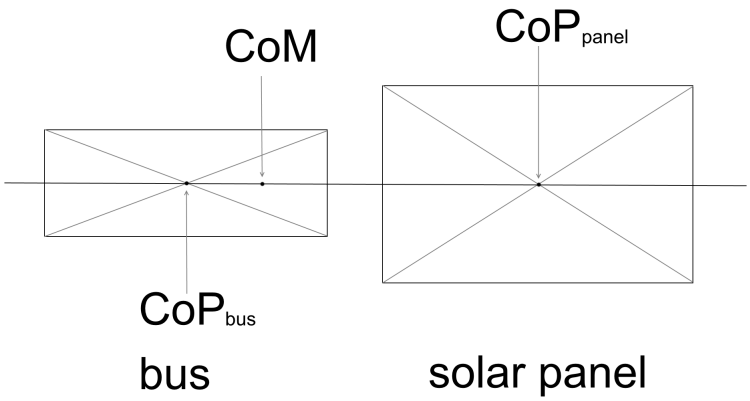

Figure 6.7: The CoM and CoP of Envisat used for verification of the torque computation

and thus changes in attitude are smaller.

6.1.3 Verification

It is important to verify the torque maps to first order, against manual calculations. The main radiation torque on Envisat arises from the solar panel which is separated from the main body by a boom, as shown in Figure 6.7. The distance from the centre of the solar panel (i.e. the CoP, the point where the panel radiation force acts) to the centre of mass is roughly $11m$. The area of the panel is $5 \times 14 = 70m^2$ [98]. The reflectivity of the front (active) side of the panel is 0.25 and specularity 0.85 and so the force exerted by radiation is (based on Equation 33 and using $\theta = 0$ for the maximum force):

$$F_{panel} = \frac{1364 \times 5 \times 14}{2.997 \times 10^8}(1 + 0.85 \times 0.25) + \left(\frac{2}{3}\right) 0.25\,(1 - 0.85) \tag{48}$$

$= \frac{118156.5}{2.997 \times 10^8}$

$= 3.944 \times 10^{-4} N$

The bus also experiences a radiation force - although the bus has many components and so the optical properties must be assumed based on a subset of these. The distance from the CoP of the bus to the CoM is roughly $-1.2m$. The area of the bus is $2.5 \times 10 = 25m^2$ [98]. Assuming reflectivity 0.5 and specularity 0.5, the force exerted by radiation is:

$$F_{bus} = \frac{1364 \times 2.5 \times 10}{2.997 \times 10^8}(1 + 0.5 \times 0.5) + \left(\frac{2}{3}\right) 0.5\,(1 - 0.5) \tag{49}$$

$= \frac{48308}{2.997 \times 10^8} = 1.612 \times 10^{-4}$

and thus the torque is:

$$\tau = \sum r \times F = \left(11 \times 3.944 \times 10^{-4} - 1.2 \times 1.612 \times 10^{-4} Nm\right) \tag{50}$$

$= 4.34 \times 10^{-3} - 1.93 \times 10^{-4} Nm = 4.15 \times 10^{-3} Nm$

The pixel array method gives a maximum torque about the y-axis of $1.5 \times 10^{-3} Nm$, thus the maximum torque calculated by the software is in line with a crude first-order calculation. The pattern of torques and their dependency on latitude and longitude in the torque map are as expected; as the radiation source moves out of plane of the solar panel, the torque is reduced, and when the radiation arrives from the back of the panel the torque is negative. Also, there is an offset in the torque map which corresponds to the angle between the solar panel and the xy-plane.

Further to this, the gravity gradient torque can be calculated, based on Equation 16. The moments of inertia are given in Table 6.3. For the maximum torque, which is also about the y-axis based on the moments of inertia:

$$\tau_y = \frac{3GM}{2R^3}(I_z - I_x) = 1.635 \times 10^{-6} \times (129112.2 - 17023.3) = 0.1833 Nm \tag{51}$$

Which gives an angular acceleration of:

$$\ddot{\omega_y} = \frac{\tau_y}{I_y} = \frac{0.1833}{124825.7} = 1.47 \times 10^{-6} rad\ s^{-2} \tag{52}$$

This is in line with what is expected based on the results of the computational analysis. Also, the relative magnitudes of gravitational and radiation torques are important - gravitational torques dominate but their effect is perturbed by radiation torques, both of which have different periodicities due to their differing sources. The combination of radiation and gravitational torques together did not explain the

x (rad/s^2)	y (rad/s^2)	z (rad/s^2)
2.21×10^{-8}	7.55×10^{-7}	2.43×10^{-8}

Table 6.4: The maximum angular accelerations induced by radiation torques about each axis

observed tumbling behaviour of Envisat, and thus there must be another influence on the attitude causing the observed tumbling.

6.2 MSG2 cooler cover

Simulations were run for the MSG2 cooler cover, with initial conditions as given in Table 3.1, in a variety of tumbling states: no tumbling (with an attitude fixed towards the Sun so that radiation forces are maximised), tumbling slowly (0.1deg/s = 1 revolution per hour), tumbling quickly (5deg/s) and no tumbling (with an attitude fixed to minimise radiation forces). The results of these simulations are split into two separate sections: the first gives net changes, and the second gives relative changes.

6.2.1 Net changes in orbital elements

The initial conditions for the cooler cover are given in Table 3.1. The results are given as separate plots for the net changes and the relative effects of the four spin rates. The net changes give the overall evolution of the objects, whereas the relative changes take the simulations with an attitude fixed for minimum effect of the radiation force as a baseline. The other results have this baseline subtracted, in order to reveal dynamics that are caused by tumbling and non-conservative forces.

In the following subsections, the simulations will be abbreviated as follows:

- Attitude fixed for minimum non-conservative effect: minimum
- Attitude fixed for maximum non-conservative effect: maximum
- Fast tumbling: fast
- Slow tumbling: slow

Figure 6.8 shows the change in semi-major axis over a week, which is a short-term periodic variation and is broadly similar for all four test cases.

Figure 6.9 shows the change in semi-major axis over a month, which is a short-

term periodic variation within the envelope of a longer-term periodic variation.

Figure 6.10 shows the change in semi-major axis over a year. There are short-term and long-term periodic changes, but no secular change over the course of a year. The semi-major axis remains broadly consistent over the course of a year.

Figure 6.11 shows the change in eccentricity over a week. The cooler cover simulated with a fixed attitude to minimise the non-conservative effects does not have a secular change in eccentricity over the week; there is a short-term periodic trend although the amplitude of this trend increases over the course of the week. The slow and fast tumbling simulations exhibit very similar changes in eccentricity, with dynamics that are the same as the maximum simulation but are damped in magnitude.

Figure 6.12 shows the change in eccentricity over a month. All four simulations show short-term and long-term periodic effects which are very similar, but the difference is in the secular changes. The minimum simulation has the smallest secular change, closely followed by both the fast and slow simulation. The maximum simulation has the largest change in eccentricity over the course of a month, of approximately 3×10^{-4}.

Figure 6.13 shows the change in eccentricity over a year. The long-term periodic trends are still visible. The secular changes are apparent - the minimum simulation shows very little change in eccentricity over a year. The two tumbling simulations show a change of 1×10^{-3} in eccentricity, and the maximum simulation shows a change of 12×10^{-3} over the year. The two regions where the change in eccentricity slows down correspond to eclipse seasons.

Figure 6.14 shows the change in inclination over a week. All four simulations show similar increases in inclination over this time period, along with a small short-term periodic variation. Figure 6.15 shows the change in inclination over a year. All four simulations short-term periodic variations, with similar behaviour for both fixed maximum n/c force and slow rotation. The fast rotation results show the greatest variation.

Figure 6.16 shows the change in AP over a week. All four simulations show similar increase in AP over this time period, along with a small short-term peri-

odic variation. Figure 6.17 shows the change in AP over a month. Again all four simulations show similar evolution, which is a short-term periodic variation superimposed on a long-term decrease in AP. Figure 6.18 shows the change in AP over a year. All four simulations show similar variations - short-term periodic variations, long-term periodic variations and what appears to be an overall decrease in AP over the course of a year.

Figures 6.8-6.18 give the net changes in orbital elements over the timescales of a year, a month and a week, to show the secular effects over a year and at the same time give detail on the long-term and short-term periodic effects. Note that the lines for the slow and fast tumbling are identical on the scale of these graphs, and so the fast rotation results are hidden behind the slow rotation results.

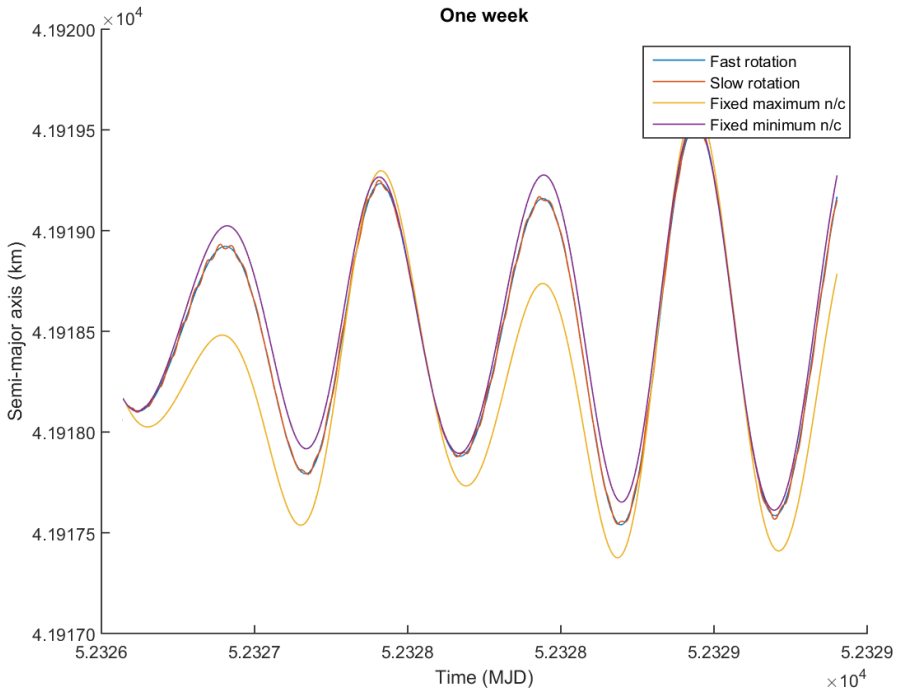

Figure 6.8: The variation in semi-major axis of MSG2 over a week

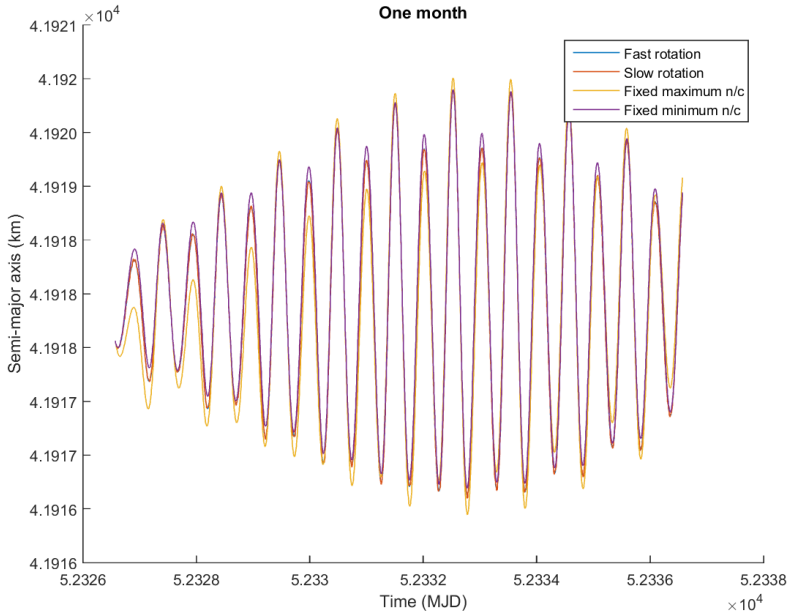

Figure 6.9: The variation in semi-major axis of MSG2 over a month

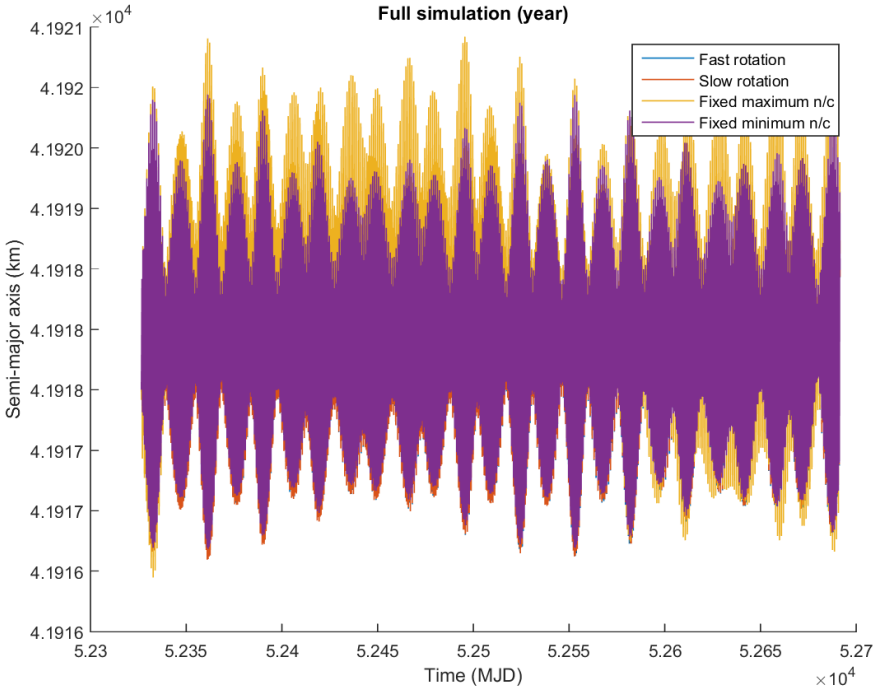

Figure 6.10: The variation in semi-major axis of MSG2 over a year

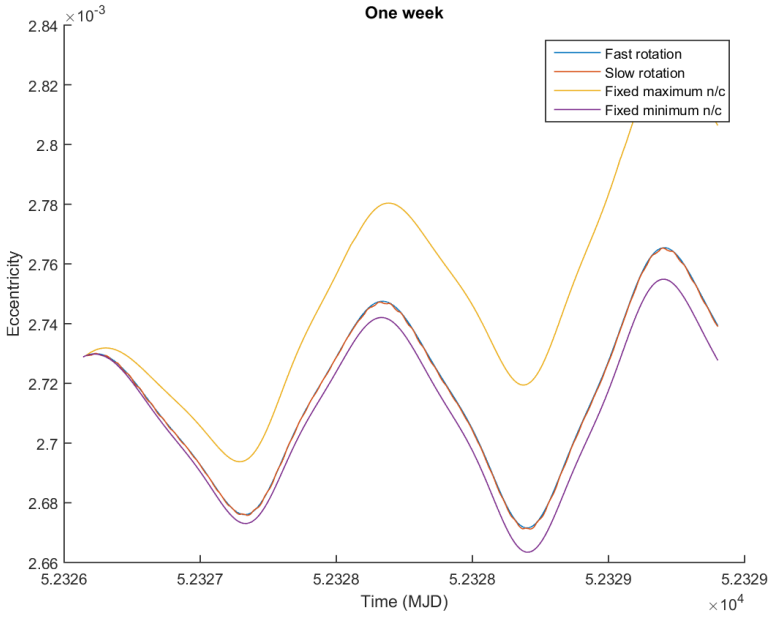

Figure 6.11: The variation in eccentricity of MSG2 over a week

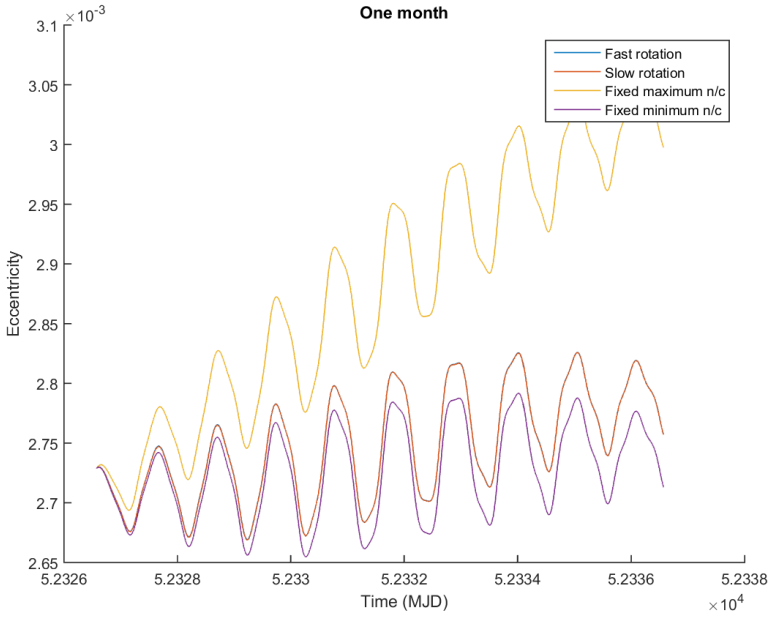

Figure 6.12: The variation in eccentricity of MSG2 over a month

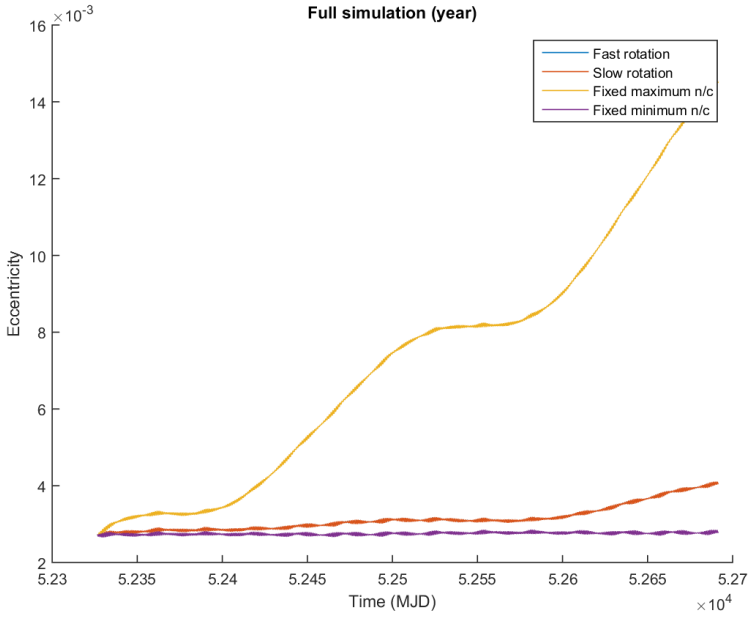

Figure 6.13: The variation in eccentricity of MSG2 over a year

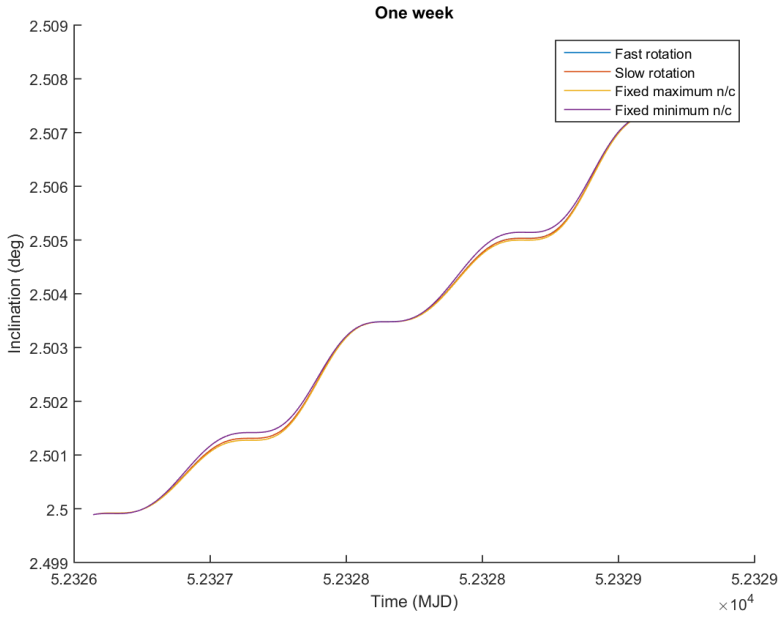

Figure 6.14: The variation of inclination of MSG2 over a week

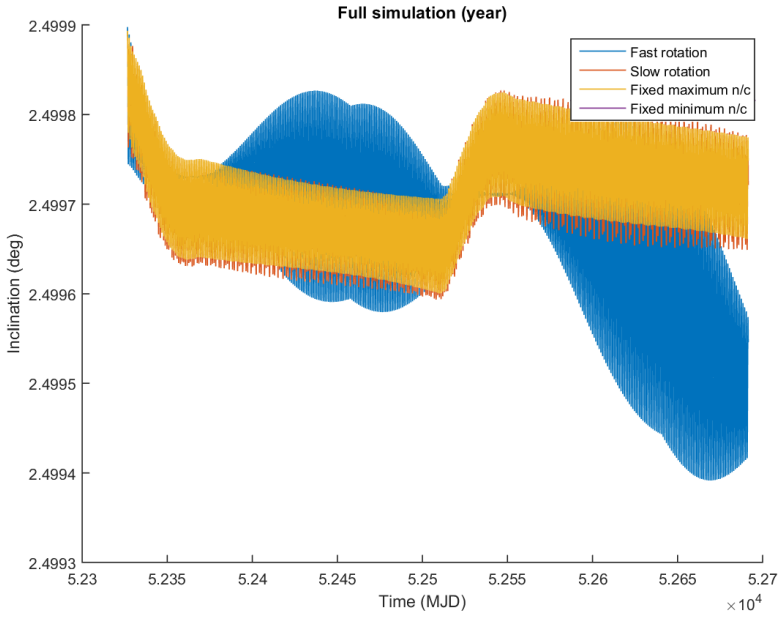

Figure 6.15: The variation of inclination of MSG2 over a year

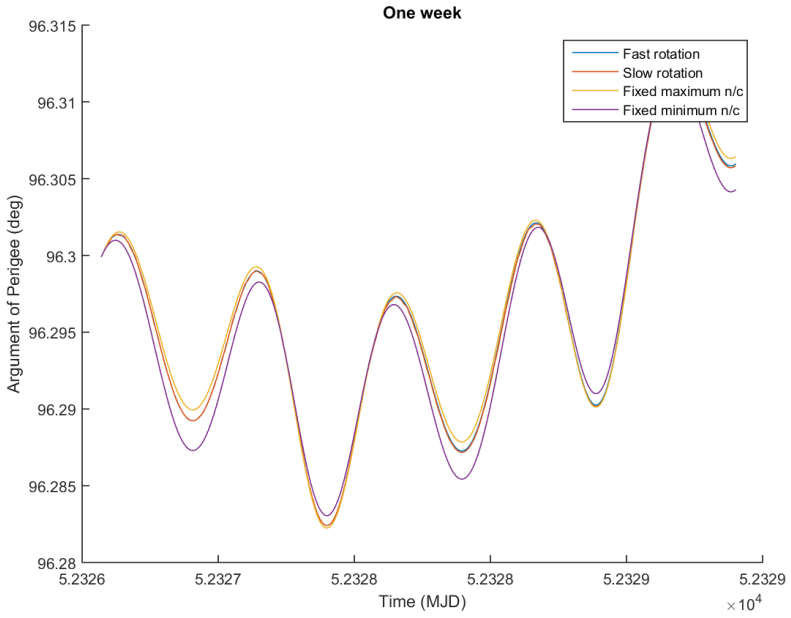

Figure 6.16: The variation in argument of perigee of MSG2 over a week

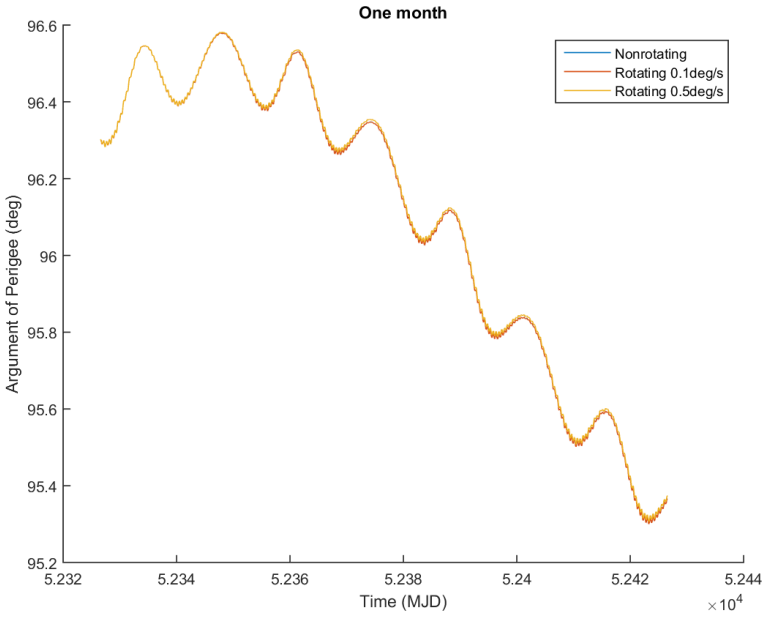

Figure 6.17: The variation in argument of perigee of MSG2 over a month

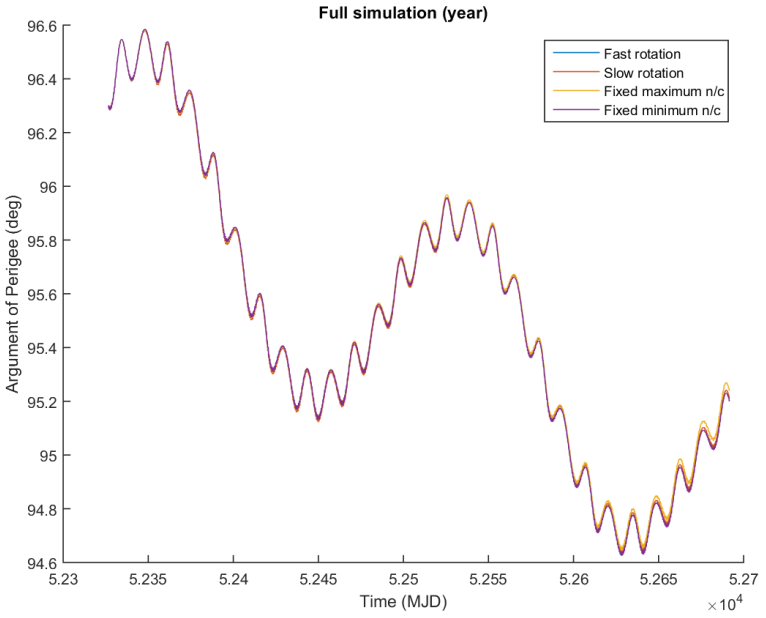

Figure 6.18: The variation in argument of perigee of MSG2 over a year

6.2.2 Relative changes in orbital elements

Based on the results of the previous section, the differences were taken. The simulation with no tumbling, and with attitude fixed to minimise non-conservative forces, was taken as the benchmark and subtracted from the results of the other simulations. Figures 6.19 - 6.23 give the relative changes in orbital elements.

Figure 6.19 shows the relative change in semi-major axis over a month. Taking the minimum simulation as a baseline, the maximum simulation shows a short-term periodic effect along with a secular increase in semi-major axis. The tumbling simulations show similar dynamics - a short-term periodic variation and a smaller average semi-major axis than the minimum simulation.

Figure 6.20 shows the relative change in semi-major axis over a year. It is apparent that for a simulation ignoring non-conservative forces, the semi-major axis does not change over a year (purple line). The effect of fast rotation (blue line) and slow rotation (red line) are very similar. They exhibit a smaller semi-major axis, with periodic variations which correspond to individual orbits around the Earth. The object with a fixed attitude and maximum non-conservative force shows an increase in semi-major axis compared to the object with minimum non-conservative forces, but also shows seasonal changes in its semi-major axis. The two 'pinched' points in the plot correspond to eclipse seasons.

Figure 6.21 shows the relative change in eccentricity over a year. Compared to the baseline minimum simulation, the maximum simulation shows an increase in eccentricity of 1×10^{-4}, although the increase slows during eclipse season. The tumbling simulations show the same dynamics but the magnitude is damped; the overall increase is 1×10^{-3} over a year.

Figure 6.22 shows the relative change in inclination over a year. Compared to the baseline, the tumbling and maximum simulation show a seasonal decrease in inclination. The tumbling objects have a small decrease in inclination of 0.5×10^{-4} deg after each eclipse season, whereas the maximum simulation shows a similar decrease after the first eclipse season, but a larger decrease of 4×10^{-4} deg after the second.

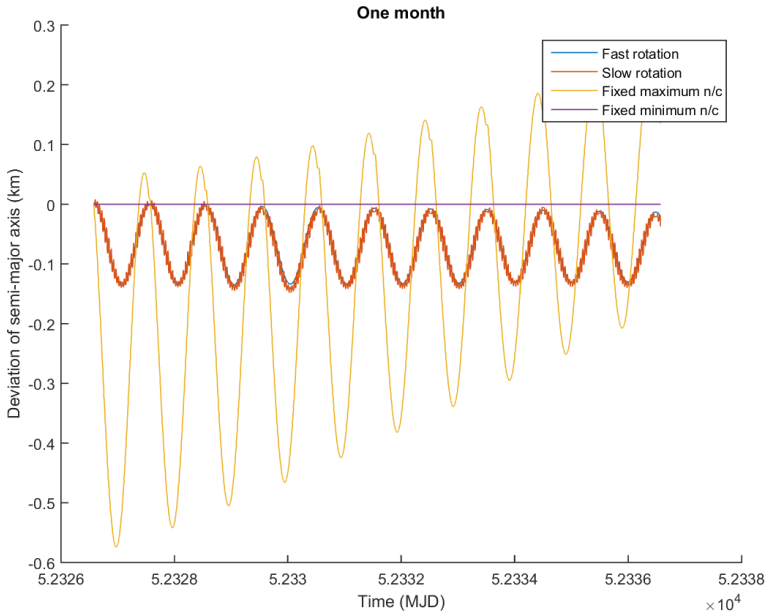

Figure 6.19: The relative variation in semi-major axis of MSG2 over a month

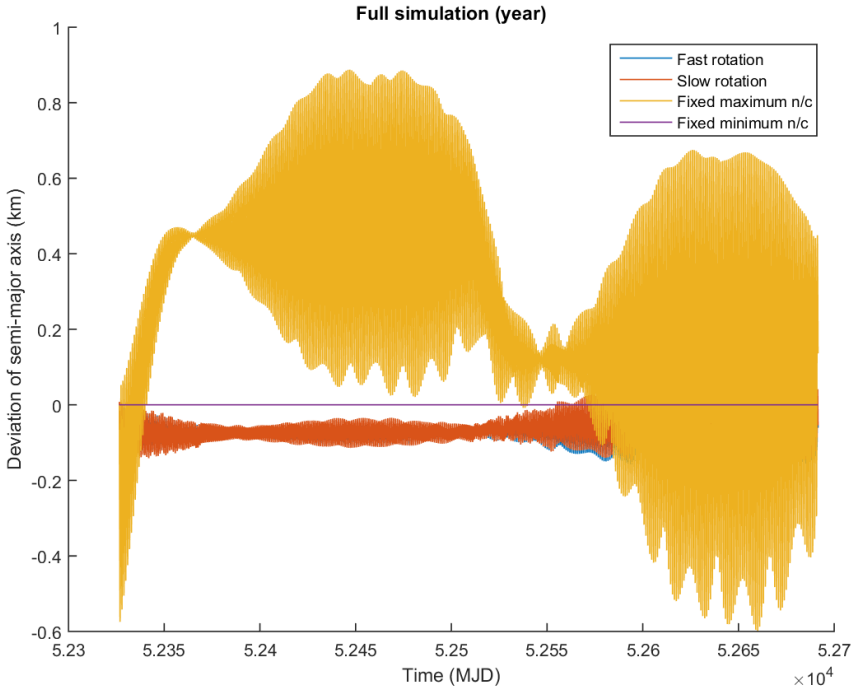

Figure 6.20: The relative variation in semi-major axis of MSG2 over a year

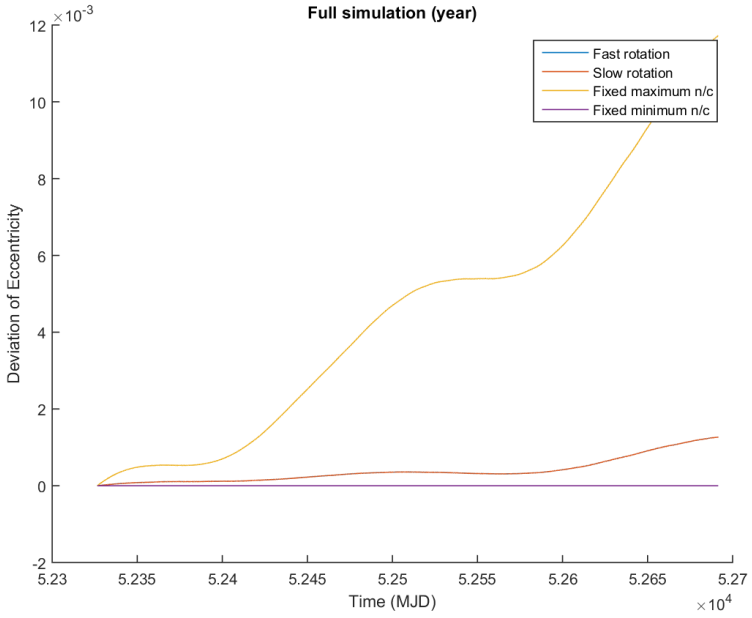

Figure 6.21: The relative variation of eccentricity of MSG2 over a year

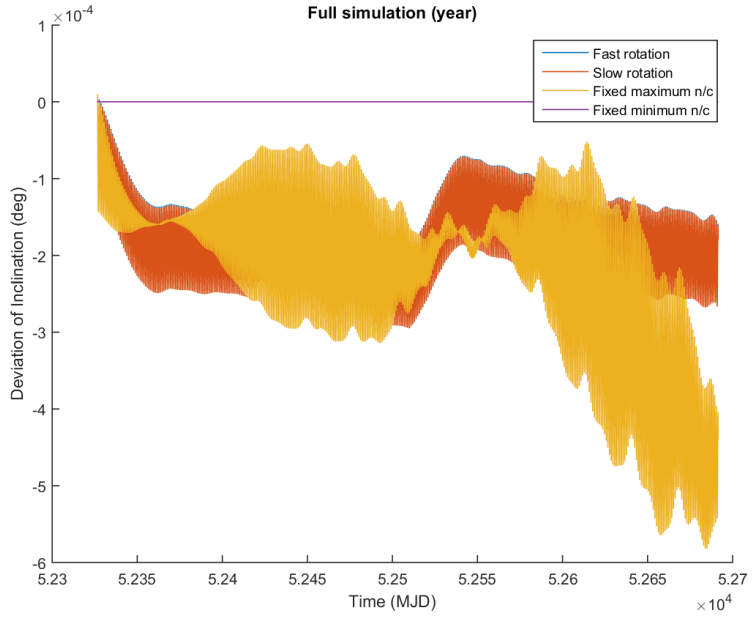

Figure 6.22: The relative variation of inclination of MSG2 over a year

Figure 6.23 shows the relative change in AP over a year. All three simulations show an initial decrease in AP over the first month, followed by a slow increase after the first eclipse season. During the second eclipse season, the maximum simulation shows no change in AP whereas the tumbling objects show a quicker increase than outside the eclipse season. After this, all three show an increase in AP similar to that before the eclipse season.

To summarise, the effects of non-conservative forces are dampened by tumbling motion. The rate of tumbling does not change this effect - the fast and slow tumbling simulations have similar results.

The periodic effects of non-conservative forces and the effect of tumbling are:

- Non-conservative forces cause an increase in eccentricity, decrease in AP and no overall change in semi-major axis over the course of a year on the MSG2 cooler cover under J2 gravity and radiation forces alone.
- Tumbling causes a dampening of these effects - the simulation results are between those of an object fixed to experience the maximum radiation force, and those of an object fixed to experience the minimum radiation force.

Chapter Summary

The results of radiation torque calculations, attitude propagation under radiation torques alone, and simulations of tumbling have been presented. These form the basis of analysis and discussion in subsequent chapters.

7 Additional Study

Chapter Outline

This chapter presents results which are complementary to the aims of the thesis.

7.1 Envisat photometric observations

Envisat has been described in Section 3.2.4 and its attitude motion under radiation torques is given in Section 6.1. Communications with the satellite were lost in 2012, and it is a good object for observation as it is one of the largest and most massive SROs that is uncontrolled.

The satellite is known to be tumbling, and data on this is available from many sources. Initial observations showed the tumbling period to be $0.2\,\mathrm{deg}/s$ in 2012 [99], increasing to $2.7\,\mathrm{deg}/s$ in 2013 [100].

The NERC Space Geodesy Facility in Herstmonceux uses both satellite laser ranging and photometry equipment. They have recorded photometric data for Envisat with observation of passes in 2013 and 2014. Further measurements are currently being recorded.

These results have been processed. An example of a good observation session without cloud cover is given in Figure 7.1, and pass with partial cloud cover is given in Figure 7.2. A total of 38 passes were recorded, with 16 giving usable data.

The data was analysed by counting the number of peaks visible over a given observation session. These peaks represent "glints" - that is, a sudden bright flash which represents the reflection of solar light from a surface of the spacecraft. These might be flashes of the front and back of the solar panel, or flashes from each side of the spacecraft bus.

The data was processed in order to find the peak-to-peak tumbling rate. This could represent a 90°, 180° or 360° rotation of the satellite peak-to-peak, but based on other experimental studies of Envisat tumbling the most reasonable assumption is 90°. This gives a tumbling period based on photometric observations of $4 \times 31.2 = 124.8s$ in July 2013, compared to 134.74s observed in September 2013 using SLR range residuals [100]. The time-evolution of this spin period is given in Table 7.1

Date	Tumbling Period (s)
01/04/2012	0
12/04/2013	30.9
05/06/2013	30.3
10/06/2013	31.4
10/06/2013	30.6
05/07/2013	30.4
07/07/2013	30.8
08/07/2013	29.5
10/07/2013	30.4
11/07/2013	31.2
13/07/2013	31.0
18/07/2013	30.4
19/07/2013	30.0
21/07/2013	27.0
12/08/2013	30.8
20/08/2013	27.5
09/09/2013	33.3

Table 7.1: Envisat photometry data showing the evolution of tumbling period

which is visualised in Figure 7.3. The satellite communications were lost on 8th April 2013 and up to this date the satellite was in a stable attitude configuration.

These results need combination with data from other sources in order to give a detailed picture of how the tumbling rate of Envisat has evolved over time. By combining such information with the simulation results outlined in this thesis, the complete story of what has happened to Envisat could be ascertained. For example, the tumbling might be solely as expected from the natural influence of the space environment, or it might be that the tumbling has been caused by a failure in an attitude control mechanism onboard the satellite.

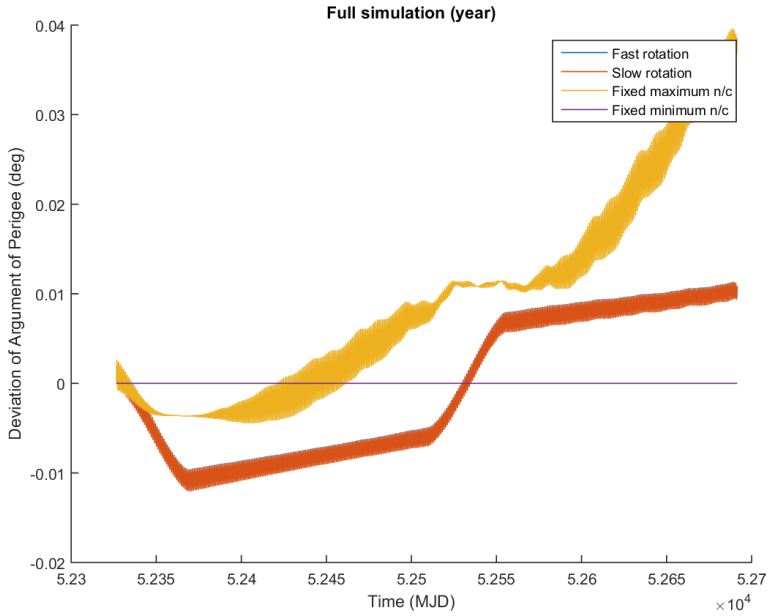

Figure 6.23: The relative variation in argument of perigee of MSG2 over a year

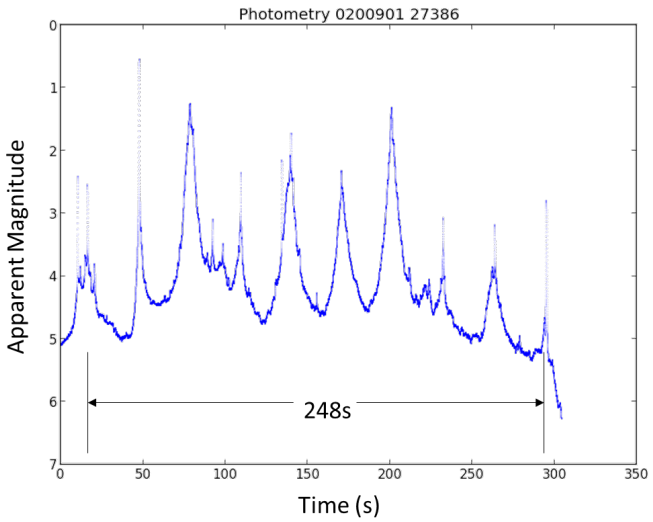

Observation date 20/08/13, clear skies
248s duration, 10 peaks. Features imply tumbling
27.5s tumbling (peak-to-peak so could be 90°, 180° or 360°)

Figure 7.1: A plot of apparent magnitude evolution for Envisat on 20/08/13 with clear skies

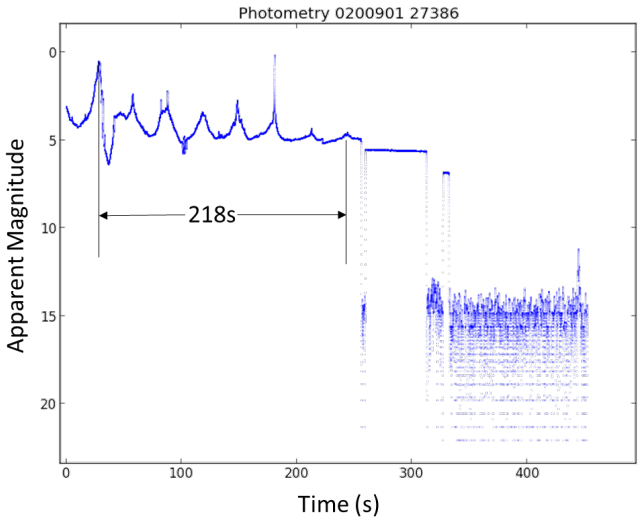

Observation date 11/07/13, clear skies
218s duration, 8 peaks
31.2s tumbling (peak-to-peak)

Figure 7.2: A plot of apparent magnitude evolution for Envisat on 11/7/13 with partial cloud cover

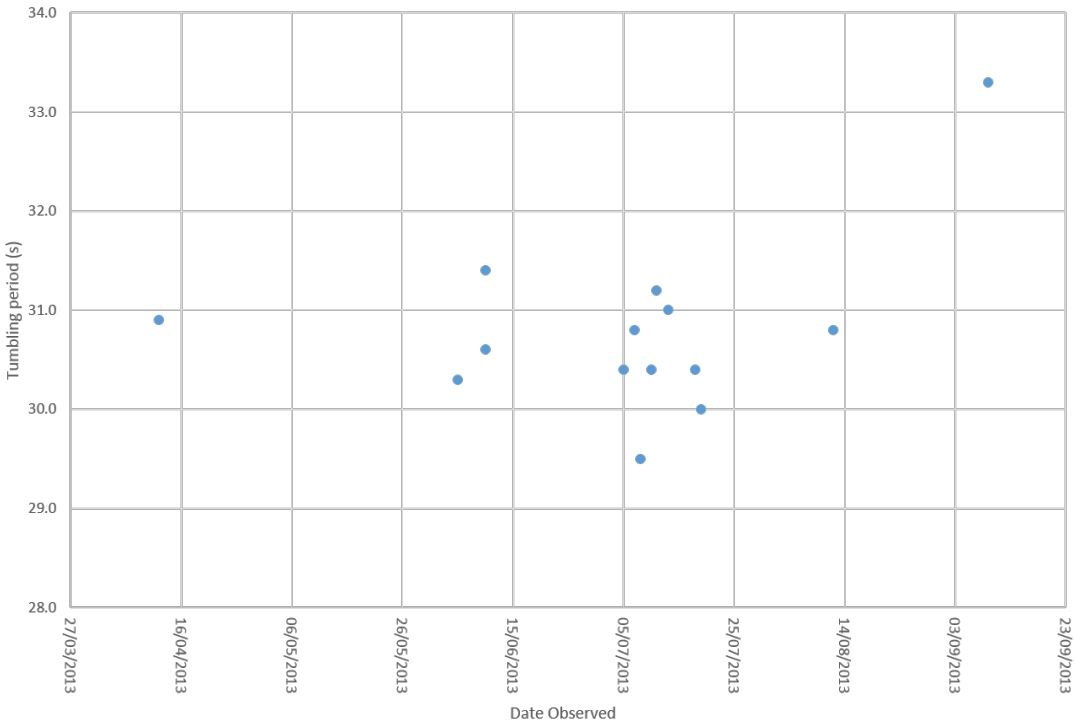

Figure 7.3: The evolution of tumbling as given by Envisat photometry data

7.2 Nanosatellites as a test platform

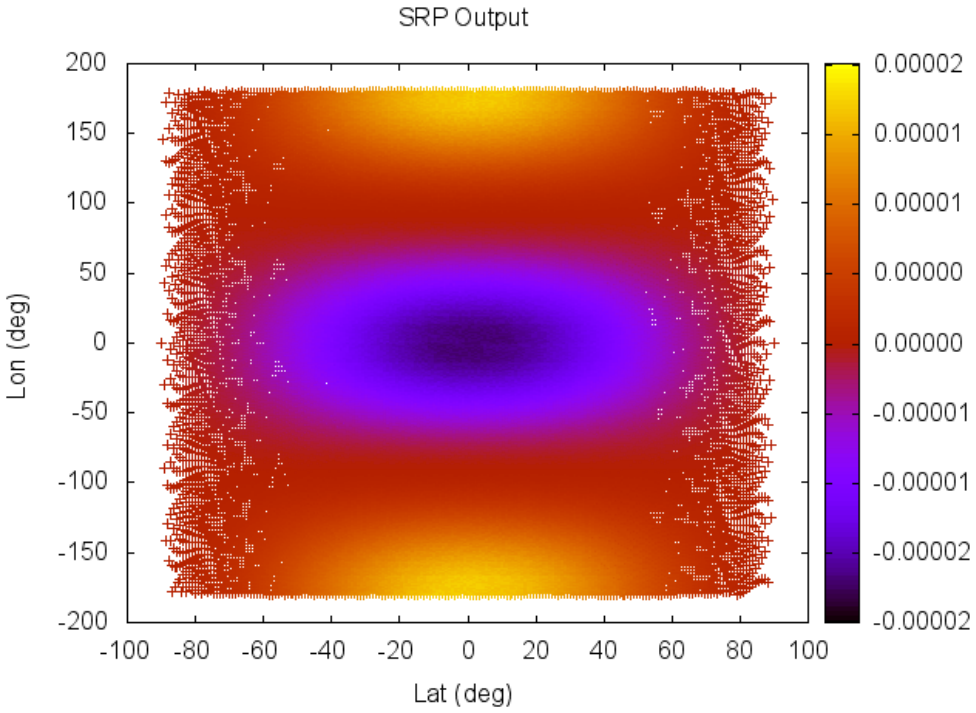

Figure 7.4: Torque map for the Kicksat sprite satellite about the x-axis

An inherent problem with orbital modelling of the debris constellation is that real-world data is extremely difficult to obtain. A key shortcoming of previous studies is that the results and validation have been purely through observation of pre-existing space-resident objects (SROs). This gives problems in validation as the physical characteristics of these objects are rarely known. However, recent developments in access to space for educational institutions will hopefully lead to experimental data which will be much more useful in the validation of computational models. CubeSat [6] initiatives such as the NASA Educational Launch of Nanosatellites (ELaNa) project are enabling universities to access space for research. Through involvement in these projects, data may be obtained which would enable validation and improvement of models.

A potential platform for such experiments is the KickSat project at Cornell University. The idea behind the KickSat project is to integrate many single-PCB

[6]The CubeSat platform is 10x10x10cm and weighing no more than 1.33kg, and is currently the leading small satellite platform

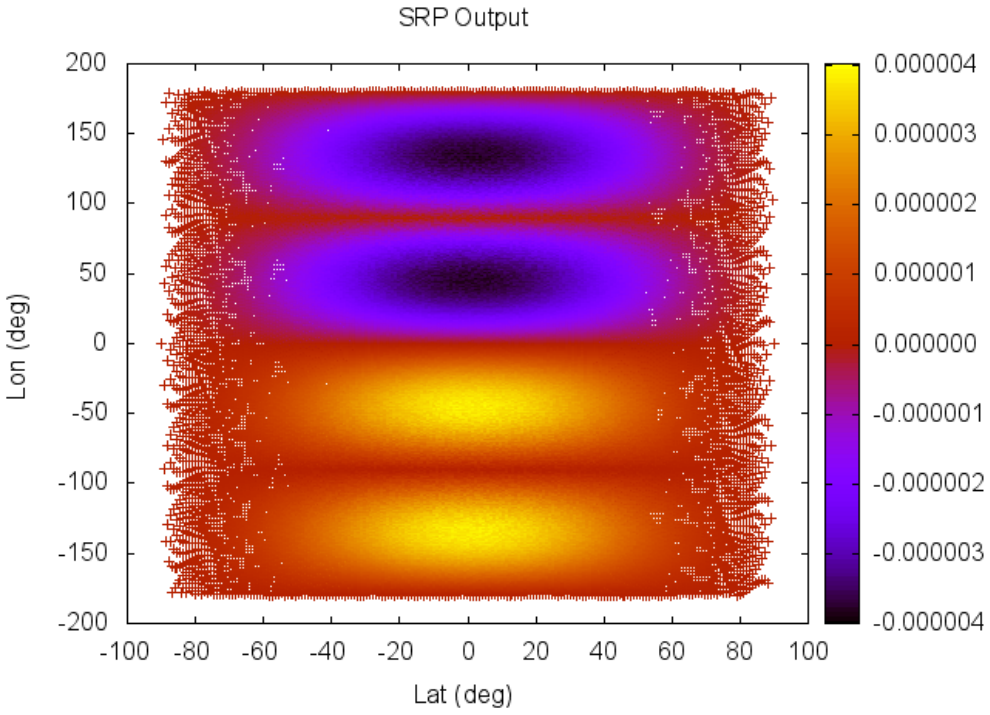

Figure 7.5: Torque map for the Kicksat sprite satellite about the y-axis

satellites ("sprites") into a CubeSat, which will enable the deployment of the sprite satellites in low earth orbit. A drawing of the 3U [7] CubeSat is given in Figure 7.7, along with a diagram of a single sprite satellite in 7.8. The specifications of each KickSat sprite satellite are given in Table 7.2.

The bulk of the funding for the KickSat project came through "crowdsourcing" on the KickStarter website, hence its name; that is, enthusiast organisations and members of the public each contributed to sponsor individual sprites. The mission was launched on April 18th, 2014; however, there was a malfunction in the release mechanism and so the sprite satellites never left the CubeSat. The entire CubeSat containing all 200 sprite satellites then re-entered the atmosphere on May 15th 2014.

The purchase of the three sprites for launch did not go through due to administrative issues, however, it was agreed that data from unpainted sprites would be provided. This data was not acquired as the CubeSat doors did not open correctly and the entire 3U container burnt up on re-entry.

[7] 3U indicates 3-unit, i.e. 30x10x10cm

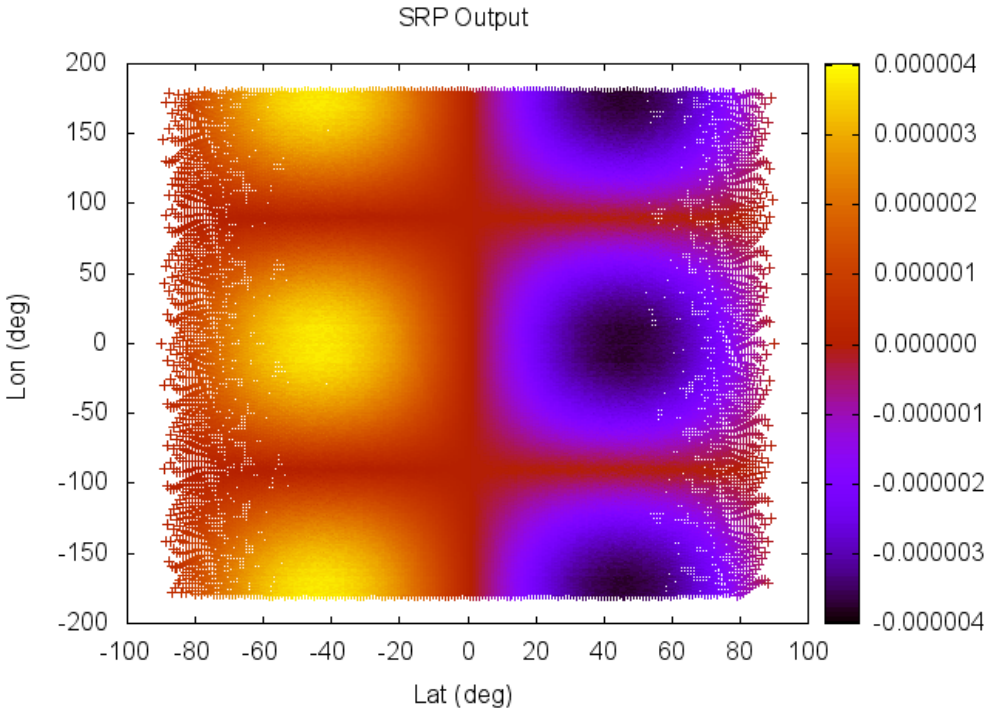

Figure 7.6: Torque map for the Kicksat sprite satellite about the z-axis

An important development for the analysis of space debris is the idea of a single-PCB satellite. These satellites are small and have HAMR properties, both of which are characteristics of a large subset of the space debris constellation. As the sprites have a high area-to-mass ratio, their orbital tumbling should resemble that of space debris - they are "debris-like" objects. The onboard sensors will enable the determination of attitude and tumbling of debris-like objects. This will be a leap in applying the scientific method to the problem of situational awareness. The data from such objects would be useful in validating and improving any theoretical models of the debris population. An additional use of the data is in finding the orbital lifetime of HAMR objects in LEO.

These small and lightweight satellites could be attached to objects which are known to become uncontrolled debris, such as rocket bodies and instrument covers. Onboard accelerometers and gyroscopes can transmit useful information about an object's position, orbit and its tumbling profile, all of which are difficult to obtain through observation alone.

Due to their low cost, single-PCB satellites can be customised for experiments.

One such customisation would be the painting of each half of a satellite so as to exert a radiation torque. The difference in optical properties between matte black (highly absorptive) and reflective white (highly reflective) would lead to a large radiation torque. Such an object is visualised in Figure 5.12. The difference between the paint on the front and back of the PCB is also important - if both sides match then oscillatory effects would be expected, whereas if both sides were painted opposite a secular and continuous radiation torque would be applied and so the object would continue to spin up until other attitude effects come into play. The computed torque maps are given in Figures 7.4-7.6.

In terms of technical specifications, MEMS sensors offer high resolution detection of forces using accelerometers and high resolution data on tumbling via gyroscopes. An example for application to small satellites is the Analog Devices ADIS16250, which is a small and low-power package that provides a pointing accuracy of 1° over a 2-minute period [101].

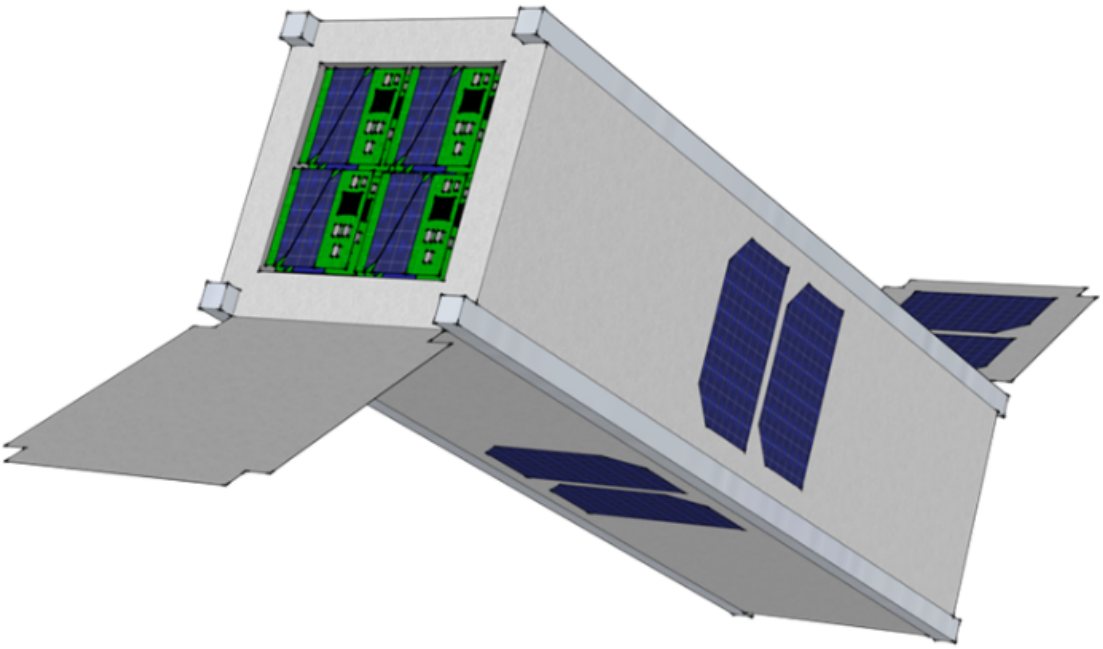

Figure 7.7: A drawing of the 3U cubesat housing 200 Kicksat sprite satellites, courtesy [10]

There is a lot of future potential for small satellite projects such as KickSat, particularly in the domain of SSA and space debris.

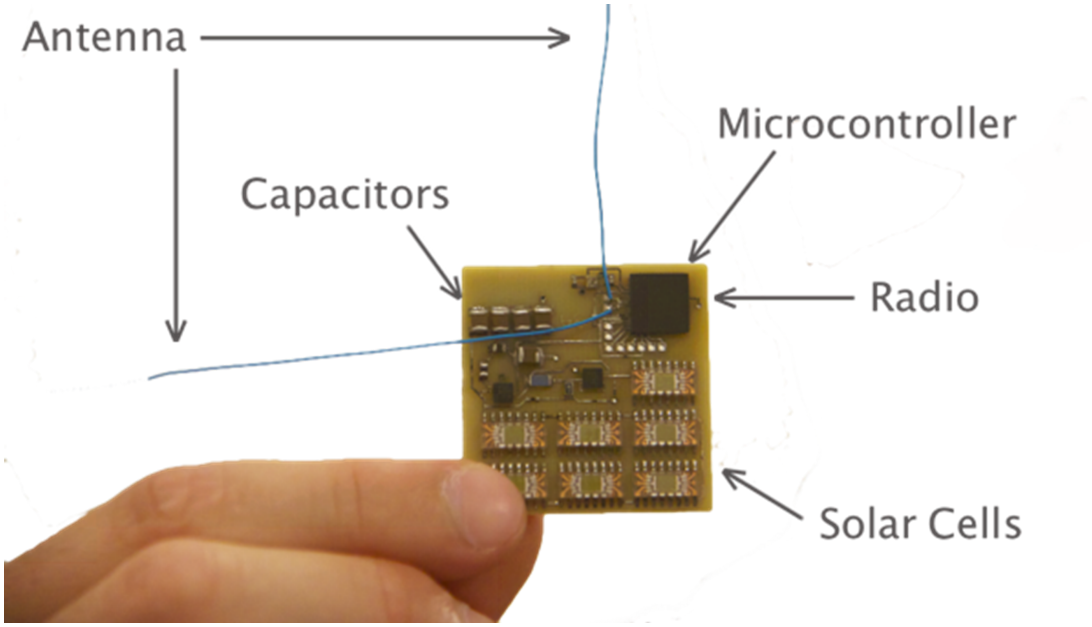

Figure 7.8: The layout of a single sprite nanosatellite, courtesy [10]

7.3 Electromagnetic interactions: the Lorentz force

The movement of a charged object in a magnetic field leads to the Lorentz force. If an SRO carries a net electrostatic charge, then the motion of the SRO will be influenced through the interaction of this charge with the local magnetic field of the Earth. The Lorentz force for a charge particle moving in an electromagnetic field is given by:

$$\vec{F}_L = q\left(\vec{E} + \vec{v} \times \vec{B}\right) \tag{53}$$

where $\vec{F}_L$ is the Lorentz force, q is the total surface charge, $\vec{v}$ is the velocity of the particle, $\vec{E}$ is the electric field vector and $\vec{B}$ is the magnetic field vector. SROs can become charged through electron, ion and photon flux interactions in the near-Earth space environment.

The Lorentz force has been suggested as a means to de-orbit space debris by attaching conductive tethers [102]. The difference between that study and the analysis presented below is that the research paper assumes active charging, whereas the analysis presented below is for purely passive objects.

To study the Lorentz force, the International Geomagnetic Reference Field

Parameter	Value
Dimensions	32mm x 32mm x 1.5mm PCB 2 x 17cm smart metal wire antenna
Mass	8g
Orbit	LEO (300km, 30° inclination)
Orbital lifetime	20.5 days predicted, 1.3-47 days
Power system	Peak: 0.132W (60mA @ 2.2V)
Sensors	Magnetometer / gyro / accelerometer
Communication	437MHz radio link, 0.01W transmitter

Table 7.2: The specifications of each KickSat sprite satellite

(IGRF) [103] has been implemented as a model of the near-Earth magnetic field. Whilst new missions are in progress to advance understanding of the behaviour of the Earth's magnetic field, the IGRF is the current scientific standard model, and is the most widely used and tested magnetic field model backed up by a large scientific community. The IGRF gives the magnetic field vector at a given point and its secular variation.

For the purposes of orbit determination and prediction, the Lorentz force has been substantially ignored. Previous studies are limited to the dynamics of small, micron-sized debris [104]. An engineering study considers a point charge and looks only at the effect as a control mechanism, whilst using only a crude magnetic field model [51]. More recent studies are limited to spacecraft which maintain their surface charge actively. The charging of larger SROs such as debris and entire spacecraft has been largely ignored [105, 106], even though the natural space environment is known to induce electrostatic potentials. In-orbit measurements have observed charging on the level of tens of kilovolts [107], and both the spacecraft charging community and satellite manufacturers work on methods to mitigate surface charging due to the damaging effects it can have on spacecraft electronics.

In this study, a high-fidelity charge distribution model has been considered. This has two benefits. Firstly, the accuracy of force modelling is improved through understanding the charging mechanisms, which in turn leads to a better estimation

of the total surface charge. Secondly, the extended distribution of charge enables the future calculation of torques. The aim of this work is to determine how the Lorentz force influences the trajectory of objects with a fixed charge.

Precise orbit prediction and determination are important in the domain of satellite operations, as well as for space debris. Missions such as GNSS/positioning and altimetry rely on high-fidelity models of all known forces acting on a spacecraft in order to achieve the highest possible levels of accuracy. Accurate force models also reduce the amount of tracking data required for orbit determination. The idea behind the Lorentz study is to see where this effect fits into the hierarchy of forces acting on both active and inactive space objects.

There are three main pieces of information that are required in order to model the Lorentz force for orbit prediction:

- The object surface charge,
- The object velocity in the Earth-Centered Inertial (ECI) reference frame, and
- The magnetic field strength at the object position in the same frame.

The near-Earth space is considered electrically neutral, so there are no polarisation E-fields (i.e. arising from charge separation). However, there are imposed E-fields due to tides in the thermosphere redistributing charge in the global ionosphere, and also large E-fields imposed on the polar regions of the ionosphere by the magnetosphere. The B-field at 160km from the IGRF is between $30 - 50 \times 10^{-6}T$, whereas the largest E-field is mV/m in magnitude in the auroral regions [108]. Therefore, the electric field is assumed to be zero - near-Earth space above 160km is considered to be electrically neutral. Satellite-based measurements show that the magnitude of E is three times less than that of $v \times B$ [104]. This, combined with the large velocity of the satellite, mean that $\vec{v} \times \vec{B} >> \vec{E}$.

The Lorentz force was expressed in Equation 53. Combining the force equation with Newton's second law, we arrive at a mass-dependent acceleration which gives the effect of the Earth's magnetic field on an orbit in the ECI frame:

$$\vec{a}_L(\vec{r}, t) = \frac{q(\vec{r}, t)}{m} \left(\vec{v}(\vec{r}, t) \times \vec{B}(\vec{r}, t) \right) \tag{54}$$

where m is the mass of the object and $\frac{q(\vec{r},t)}{m}$ is the charge per unit mass - also known as the specific charge. This quantity $\vec{a}_L$ is the input to the orbit prediction method.

The first input to the acceleration equation is specific charge. This is the most significant challenge - accurate information on the specific charge across the surface of an SRO (and its time-evolution) is not available. Internal charging is ignored due to Gauss' theorem, as any internal charge can be modelled as a surface charge. Previous studies model the surface charge as a point, to model the net specific charge. For the purpose of this study, the same assumption is made due to lack of detailed information on surface charging. The charging mechanisms in near-Earth space can be modelled based on the following [104, 59, 109]:

- Electron flux (electron scattering and secondary emission currents)
- Ion flux (ion thermal plasma currents)
- Photon flux (electron photoemission)

The International Geomagnetic Reference Field (IGRF) is an empirically-derived mathematical model of the near-Earth magnetic field due to electric currents in the Earth core. The IGRF-11 geomagnetic field model (2009) [110] was used. It is maintained and updated by the V-MOD: Geomagnetic Field Modeling Working Group of the International Association of Geomagnetism and Aeronomy (IAGA). The empirical data is collected at a globally distributed network of ground-based magnetic observatories, as well as from satellite missions such as the CHAMP (Challenging Minisatellite Payload) satellite mission.

As the IGRF models the main geomagnetic field and its secular variation, it ignores the effects of the ionosphere, magnetosphere, solar storms and the solar wind. Magnetic field variations of up to $1\mu T$ are detected during solar storms. This limitation means that the IGRF is only suitable for modelling geomagnetically quiet conditions. The effects of solar storms and the solar wind vary too quickly and can be transient, so the complexities of these are left for future study.

The IGRF represents the geomagnetic field strength vector $\vec{B}(\vec{r},t)$ as the gra-

dient of a scalar potential function $V(\vec{r}, t)$:

$$\vec{B}(\vec{r}, t) = -\nabla V(\vec{r}, t) \tag{55}$$

and V is a spherical harmonic expansion:

$$V(r(r, \vec{\theta}, \phi), t) = a_E \sum_{n=1}^{k} \left(\frac{a_E}{r}\right)^{n+1} \sum_{m=0}^{n} \left(g_n^m cos(m\phi) + h_n^m sin(m\phi)\right) P_n^m(cos(\theta)) \tag{56}$$

where a_E is the mean radius of the Earth, g_n^m and h_n^m are Gauss coefficients of degree l and order m, which are determined from empirical data, and $P_n^m(\theta)$ is the associated Legendre polynomial of degree/order n/m. θ and ϕ are the co-latitude (90deg - latitude) and longitude respectively.

Table 7.3 gives the initial conditions used for the orbital evolution study. Three orbital regimes have been selected, as given in the table. The breadth of these regimes was selected to balance the three components which lead to the Lorentz force:

- Surface charging, which is orbit-dependent
- Magnetic field strength
- Velocity

The three orbital regimes were also chosen to give a broad idea of what the effect might be for every class of orbit.

The "reference" force model is gravitational including Earth oblateness (J2). This simple force model was chosen in order to give results that are easy to interpret, as any differences in orbit evolution can be attributed to the Lorentz force. For each simulation, the gravitational orbit propagation is compared to one including both gravity and the geomagnetic Lorentz force.

The results are presented as the Lorentz results relative to the J2 baseline.

In Figure 7.9, the inclination and semi-major axis are compared for an object in GEO. Over the 23-day orbit track, the Lorentz force causes an increase in semi-major axis of $0.5km$ and an increase in inclination of 6.4×10^{-6} deg. The surface

Orbital regime / example	a/km	e	i/rad	ω/rad	Ω/rad
LEO, NOAA-19	7216	0.0000123	1.717	1.926	0
MEO, GPS	26556.8	0.00135	0.9425	0	0
GEO, MSG2	42164	0.00001	0.0001	0	0

Table 7.3: Initial conditions used in the Lorentz study; LEO, MEO and GEO Keplerian elements

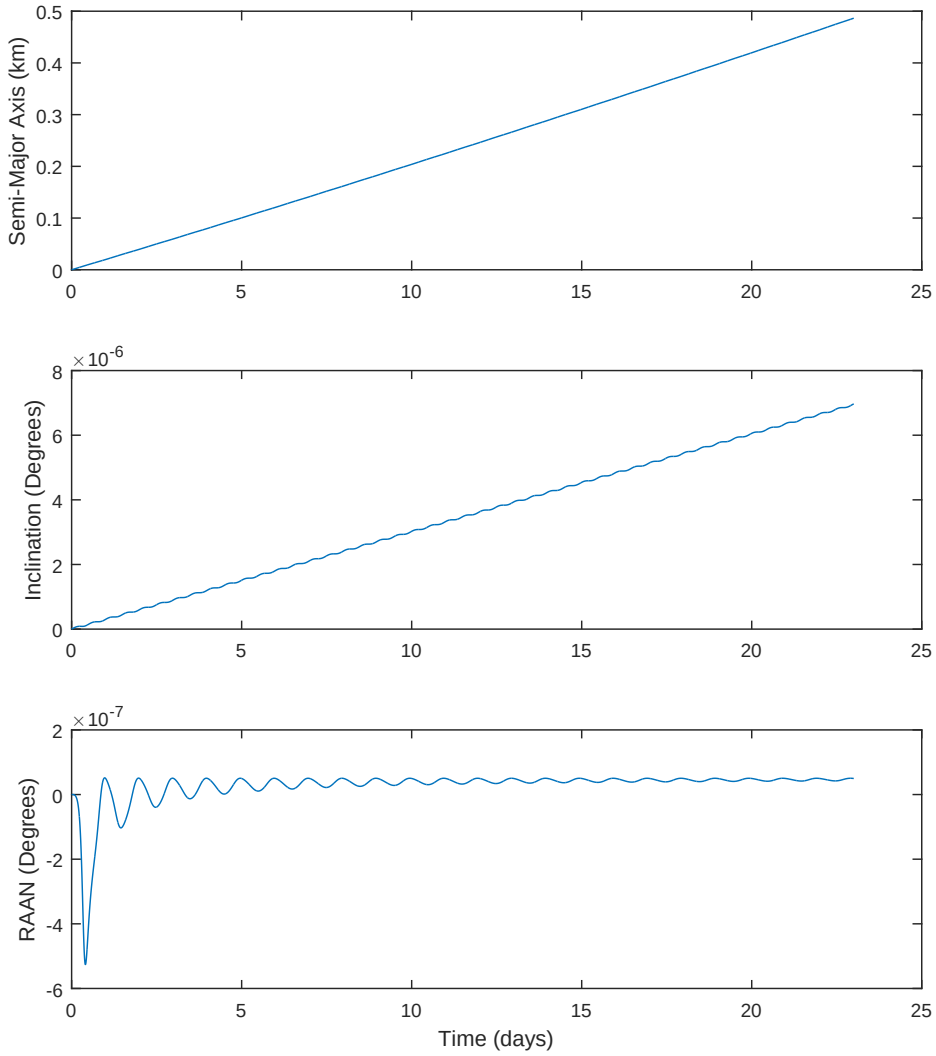

Figure 7.9: A comparison of the evolution, over 23 days, of the orbital elements of an object in GEO with $1\mu C/kg$ specific charge; each line is the difference between the Lorentz force included and excluded from simulations

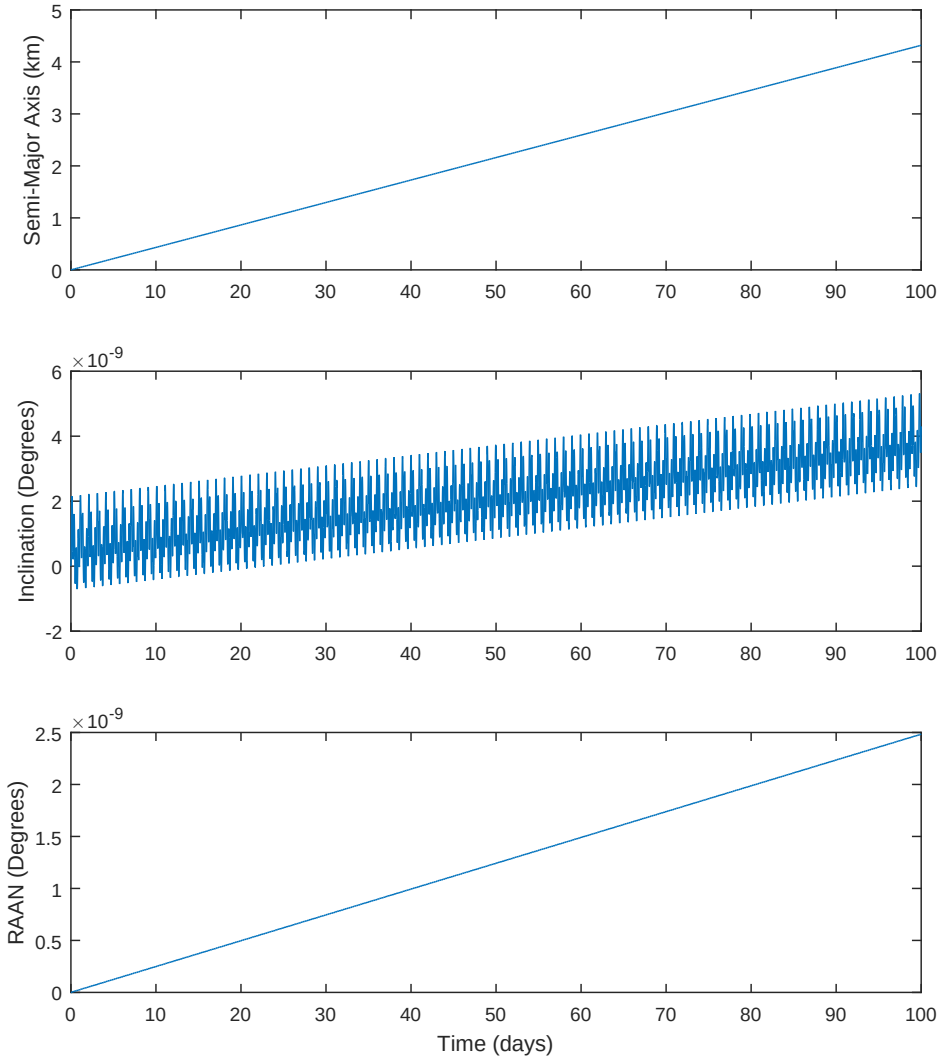

Figure 7.10: A comparison of the evolution, over 100 days, of the orbital elements of an object in MEO with $1nC/kg$ specific charge; each line is the difference between the Lorentz force included and excluded from simulations

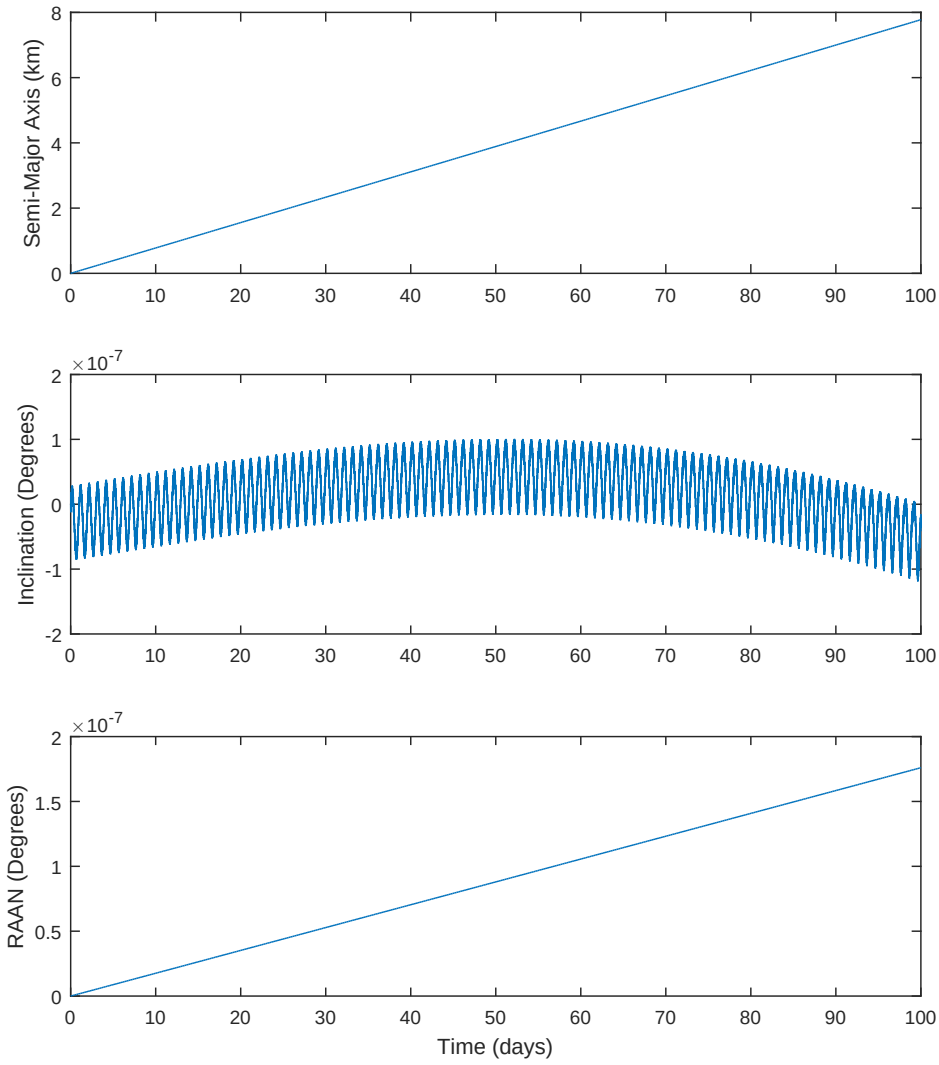

Figure 7.11: A comparison of the evolution, over 100 days, of the orbital elements of an object in LEO with $1nC/kg$ specific charge; each line is the difference between the Lorentz force included and excluded from simulations

charge was increased for this simulation in order to increase the force on the object in the ECEF frame - an object in GEO has little to no velocity with respect to the Earth surface. It should be noted that this part of the study is most limited as it is on the boundary of the applicable regions for the IGRF magnetic field model.

In Figure 7.10, the inclination, semi-major axis and RAAN are compared for an object in MEO. Over the 100-day orbit track, the Lorentz force causes an increase in semi-major axis of $4km$, and a relative increase in both inclination and RAAN. The inclination has periodic signatures on a daily timescale.

In Figure 7.11, the inclination, semi-major axis and RAAN are compared for an object in LEO. Over the 100-day orbit track, the Lorentz force causes an increase of semi-major axis, and an decrease of RAAN and an increase then decrease of inclination in comparison to a simulation without the Lorentz force. The semi-major axis increases by $8km$.

This pilot study was to broadly determine the maximum influence that the geomagnetic field might have on the trajectory of objects in near-Earth orbit and to place the Lorentz force within the hierarchy of perturbations of orbits. The Lorentz acceleration was computed, under a set of simplifying assumptions, using the IGRF for three test orbital regimes. The results suggest that the Lorentz force could play a role in altering the orbital regime of uncontrolled objects through changes in semi-major axis, inclination and RAAN in the LEO, MEO and GEO regimes, depending on the surface charge. Further study is required to model charging mechanisms, and additional information which quantifies the surface charge on passive objects is required to validate the predictions presented.

Chapter Summary

This chapter has presented three separate areas of study: observation of Envisat tumbling, the use of nanosatellites to imitate debris to enable more detailed analysis of the near-Earth environment, and the results of a pilot study into the effect of the Lorentz force.

8 Discussion

Chapter Outline

The previous chapter presented an analysis of the results obtained using the methods implemented in this study. This chapter discusses the relevance and broader application of these results, and their use within the SSA community.

8.1 Envisat tumbling

It has been shown that Envisat changed from having a fixed attitude, before loss of communication, to an uncontrolled tumbling state. This uncontrolled tumbling cannot be explained by the natural influences of the space environment as predicted by gravitational and radiation torques 6.1. An important conclusion is therefore that the tumbling of Envisat and its current attitude evolution are a result of an external influence. This might be due to a failure of its attitude control system, resulting in angular momentum being dumped from reaction wheels into the spacecraft and thus an unpredictable tumbling evolution. Another possibility is a collision, although imaging from other satellites shows that Envisat is broadly intact.

8.2 Tumbling of space debris

Based on the orbital simulations of objects tumbling and with fixed attitude, the periodic and secular effects have been analysed. They show that the effect of tumbling is to dampen the effects of non-conservative forces, although the tumbling rate did not change how these forces perturb the orbit.

These results are important for both active and uncontrolled objects. For uncontrolled objects, the torques cause changes in attitude which modify how non-conservative forces act on an SRO. The effect of constant tumbling rates has been shown to dampen the effects of non-conservative forces, but their effect on orbital motion is still experienced. The rate of tumbling did not change how large an effect was caused by non-conservative forces.

For asymmetric active objects, with a controlled and fixed attitude, the effects

of non-conservative forces will be dependent on the torques. That is, a proportion of the incident energy will be transferred into angular momentum through the torques, which will be picked up by the attitude control systems. Thus a pure force modelling approach is likely to overestimate the non-conservative forces; the physical basis of non-conservative effects is split into forces and into torques, but a force-only modelling approach attributes the entire physical effect to translational motion. The balance of energy input from non-conservative pathways leading to translational versus rotational motion requires further analysis, but this study has illuminated important considerations not only for torque and attitude modelling, but also for force and orbit modelling.

8.3 Additional work

8.3.1 Nanosatellites

Initial suggestions for the use of nanosatellites as "intentional debris" have been made. This is so that their debris-like characteristics can be used in the validation of modelling techniques against real-world data, which is difficult to obtain through observation alone. Nanosatellites can transmit accurate data regarding their position, velocity and tumbling, which should be compared to simulation results in order to validate the methods used. Further to this, such objects could be attached to items which would otherwise become debris, such as instrument covers, in order to give them an electronic "tag" which can be tracked. In LEO, drag is an important consideration so this would also need modelling in a detailed study of nanosatellites.

8.3.2 Geomagnetic Lorentz Force

It has been shown that the geomagnetic Lorentz force has the potential to change semi-major axis (make orbits larger or smaller), inclination (tilt them with respect to the Earth), and RAAN (cause the orbital plane to precess about the Earth). These might form a part of the unexplained orbital evolution of uncontrolled objects in near-Earth space such as Envisat, under specific assumptions about their surface charge. Any influence which has the potential to change orbital elements can cause

debris to float into operational zones and therefore warrants further investigation, as the result of changes in orbital elements can lead to a cluttering of operational zones.

Other uses for geomagnetic modelling would be to detect orbital regimes which might attract debris in the longer term (for example, if the balance of forces and torques means that a particular region of orbits is more favourable for debris), but also for the potential effect of de-orbiting. Active charging might be used as a way to influence the orbits of end-of-life objects over the longer term, without the need for propellants; either into "graveyard" orbits or for the purposes of de-orbiting and meeting the 25-year de-orbiting criteria.

9 Conclusions

Chapter Outline

Section 9.1 gives a brief review of the problem statement and method of study, along with the broad conclusions inferred from the results presented in this thesis. Sections 9.2.1-9.2.6 give a more detailed account of the research contributions and relate each conclusion to the aims and objectives in Chapter 4.1. Finally, Section 9.3 presents the areas highlighted through the study which could be addressed in future work.

9.1 Overview of study

The basis of this study is the characterisation of orbit and tumbling evolution of uncontrolled manmade objects in near-Earth space. The field of SSA has been a focus in the space community in the past 3-6 years, and the application of computational techniques to radiation torque modelling and attitude evolution is a relatively new field with ESA announcing their ιOTA software development in late 2015. The main aims of this research were given in Chapter 4.1. The method applied to this problem was two-fold; firstly, a high-fidelity method for calculating radiation pressure torques on complex SROs was developed, and this was combined with an attitude propagation model in order to predict the attitude evolution of HAMR objects under radiation torques alone. Second, a toolset was developed to enable simulations of objects tumbling in orbit, including the effects of non-conservative forces, in order to predict the effect of tumbling on orbit evolution.

The objectives have been met through the application of these methods, leading to the principal conclusions of this study which are grouped into themes:

Conclusions

Existing constellation

- A subset of space debris have HAMR properties and have been observed tumbling with a period of 0.2s-30s. However, the origin and nature of these objects is uncertain. Their spin behaviour affects their orbital motion strongly, due to non-conservative forces.
- The existing constellation of debris is clustered into a few notable regions, described in Section 2.4: broadly speaking there are three regions in LEO, MEO and around GEO.

Torque modelling

- Gravitational and radiation torques can dominate the attitude motion of SROs depending on their physical characteristics and initial conditions.
- Radiation torques on Envisat are an order of magnitude smaller than gravitational torques based on the models presented; the effect on angular acceleration is $1.47 \times 10^{-6} rad/s^2$ for gravity versus $7.5 \times 10^{-7} rad/s^2$ for radiation. This is in agreement with initial results that were recently published by ESA based on ιOTA simulations.
- Under the influence of radiation torques alone, SROs with an optical geometric asymmetry and a HAMR may either spin-up or oscillate about an equilibrium state. Based on the models developed in this thesis, Envisat spins up at a rate of $7.5 \times 10^{-7} rad/s^2$ about the y-axis under radiation torques alone, due to its large single solar panel.
- Radiation torques alone do not explain the evolution of the Envisat satellite since its death, leading to the potential failure of an attitude control system as the cause of its spin evolution.
- Visualisation of the radiation torques, in a way which enables quick and easy characterisation of the torque effects to be drawn even for complex SROs, is important in understanding this complex phenomenon.

Orbital perturbations caused by tumbling

- Non-conservative forces perturb the orbit of SROs with both secular and periodic effects, and tumbling dampens these effects on the orbital elements that describe the orbit of an SRO.

Additional study

- The novel idea of using nanosatellite technology as a testbed for investigating the orbital dynamics of space debris has been presented. Nanosatellites are a promising technology for both the validation of models of space debris, and for scientific testing of the effect of the near-Earth space environment on SRO orbit evolution and lifetime.
- The Lorentz force is not negligible and needs further investigation using real-world test data in order to characterise its effect on the orbit of satellites and space debris. Pilot studies into electromagnetic interactions have shown it may be an overlooked effect in the near-Earth space environment. The effect shows potential to move SROs from one orbital regime into another; further analysis into the nature of surface charging and its magnitude are necessary. For collision and breakup debris, the material properties may lead to unusual surface charging due to varied material properties across the various fragments.

Each of these conclusions are discussed in more detail in the following sections, followed by proposals for the next steps in research in this field.

This study is an initial step in computational torque and attitude modelling of space debris and hence the approach taken here is broad, in order to understand the problem domain and to set a framework for future work. This would feed into both conjunction analysis through improved orbit prediction, and into the tasking of observation equipment through improved knowledge on attitude and hence observability. There are many suggestions for future work; one is reminded of the sentiment of Wordsworth as given at the start of this thesis. While the near-Earth space environment has become cluttered through human activity, it is through the application of science and intellect that we can learn more about how objects move around the Earth. Through the analysis of forces exerted by the

combined effects of the solar system, we can learn more about our solar system and work towards a remedy for this problem.

There were some concerns raised about the validity of the results for two main reasons: the initial tumbling conditions are so difficult to acquire, and the lack of drag torque analysis. The key response to these points respectively is firstly that these results enable calculation of envelopes of potential orbital regimes for spinning objects, but also that future improvements in sensor technology may well enable improved acquisition of initial conditions. For the second point, this thesis is dedicated to the study of space debris - the objects of concern are those where the orbital lifetime is many decades or more. For these objects, the effects of drag are small in comparison to other forces, as drag is a key factor in orbital lifetime. This is corroborated by other research groups.

9.2 Principal conclusions

9.2.1 Radiation torque modelling

A method for computing the torque exerted by SRP on objects of arbitrary shape was developed. This method was then verified on test objects, through black-box testing for simple objects compared to manual calculations. The method implemented allowed radiation torques to be calculated for one of the most massive and geometrically complex satellites in orbit: Envisat, with an end-of-life mass of 7827.9kg and with 1100 individual components required for a high-fidelity representation. The results for Envisat were presented in the form of torque maps such as the one given in Figures 6.3 - 6.5. Under radiation torques alone, it has been shown that the spin period for Envisat could decrease at 1.02×10^{-2} seconds per day due to its optical geometric asymmetry. Simulated spin behaviour derived from the torque model 'behaved as expected' - that is, it agreed with first order expectations. The spin-up behaviour is as expected due the optical geometric asymmetry of the panel on one side of the bus, the differences in optical properties of the front and back of the panel, and the shadowing of the panel by the spacecraft bus.

The main conclusion is that whilst gravity is the main driver of attitude motion through secular effects (as the torques induced are largest), the effect of radiation torques has both secular and periodic effects. The gravitational torques are an order of magnitude larger than the radiation torques. Further to this, whereas gravitational torques adjust the attitude of the SRO with respect to the Earth (or other massive body), radiation torques depend on Solar position in the body frame of the SRO. The combination of these gives a complex attitude motion, and further study is required in order to characterise the full complexity. This could be through a full 6dof simulation suite, as proposed in Section 9.3.1.

An additional intuition has been gained through this work: force modelling, in the absence of any consideration of attitude, leads to an overestimation of force for asymmetric objects. This is because some of the incident energy is transferred to angular momentum for asymmetric objects. This is important for both active and inactive objects in orbit.

9.2.2 Visualisation methods

The output of radiation torque simulations is given as grid files. These are difficult to draw useful conclusions from without further analysis, so a method was devised to represent the output in an easy, 'at-a-glance' view of the full complex system dynamic. This is analogous to a simple statistic that captures and summarises a complex array of information and makes it easily understandable. The concept of torque maps enables an intuitive way of presenting torques in the body frame of the SRO. An example torque map is given in Figures 6.3 - 6.5.

9.2.3 Analysis of existing constellation

Through the analysis of TLE datasets, there are some notable conclusions that can be made about the current SRO constellation:

- The constellation is made up primarily of debris items and spent rocket bodies. These are passive and pose a threat to future space missions.
- The constellation is more concentrated in 3 orbital altitudes as defined by semi-major axis: LEO (100-2000km), MEO (21,000-26,000km) and around the GEO belt (41,000-46,000km). This corroborates the analysis of other studies and highlights the importance of the space debris problem as the majority of active satellites that underpin technology in modern society are in these altitude ranges.
- The majority of current SROs (56% of those in the TLE database) have a low eccentricity ($e < 0.1$)and high inclination ($60 - 105°$)
- The RAAN of the current constellation indicates that more objects enter the northern hemisphere in the 180° to the west of the first point of Aries (7,906 SROs) than in the 180° to the east of the first point of Aries (7,141 SROs). The RAAN is secular and so this distribution is time-dependent but this offers a snapshot glimpse into the distribution.

These conclusions are in line with other analyses of the constellation and give insight into the most important regions which require analysis through the methods applied in this thesis.

9.2.4 Trajectory analysis

In order to characterise the effect of non-conservative forces on rotating objects, a set of simulations were run. These simulations compare objects which are fixed in inertial space to have the maximum effect from SRP, objects which rotate at a fixed rate, and objects which are fixed to have a minimum effect from SRP. The results show both periodic and secular changes, and the rotating simulations always show effects somewhere between those of objects fixed in inertial space with minimum and with maximum radiation effects. The conclusions that we can draw from these simulations are that the effects of SRP are dampened by rotation.

9.2.5 Nanosatellites as a debris test platform

There are two potential uses for nanosatellites in the context of SSA: as artificial, trackable objects which have properties similar to space debris, and also as a means to tracking future objects which will become debris by tagging them - effectively turning them into actively transmitting satellites. This is achieved by attaching lightweight PCBs to such objects to effectively turn them into nanosatellites by enabling transmission and reception of signals. Nanosatellites are also promising for the study of SRO dynamics because of their low cost, short orbital lifetimes in LEO, ease of tracking and similar physical characteristics to HAMR debris. In this scenario, nanosatellites can be used for validation and for scientific testing of the effect of the near-Earth space environment on HAMR SRO orbit evolution and lifetime.

Potential designs of nanosatellites for these purposes were discussed, including methods to induce radiation torques in order to validate a 6dof orbit and attitude prediction suite. These were intended for application and flight with the KickSat project, but unfortunately, the involvement with the KickSat project was not possible due to technical difficulties.

9.2.6 Additional work

Initial studies of the Lorentz force have shown that it can have a significant effect on an orbit, with the potential to change the orbital regime through semi-major axis, inclination and RAAN. This effect may be a factor in the divergence and spreading of objects throughout orbital regions after a breakup event.

9.3 Future work

There are several extensions which are highlighted and could be conducted in future studies in the field. These are given, in approximate order of importance, in the following sections.

9.3.1 Orbit-attitude coupling

A key difficulty is the link between orbit and attitude - due to the fundamental differences in how these influence an object, it is difficult to simulate them simultaneously. In order to overcome this problem, the simulation of attitude and of orbit are separated.

In order to study the coupling between orbital and tumbling motion, a full 6dof simulation suite is required. This would take the radiation force and torque outputs (grid files), and integrate these numerically in combination with other advanced force and torque models. The orbit propagation would be called less frequently than the attitude model, as the tumbling evolves more quickly.

Suggestions for such a simulation suite would include Lie variational or symplectic integration for the attitude motion, as the attitude space is nonlinear. For the orbital motion, a linear approximation is suitable and so Runge-Kutta is sufficient for translational motion. The reason is this that RK methods split a timestep into equal segments, whereas symplectic and collocation use segments which are not equal and so not linearly spaced. This is advantageous in non-linear spaces such as rotation [111]. McCullough *et al.* [112] find that even a fourth-order Runge-Kutta integrator provides an excellent balance of accuracy to computational runtime for orbit propagation. Montenbruck [97] shows that if velocity-dependent terms are not included (Lorentz force and drag), then RK methods are most efficient.

The final product here would be a complete 6dof orbit and attitude simulation suite where the two are coupled but integrated separately to account for the differing timescales for evolution in orbit and attitude. Given the initial conditions, firstly the torque and attitude model would propagate forwards and then call the force model when the attitude has changed beyond a given threshold. This way, the orbital effect of non-conservative forces can be modelled more completely.

Energy and momentum conservation laws must be modelled fully in a 6dof simulation suite. The non-conservative forces alter the energy state of the SRO, and there is a balance of energy transfer into linear and rotational kinetic motion. The incident radiation flux carries a fixed amount of energy and so current techniques of radiation pressure force modelling overestimate the radiation forces for active satellites. This is because some of the energy drives attitude motion, which is then withdrawn by the attitude control systems and thus this portion of incident radiation does not lead to a net force acting on the spacecraft.

A complete 6dof modelling suite would include the following (including order-of-magnitude estimates):

Forces

- High-order gravity model ($10^{-2} kms^{-2}$)
- Radiation pressure (Solar, reflected Earth and emitted Earth radiation) ($10^{-10} kms^{-2}$)
- Third body (Lunar, Solar, planetary) gravity ($10^{-9} kms^{-2}$)
- Lorentz force ($10^{-16} kms^{-2}$)
- Drag (highly shape- and altitude-dependent)

Torques

- J2 gravitational ($10^{-6} rads^{-2}$)
- Radiation pressure ($10^{-7} rads^{-2}$)
- Drag (highly shape- and altitude-dependent)

The inputs required would include the force and torque models, physical SRO properties (geometry, moments of inertia, optical and thermal properties), and initial conditions. Outputs would include orbit and attitude propagation, but also graphics which enable quick intuition into the motion. This might be through

graphs of attitude dependence for each force or torque for that specific object, force and torque maps, and azimuth plots of expected precession of the spin axis.

9.3.2 Extensions to radiation force and torque modelling

To model the effects of radiation more completely, there are some extensions to the methods presented in this thesis. The Sun is the most intense source of radiation, however the Earth also emits and reflects radiation. The Solar radiation is reflected by clouds, land and water, and the Earth also emits a very low-frequency photon distribution based on Wien's displacement law. While these are implemented in newer versions of the radiation force modelling suite, they should also be implemented in the radiation torque modelling software.

The frequency-dependence of the radiation pressure has been neglected here. Also, the frequency-dependence of the material surface properties has been ignored.

For objects with an asymmetry that leads to radiation torques, improved modelling of shadowing could lead to more accurate simulations. If Envisat were to move from Earth shadow, into the penumbra and then into the full-phase region where solar radiation is direct, it is important to consider which part of the spacecraft body is illuminated first. If the satellite entered full-phase panel-first, this would lead to a larger torque than if the bus were illuminated first.

The current code, written in C++, could be sped up through modern ray tracing techniques; recent developments in GPGPU technology such as CUDA are ideally suited to this "embarrassingly parallel" problem. Double precision ray tracing can be achieved on GPUs, and so an extension to the pixel array method could be implemented in a GPU-based software package, with direct input of CAD models with reflectivity and specularity data added on, rather than the intermediate "USER" files.

9.3.3 Drag torque modelling using the pixel array method

The drag on space vehicles is caused by the sparse atmospheric particles interacting with the surfaces of the vehicle. The pixel array method enables the simulation of an incident flux on an SRO of complex geometry. An extension to this method

could simulate the particle flux, by replacing the optical properties in the input file with surface roughness in order to calculate aerodynamic forces and torques without the need for a full fluid dynamics simulation. This is a good assumption because the mean free path of particles in near-Earth space is of the order of $10^2 - 10^5 km$ so to first order the particles do not interact with each other and can be treated independently.

9.3.4 Electromagnetic interactions and the Lorentz torque

The geomagnetic Lorentz force was calculated based on simplifying assumptions:

- Fixed point-charge
- No local electric field
- Magnetic field originating solely from the Earth (i.e. ignoring solar magnetic interactions and storms)

The fixed point charge assumption is the most limiting, as in reality the charge is both spread over the surface and evolves in time. More data is required on the charging mechanisms as an input to such simulations. For a detailed description of surface charging, the pixel array method can be used to compute photoemission of electrons as the photon interactions with the surface are already simulated. Additional information on the photoemissive properties of each component would enable this extension. Alternatively, empirical data from sensors on spacecraft could be used to build a map of how satellites become charged in different orbital regimes.

The IGRF model used also has limitations in its applicable regions. To extend to further orbits and model the effects of magnetism on GEO orbits more precisely, TS geomagnetic field models [113] could be used.

Appendices

Personal contributions

TEDxUCL presentation

To bring the issue of space debris to the wider intellectual community and engage with members of the university, a TEDxUCL talk was given in July 2013 . The title was "Space Debris: Isolation of Humankind?". There were several intentions in giving such a talk:

- Raising awareness of the problem of space debris
- Reaching out to the broader community for ideas and potential collaborations
- Clarification, collation and revision of the basics of space debris through the process of explaining them in simple terms to an unfamiliar audience

A video recording of the talk is available to view on the TEDx YouTube channel [114].

Non-conservative torques

This paper was presented at the American Institute of Aeronautics and Astronautics (AIAA) conference in San Diego [115]. This was a specialist American Astronautical Society (AAS) Astrodynamics conference with a focus on astronautical spaceflight including SSA, satellite operations and interplanetary missions.

This paper covers the pixel array method for calculating radiation torques on Envisat.

SPACE Conferences and Exposition
4-7 August 2014, San Diego, CA
AIAA/AAS Astrodynamics Specialist Conference

Non-Conservative Torque and Attitude Modeling for Enhanced Space Situational Awareness

Hira S. Virdee[1], Santosh Bhattarai[2], Stuart Grey[3] and Marek Ziebart[4]
University College London, Gower Street, London, WC1E 6BT, UK

The tumbling of space debris is an important problem, as the evolving attitude of debris directly influences the forces on it and therefore perturbs its orbit. This paper investigates the torque induced by solar radiation pressure (SRP) on Envisat and the resulting changes in attitude. These changes are compared to observations.

Nomenclature

τ	=	Cartesian torque vector
I	=	Moment of inertia about each Cartesian axis (*Ix, Iy, Iz*)
Θ	=	Displacement angle about a given Cartesian axis

I. Introduction

THE tumbling of uncontrolled space objects has a direct impact on their orbits, through attitude-dependent perturbations in non-conservative forces such as radiation pressure and drag. These are particularly important for high area-to-mass ratio* (HAMR) objects such as space debris. Changes in attitude lead to changes in surface force, such as solar radiation pressure (SRP). Understanding in this area could lead to improved models of the spatial distribution of space debris, enhancing space situational awareness (SSA). It could also lead to innovative methods for influencing debris with a view to de-orbiting.

Whereas active satellites have control mechanisms to periodically adjust their orbit and attitude, debris have no attitude or orbit control mechanisms. Forces and torques therefore have a more direct and irreversible effect on the orbit and attitude of the uncontrolled debris which reflects more directly the natural influences of the space environment. The tumbling of space debris has been observed, and it is hypothesised that SRP is a significant factor in the perturbation of space debris orbits[1]. It is therefore important to take this into account in an advanced model of space debris orbits.

In this paper, a method for the high-fidelity calculation of SRP torques is described; this method has been implemented. The calculated SRP torques for Envisat are visualised. The results of simulations of the evolution of the attitude of Envisat are given and compared to observations.

II. Background

The equations of motion for torque modeling are similar to those for force modeling. In torque modeling, the equation of motion is given by Euler's dynamical equation; see Eq. (1).

$$\tau = I\ddot{\theta} \tag{1}$$

where τ represents the torque exerted on an object in three dimensions, I is the moment of inertia and $\ddot{\theta}$ is the angular acceleration vector, also denoted $\dot{\omega}$.

---

[1] PhD Researcher, SGNL, Chadwick Building, UCL. Gower Street, London. WC1E 6BT. AIAA Student Member. hira.virdee.10@ucl.ac.uk
[2] PhD Candidate, SGNL, Chadwick Building, UCL. Gower Street, London. WC1E 6BT. AIAA Student Member.
[3] Lecturer, SGNL, Chadwick Building, UCL. Gower Street, London. WC1E 6BT. AIAA Member.
[4] Professor, SGNL, Chadwick Building, UCL. Gower Street, London. WC1E 6BT. AIAA Member.
*HAMR objects are defined as having $\frac{A}{m} > 1m^2/kg$

The torque is found by summing the moment of each force about the center of mass, just as linear forces are summed to find an acceleration. There are three main torques on space-resident objects (SROs): gravitational, aerodynamic drag and radiation[2]. Here, the term SRO is used to encompass both active satellites and space debris as the torque modeling methods described are applicable to both.

$$\tau = \tau_{grav} + \tau_{drag} + \tau_{rad} \quad (2)$$

Other torques may also need to be considered in a complete approach, such as the Lorentz torque and the YORP effect[3]. The Lorentz torque arises due to the interaction of differential SRO surface charging with the geomagnetic field, and the YORP effect is a result of asymmetric heating and cooling as an object tumbles.

For application to HAMR debris at higher altitudes, the gravitational and drag torque are negligible in comparison to radiation torques. This paper focuses on the radiation pressure torque caused by solar illumination of an SRO.

There are four main factors that affect the magnitude of the SRP torque:

1. Orientation of the body with respect to the solar radiation flux
2. Reflection characteristics of the various surfaces, which describe how incident radiation is reflected and absorbed
3. SRO geometry, which determines asymmetries that lead to torques
4. Shadowing effects – both of the entire body being in umbra, and for the effect of one part of an SRO shadowing other parts of the same object.

Torques on SROs are caused by asymmetries in physical geometry and asymmetric forces. Torques are also induced on objects which have a center of mass that is not at the geometric center of the object. The center of mass and moment of inertia can be calculated from the geometry of the SRO. Envisat is an example of a highly asymmetric object, as it has a large solar panel that is separate from the main satellite bus.

The center of mass of complete satellites is variable, due to fuel tanks emptying and the sloshing of fuel. Some satellites also have spinning momentum wheels which contribute to the gyroscopic stabilization of attitude. For the purposes of this analysis these effects are ignored, as the models are intended for application to HAMR debris.

The physical characteristics (mass, area, center of mass, moment of inertia) are difficult to obtain for debris in orbit. Such characteristics may be obtained through fragmentation experiments[4], or derived from observations[5]. Examples of debris known to be tumbling include the MSG2 cooler cover[5] and Envisat[6].

III. Method

The Space Geodesy and Navigation Laboratory (SGNL) research group at University College London (UCL) has a heritage in the high-fidelity modeling of solar radiation pressure forces[7,8]. The existing code has been validated on numerous missions[8]. The computational approach is to place an array of photon-emitting pixels at a given position relative to the SRO. The intersection of these emitted photons with the SRO geometry is then calculated. The material properties (reflectivity and specularity of the surface) are used to find the proportion of photons that are reflected along with their direction. These are then used to find the force exerted on the SRO, and the force exerted by each pixel in the array is then summed over an array that spans the geometry of the SRO. This method is described in more detail in (Ref. 7,8).

This code was extended to calculate the torque exerted. The center of mass is specified, and thus the torque arm is from the center of mass to the intersection point of the photon with the SRO surface.

In order to demonstrate the high-fidelity modeling technique, Envisat was chosen. The reasons for this are the observation of Envisat to be tumbling, and its well-known physical properties. However, the orbital altitude of Envisat is low (790km) so the drag torques are significant, and the large size and mass of Envisat mean that the gravitational torques are significant. It also has a low area-to-mass ratio, and so it is expected that the SRP torques are not sufficient to explain its tumbling.

A comparison of a rendered image of Envisat to the high-fidelity model used in these simulations is given in Fig. 1. The numeric data pertinent to the attitude simulations, that is the moment of inertia and center of mass, is given in Tables 1 and 2. An attitude model based on Euler angles was implemented. This utilizes the calculated SRP torques to find the attitude evolution over time.

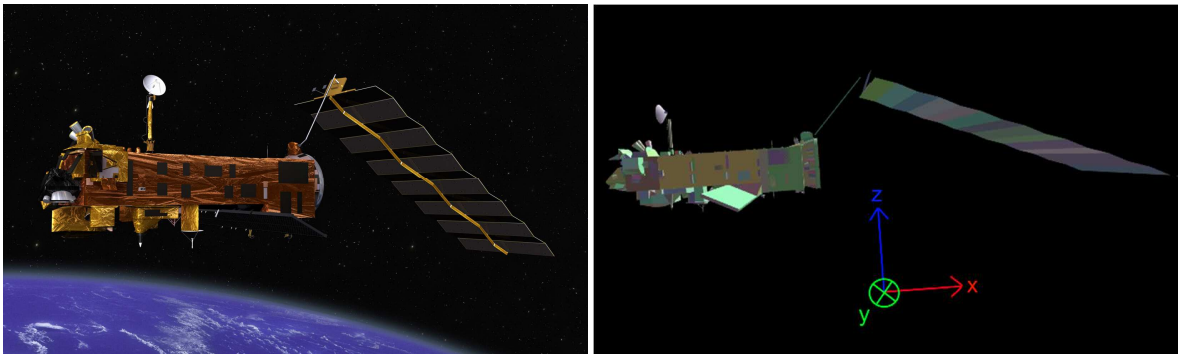

Figure 1. **A rendered image of Envisat (© ESA) compared to the model used in the high-fidelity SRP approach.**

Table 1. **The center of mass of Envisat[9].**

	Mass (kg)	Centre of Mass		
		x (m)	y (m)	z (m)
Initial	8106.4	-4.635	-0.020	-0.039
Final	7827.9	-3.905	-0.009	0.003

Table 2. **The moments of inertia of Envisat[10].**

Ix (km m²)	Iy (km m²)	Iz (km m²)
17023.3	124825.7	129112.2

IV. Results

The results of the SRP torque analysis are given separately for the torque about each axis. This is because the torque about each axis is independent of the torque about the other axes. The torque is plotted as a function of the latitude and longitude of the Sun in the body frame of the SRO, and is given separately for the torque about each axis. The direction of these axes are given in Fig. 1 above. An intuitive method for reading these "torque maps" is to trace along a particular latitude or longitude and to read the resulting changes in the exerted torque.

Figure 2 shows the SRP torque about the x-axis for Envisat. The torques about the x-axis range from $6x10^{-5}$ Nm to $-6x10^{-5}$ Nm. There are four main features in the graph. These are the maxima and minima in torque about the x-axis, which occur at approximately ±45° latitude and ±90° longitude. Another interesting feature is that the torque about the x-axis is smaller when the Sun is in a position with a positive latitude, compared to the same negative latitude. The asymmetry of the torque about the x-axis is a result of the shadowing of the bus solar array by the bus for positive latitudes.

Figure 3 shows the SRP torque about the y-axis for Envisat. The SRP torque is dominated by the large 15m x 6m solar array which is separated significantly from the center of mass. The torques about the y axis range from $1.5x10^{-3}$ Nm to $-1.5x10^{-3}$ Nm. The torques depend directly on the latitude; when the Sun is above or below the solar array there is a large torque about the y-axis. There is also a small variation of torque with longitude, due to the shadowing of the main bus by the solar array and the varying material properties of the bus with longitude.

Figure 4 shows the SRP torque about the z-axis for Envisat. They range from $-5x10^{-4}$ Nm to $5x10^{-4}$ Nm. The two minima and two maxima in torque about the z-axis are similar to the torques about the x-axis, but the key difference is that the torques about the z-axis are symmetric about the xy-plane. That is, for positive and negative Solar latitudes at any given longitude, the torque is similar. Here again, there is an asymmetry in the torque that is caused by self-shadowing effects and by the different material properties of the top and bottom of the bus.

These torque maps were combined with an attitude model. The evolution of the angular velocity of Envisat about the x-axis as a result of SRP torques over several orbits is given in Fig. 5, and about the y-axis in Fig. 6. Due to the smaller torque about the z-axis and the higher moment of inertia about the z-axis, the equivalent graph about the z-axis has been omitted. These simulations show that changes in angular velocity are caused by SRP torques over the timescale of several orbits, although they are small. The graphs are plotted relative to the initial angular velocity in order to highlight the changes due to SRP torques.

Longer simulations were also run, and their average effect on the Envisat attitude are given in Table 3.

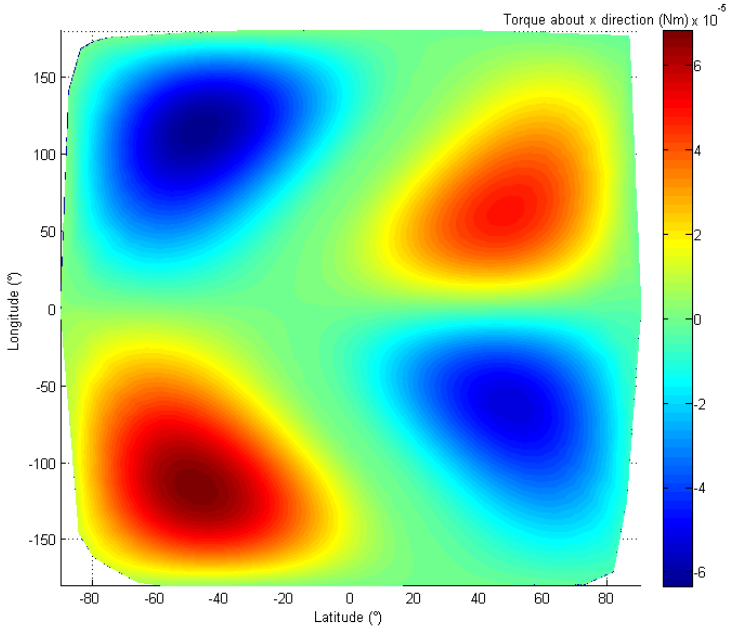

Figure 2. **A map of the torque about the x-direction for Envisat, for each latitude and longitude of the Sun in the body frame of Envisat.**

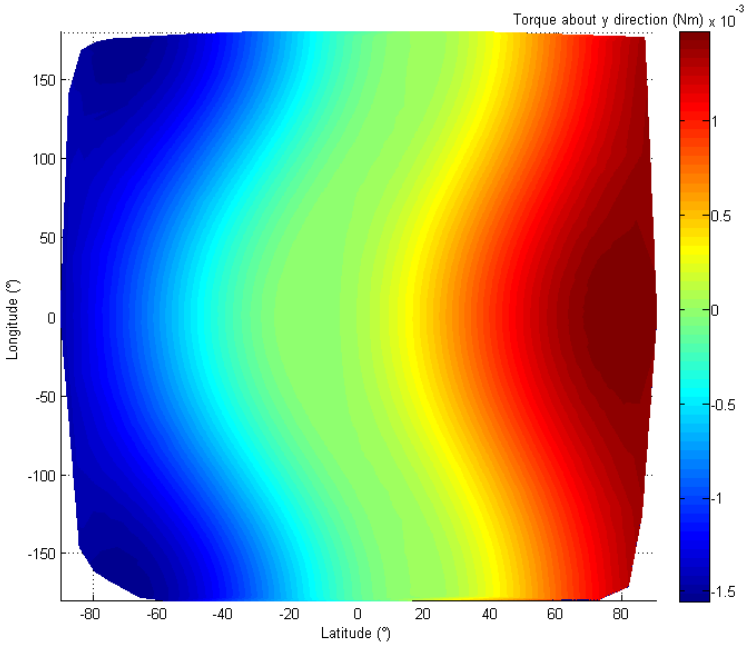

Figure 3. **A map of the torque about the y-direction for Envisat, for each latitude and longitude of the Sun in the body frame of Envisat.**

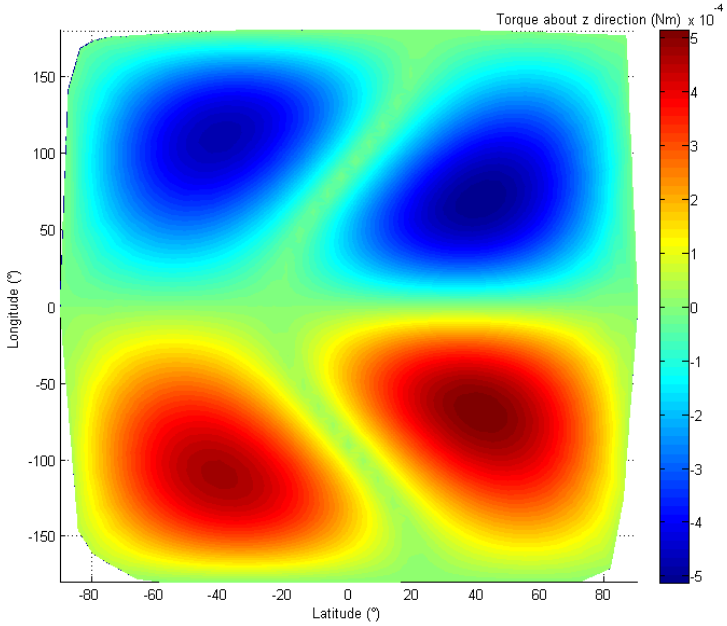

Figure 4. **A map of the torque about the z-direction for Envisat, for each latitude and longitude of the Sun in the body frame of Envisat.**

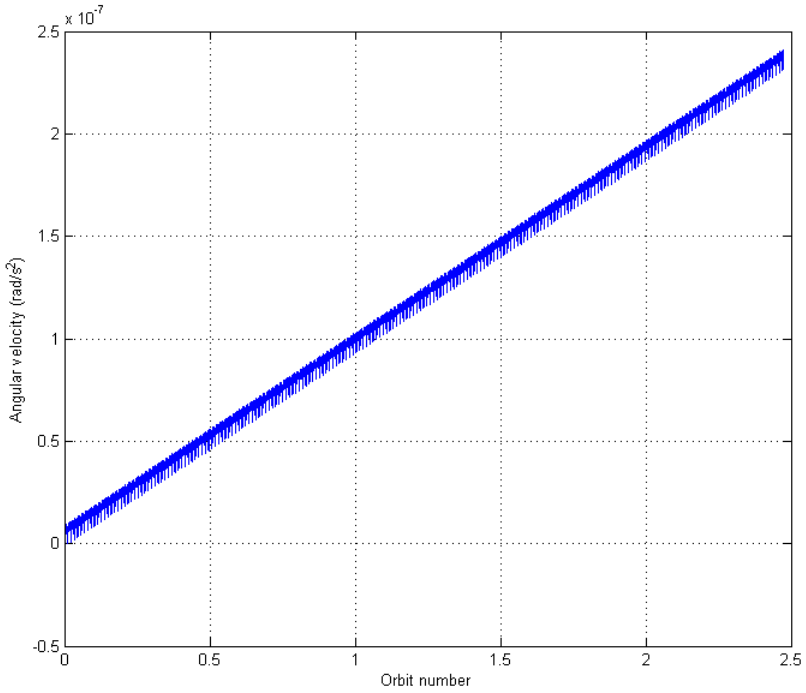

Figure 5. **The evolution of the relative angular velocity about the x-axis of Envisat under the influence of SRP torques.**

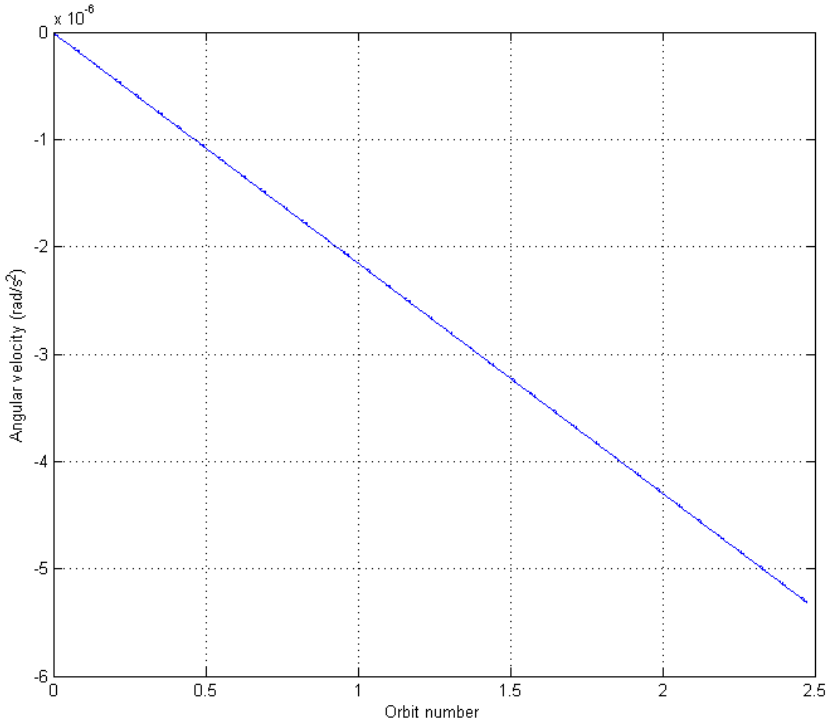

Figure 6. **The evolution of the relative angular velocity about the y-axis of Envisat under the influence of SRP torques.**

Table 3. **The evolution of the period of rotation of Envisat due to SRP torques, about the body frame x-, y- and z-axes**

Axis	Change in period per day (s)	Angular acceleration (rad/s²)
x	3.04E-04	2.21E-08
y	1.04E-02	7.55E-07
z	3.34E-04	2.43E-08

V. Discussion

The Envisat mission ended on 8th April 2012 when communication with the satellite was lost. At this point, the satellite was not tumbling. Observations have shown that the rate of tumbling increased up to a period of 134.74s in September 2013, and the tumbling rate has subsequently been observed to be decreasing – the period is increasing at a rate of 36.7ms/day about the spin axis[6].

Comparing the recently observed tumbling rate to the simulation summary in Table 3, it is apparent that SRP torques do not explain the full attitude dynamics for a low area-to-mass object such as Envisat, as expected. Further investigation is needed in order to determine which torques cause the tumbling of such objects.

The maximum area-to-mass ratio of Envisat is 0.0166 m^2/kg. HAMR objects are those with $A/m>1 m^2/kg$. The effects of SRP torques are much more pronounced on HAMR objects. This, combined with their small physical size and mass compared to Envisat and therefore lower gravitational torque, explain why the change in tumbling rate for Envisat cannot be explained by SRP torques alone. The models developed are applicable to HAMR objects at higher altitudes, and need validating with such models.

Further investigation of the effects on HAMR objects is necessary. However, for application to such objects, more information on the physical characteristics is required. This is because the simulations are sensitive to initial conditions and input parameters such as area and moment of inertia.

Ongoing and future work includes:

- Integration of the attitude model with a full force and orbit model
- Shadowing of the SRO from the SRP flux in the Earth umbra and penumbra
- Gravitational torques based on spherical harmonic expansions of the gravity field gradient
- Drag torques based on a statistical mechanics approach
- Inclusion of ERP and TRR models

There are two methods to validating such developments. The first is through analysis of objects known to be tumbling and uncontrolled, such as Envisat and the MSG2 cooler cover. The second method is to use attitude correction data from active missions to compare against the estimated changes in attitude.

VI. Conclusion

Under the torque caused by SRP alone, the period of Envisat changes by 0.3ms, 10.4ms and 0.3ms per day about the x-, y- and z-axis respectively. The observed tumbling of Envisat is partially explained by these results, but as expected there are other effects which require further investigation in order to explain the complete attitude dynamics. These effects include gravitational and drag torques. The discrepancy is explained by the low area-to-mass ratio of Envisat. The application of the models given in this paper are much more important for HAMR objects. The barrier to this is that validation against individual HAMR objects is difficult, owing to their unknown physical characteristics.

A more complete model of the torque and attitude of SROs requires consideration of both gravitational and drag torques. A more accurate model of radiation torques requires modeling of Earth shadowing, Earth radiation pressure (ERP) and thermal re-radiation (TRR) to be included. For application to HAMR debris, more information on the physical characteristics is required in order to apply the models outlined in this paper.

Through modeling the attitude and tumbling of well-observed objects such as Envisat, and validating the models through their observation, we can apply these models to debris to explain their orbital and tumbling dynamics.

Acknowledgments

Effort sponsored by the Air Force Office of Scientific Research, Air Force Material Command, USAF, under grant number FA8655-11-1-3043. The U.S. Government is authorized to reproduce and distribute reprints for Governmental purpose notwithstanding any copyright notation thereon.

References

[1]Schildknecht, T., Musci, R. and Flohrer, T., "Properties of the high area-to-mass space debris population at high altitudes", *Advances in Space Research*, Vol. 41, No. 7, 2008, pp. 1039-1045

[2]Hughes, P. C., *Spacecraft Attitude Dynamics*, Dover, Mineola, New York, 2004.

[3]Albuja, A. A. and Scheeres, D. J., "Defunct Satellites, Rotation Rates and the YORP Effect," *Advanced Maui Optical and Space Surveillance Technologies Conference*,

[4]Liou, J-C., et al. "DebriSat-A Planned Laboratory-Based Satellite Impact Experiment." (2013).

[5]Kelecy, T. and Jah, M., "Analysis of high area-to-mass ratio (HAMR) GEO space object orbit determination and prediction performance: Initial strategies to recover and predict HAMR GEO trajectories with no a priori information". *Acta Astronautica*, Vol. 60, No. 7-8, 2011, pp. 551-558

[6]Kucharski, D. et al., "Attitude and Spin Period of Space Debris Envisat Measured by Satellite Laser Ranging", *IEEE Transactions on Geosciense and Remote Sensing*, Vol. 52, No. 12, 2014, pp. 7651-7656

[7]Ziebart, M., "High precision analytical solar radiation pressure modelling for GNSS spacecraft," Ph.D. Dissertation, School of Computing and Technology, University of East London, 2001.

[8]Ziebart, M., Adhya, S., Sibthorpe, A., Edwards, S., and Cross, P., "Combined radiation pressure and thermal modelling of complex satellites: Algorithms and on-orbit tests," *Advances in Space Research*, Vol. 36, No. 3, 2005, pp. 424–430.

[9] "Satellite Envisat mass & center of gravity history", URL: ftp://ftp.ids-doris.org/pub/ids/satellites/en1mass.txt [cited 2 July 2014]

[10]Bastida Virgili, B., Lemmens, S. and Krag, H., "Investigation on Envisat attitude motion", *ESA e.Deorbit Symposium*, May 2014.

Bibliography

References

[1] "Nasa trl." `www.nasa.gov/content/technology-readiness-level`, retrieved 11/02/16.

[2] NASA, "Orbital debris quarterly newsletter," vol. 18, no. 1, p. 10, 2014.

[3] A. Rossi, "Population models of space debris," in *IAU Colloq. 197: Dynamics of Populations of Planetary Systems* (Z. Knežević and A. Milani, eds.), pp. 427–438, Feb. 2005.

[4] O. Montenbruck and E. Gill, *Satellite Orbits: Models, Methods, and Applications*. Physics and astronomy online library, Springer Berlin Heidelberg, 2000.

[5] T. Schildknecht and A. Hinze, "Long-term evolution of high area-to-mass ratio objects in different orbital regions," in *39th COSPAR Scientific Assembly*, vol. 39 of *COSPAR Meeting*, p. 1718, July 2012.

[6] P. Seitzer, H. Rodriguez-Cowardin, E. Barker, K. Abercromby, G. Foreman, and Horstman M., "Photometric Studies of GEO Debris," in *Advanced Maui Optical and Space Surveillance Technologies Conference*, 2009.

[7] J. Ender, L. Leushacke, A. Brenner, and H. Wilden, "Radar techniques for space situational awareness," in *Radar Symposium (IRS), 2011 Proceedings International*, pp. 21–26, IEEE, 2011.

[8] W. Steven, "A graceful retirement for envisat after 10 years watching over our planet—news— bis," 2012.

[9] E. B. Saff and A. B. J. Kuijlaars, "Distributing many points on a sphere," *The Mathematical Intelligencer*, vol. 19, no. 1, pp. 5–11.

[10] `https://www.kickstarter.com/projects/zacinaction/kicksat-your-personal-spacecraft-in-space`, retrieved 21/02/2016.

[11] "Johnson Space Centre Orbital Debris FAQ." `http://orbitaldebris.jsc.nasa.gov/faqs.html`.

[12] L. I. of Space Policy and Law, *Yearbook on Space Policy 2012/2013: Space in a Changing World*. Springer, 2015.

[13] M. Ziebart, *High Precision Analytical Solar Radiation Pressure Modelling for GNSS Spacecraft*. PhD thesis, University College London, 2001.

[14] T. Kelecy and M. Jah, "Analysis of high area-to-mass ratio (HAMR) GEO space object orbit determination and prediction performance: Initial strategies to recover and predict HAMR GEO trajectories with no a priori information," *Acta Astronautica*, vol. 69, pp. 551–558, Sept. 2011.

[15] ""Satellite Envisat mass and center of gravity history"." `ftp://ftp.ids-doris.org/pub/ids/satellites/en1mass.txt`.

[16] V. Agrawal, *Satellite Technology: Principles and Applications*. Wiley, 2011.

[17] A. Siddiqi, "Sputnik 50 years later: New evidence on its origins," *Acta Astronautica*, vol. 63, no. 14, pp. 529 – 539, 2008.

[18] "Space Launch Report." `http://www.spacelaunchreport.com/`, retrieved 30/5/13.

[19] "UCS Satellite Database." `http://www.ucsusa.org/nuclear_weapons_and_global_security/space_weapons/technical_issues/ucs-satellite-database.html`, retrieved 30/5/13.

[20] E. G. Stansbery, "Growth in the Number of SSN Tracked Orbital Objects," Tech. Rep. 20060022013, NASA Johnson Space Center, Houston, TX, United States, January 2004.

[21] J. N. Pelton, *Space Debris and Other Threats from Outer Space*. Springer, 2013.

[22] D. J. Kessler, "Sources of Orbital Debris and the Projected Environrnent for Future Spacecraft," no. 4.

[23] H. Wirnsberger, O. Baur, and G. Kirchner, "Space debris orbit prediction errors using bistatic laser observations. case study: {ENVISAT}," *Advances in Space Research*, vol. 55, no. 11, pp. 2607 – 2615, 2015.

[24] G. Pupillo, M. Bartolini, G. Cevolani, M. Di Martino, I. Falkovich, A. A. Konovalenko, S. Malevinskij, S. Montebugnoli, A. Nabatov, S. Pluchino, E. Salerno, F. Schillirò, and L. Zoni, "Space debris observational test with the Medicina-Evpatoria bistatic radar.," *Memorie della Societa Astronomica Italiana Supplementi*, vol. 12, p. 44, 2008.

[25] I. Molotov, V. Agapov, V. Titenko, Z. Khutorovsky, Y. Burtsev, I. Guseva, V. Rumyantsev, M. Ibrahimov, G. Kornienko, a. Erofeeva, V. Biryukov, V. Vlasjuk, R. Kiladze, R. Zalles, P. Sukhov, R. Inasaridze, G. Abdullaeva, V. Rychalsky, V. Kouprianov, O. Rusakov, E. Litvinenko, and E. Filippov, "International scientific optical network for space debris research," *Advances in Space Research*, vol. 41, pp. 1022–1028, Jan. 2008.

[26] N. M. Hill, "Measurement of Satellite Impact Test Fragments for Modeling Orbital Debris," *Engineering and Science*, 2009.

[27] a. Houpert, "A space based radar on a micro-satellite for in-situ detection of small orbital debris," *Acta Astronautica*, vol. 44, pp. 313–321, Apr. 1999.

[28] G. Kirchner, F. Koidl, F. Friederich, I. Buske, U. Volker, and W. Riede, "Laser measurements to space debris from Graz SLR station," *Advances in Space Research*, vol. 51, pp. 21–24, Jan. 2013.

[29] H. Kinkrad, *Space Debris: Models and Risk Analysis*. Springer-Praxis, 2006.

[30] "UK Parliament POSTnote: Space Debris," March 2010.

[31] "Space situational awareness satellite program announcement." `http://www.af.mil/News/ArticleDisplay/tabid/223/Article/473403/shelton-announces-new-space-situational-awareness-satellite-program.aspx`, retrieved 11/02/16.

[32] N. Bobrinsky and L. Monte, "The space situational awareness program of the European Space Agency," *Cosmic Research*, vol. 48, pp. 392–398, Oct. 2010.

[33] T. Donath, T. Schildknecht, V. Martinot, and L. D. Monte, "Possible european systems for space situational awareness," *Acta Astronautica*, vol. 66, no. 9â10, pp. 1378–1387, 2010.

[34] L. Innocenti, T. Soares, and J. Delaval, "ESA Clean Space Initiative," in *6th European Conference on Space Debris*, vol. 723 of *ESA Special Publication*, p. 4, Aug. 2013.

[35] Biesbroek, R., Soares, T., Huesing, J., Wormnes, K., Innocenti, L., "The e.Deorbit CDF Study: A design study for the safe removal of a large space debris," in *64rd International Astronautical Congress (IAC) Beijing*, ESA Special Publication, 2013.

[36] H. Klinkrad, *Space debris models and risk analysis*. Berlin New York Chichester, UK: Springer Published in association with Praxis Pub, 2006.

[37] D. J. Kessler and B. G. Cour-Palais, "Collision frequency of artificial satellites: The creation of a debris belt," *Journal of Geophysical Research: Space Physics*, vol. 83, no. A6, pp. 2637–2646, 1978.

[38] A. M. Bradley and L. M. Wein, "Space debris: Assessing risk and responsibility," *Advances in Space Research*, vol. 43, no. 9, pp. 1372 – 1390, 2009.

[39] C. Fruh, "Characterisation of space debris objects via orbital data and light curves," in *Proceedings of the 6th European Conference on Space Debris*, 2013. 6th European Conference on Space Debris, ESA ESOC Darmstadt, April 2013.

[40] M. Ziebart, "Generalised analytical solar radiation presure modelling algorithm for spacecraft of complex shape," *Journal of Spacecraft and Rockets*, vol. 41, no. 5, pp. 840–849, 2004.

[41] M. Ziebart, S. Adhya, A. Sibthorpe, S. Edwards, and P. Cross, "Combined radiation pressure and thermal modelling of complex satellites: Algorithms and on-orbit tests," *Advances in Space Research*, vol. 36, no. 3, pp. 424 – 430, 2005.

[42] S. Adhya, *Thermal Re-Radiation Modelling for the Precise Prediction and Determination of Spacecraft Orbits*. PhD thesis, University College London, 2005.

[43] A. J. Sibthorpe, *Precision Non-Conservative Force Modelling For Low Earth Orbiting Spacecraft*. PhD thesis, University College London, 2006.

[44] T. Schildknecht, R. Musci, M. Ploner, G. Beutler, W. Flury, J. Kuusela, J. de Leon Cruz, and L. de Fatima Dominguez Palmero, "Optical observations of space debris in {GEO} and in highly-eccentric orbits," *Advances in Space Research*, vol. 34, no. 5, pp. 901 – 911, 2004. Space Debris.

[45] C. Früh and T. Schildknecht, "Investigation of Properties and Characteristics of High-Area-to-Mass- Ratio Objects Based on Examples of Optical Observation Data of Space Debris Objects in GEO-like Orbits," in *Advanced Maui Optical and Space Surveillance Technologies Conference*, p. E7, Sept. 2010.

[46] M. H. Kaplan, *Modern Spacecraft Dynamics and Control*. Wiley, 1976.

[47] Curtis, *Orbital Mechanics for Engineering Students 3rd Edition*. Elsevier, 2014.

[48] T. S. Kelso, "Validation of sgp4 and is-gps-200d against gps precision ephemerides," in *Proceedings of 2007/02: AAS/AIAA Spaceflight Mechanics Meeting*, Feb 2007.

[49] W. Ting and H. Hai, "Estimating Orbital Lifetime of Space Objects from Two-Line Elements." `http://wangting.org/pages/papers/lifetime.pdf`.

[50] a. Rossi, L. Anselmo, a. Cordelli, P. Farinella, and C. Pardini, "Modelling the evolution of the space debris population," *Planetary and Space Science*, vol. 46, pp. 1583–1596, Nov. 1998.

[51] G. E. Pollock, J. W. Gangestad, and J. M. Longuski, "Analytical solutions for the relative motion of spacecraft subject to lorentz-force perturbations," *Acta Astronautica*, vol. 68, no. 1, pp. 204–217, 2011.

[52] N. Praly, M. Hillion, C. Bonnal, J. Laurent-Varin, and N. Petit, "Study on the eddy current damping of the spin dynamics of space debris from the Ariane launcher upper stages," *Acta Astronautica*, vol. 76, pp. 145–153, July 2012.

[53] N. K. Pavlis, S. A. Holmes, S. C. Kenyon, and J. K. Factor, "The EGM2008 Global Gravitational Model," *AGU Fall Meeting Abstracts*, p. A1, Dec. 2008.

[54] E. M. Standish, Jr., "The observational basis for JPL's DE 200, the planetary ephemerides of the Astronomical Almanac," *Astronomy and Astrophysics*, vol. 233, pp. 252–271, July 1990.

[55] J. R. Wertz and W. J. Larson, *Space mission analysis and design.* Springer, New York, 1999.

[56] P. C. Hughes, *Spacecraft Attitude Dynamics.* Wiley and sons, 1986.

[57] D. A. Vallado, *Fundamentals of Astrodynamics and Applications.* Microcosm Press/Springer, 2007.

[58] V. A. Chobotov, *Spacecraft Attitude Dynamics and Control.* Krieger publishing, 1991.

[59] D. Hastings and H. Garrett, *Spacecraft-Environment Interactions (Cambridge Atmospheric and Space Science Series).* Cambridge University Press, 2004.

[60] H. Cowardin, K. Abercromby, E. Barker, P. Seitzer, M. Mulrooney, and T. Schildknecht, "An Assessment of GEO Orbital Debris Photometric Properties Derived from Laboratory-Based Measurements," in *Advanced Maui Optical and Space Surveillance Technologies Conference*, p. E25, 2009.

[61] J. P. Loftus, "Orbital Debris : A Chronology," *Program*, no. January, 1999.

[62] M. a. Skinner, R. W. Russell, R. J. Rudy, D. J. Gutierrez, D. L. Kim, K. Crawford, S. Gregory, and T. Kelecy, "Time-resolved infrared spectrophotometric observations of high area to mass ratio (HAMR) objects in GEO," *Acta Astronautica*, vol. 69, pp. 1007–1018, Dec. 2011.

[63] R. Jehn, S. Ariafar, T. Schildknecht, R. Musci, and M. Oswald, "Estimating the number of debris in the geostationary ring," *Acta Astronautica*, vol. 59, pp. 84–90, July 2006.

[64] C. Früh and T. Schildknecht, "Variation of the area-to-mass ratio of high area-to-mass ratio space debris objects," *Monthly Notices of the Royal Astronomical Society*, vol. 419, no. 4, pp. 3521–3528, 2012.

[65] G. Beutler, *Methods of celestial mechanics*. Berlin New York: Springer, 2005.

[66] P. Anz-Meador and A. Potter, "Density and mass distributions of orbital debris," *Acta Astronautica*, vol. 38, no. 12, pp. 927 – 936, 1996.

[67] H. Boehnhardt, H. Koehnhke, and A. Seidel, "The acceleration and the deceleration of the tumbling period of rocket intercosmos 11 during the first two years after launch," *Astrophysics and Space Science*, vol. 162, no. 2, pp. 297–313, 1989.

[68] V. Williams and A. Meadows, "Eddy current torques, air torques, and the spin decay of cylindrical rocket bodies in orbit," *Planetary and Space Science*, vol. 26, no. 8, pp. 721 – 726, 1978.

[69] Z. Zhongping, Y. Fumin, Z. Haifeng, W. Zhibo, C. Juping, and L. Pu, "The Experiment and results of Laser Ranging to Space Debris," no. 17912, pp. 2–9.

[70] J. W. Creshaw and P. M. Fitzpatrick, "Gravity effects on the rotational motion of a uniaxial artificial satellite.," *AIAA Journal*, vol. 6, pp. 2140–2145, Nov. 1968.

[71] L. M. L. Juan F. San-Juan and R. Lopez, "Higher-order analytical attitude propagation of an oblate rigid body under gravity-gradient torque," *Mathematical Problems in Engineering*, 2012.

[72] D. Scheeres, A. Rosengren, and J. Mcmahon, "The dynamics of high area-to-mass ratio objects in earth orbit: the effect of solar radiation pressure," *Spaceflight Mechanics*, vol. 140, 2011.

[73] J. P. Loftus, "U.S. Studies in Orbital Debris," *Acta Astronautica*, vol. 24, pp. 333–341, 1991.

[74] H. Yoshida and M. Araki, "Social impact of space debris. Study of economic and political aspects," *Acta Astronautica*, vol. 34, pp. 345–355, 1994.

[75] C. Wiedemann, M. Oswald, J. Bendisch, H. Sdunnus, and P. Vörsmann, "Cost and benefit analysis of space debris mitigation measures," *Acta Astronautica*, vol. 55, pp. 311–324, Aug. 2004.

[76] L. Anselmo and C. Pardini, "Dynamical evolution of high area-to-mass ratio debris released into GPS orbits," *Advances in Space Research*, vol. 43, pp. 1491–1508, May 2009.

[77] L. Anselmo and C. Pardini, "Long-term dynamical evolution of high area-to-mass ratio debris released into high earth orbits," *Acta Astronautica*, vol. 67, pp. 204–216, July 2010.

[78] A. Langwost, H. Sdunnus, D. Gunia, G. Drolshagen, J. Soerensen, and S. Hauptmann, "Presentation of the PC Version of the Esabase/debris Impact Analysis Tool," in *4th European Conference on Space Debris* (D. Danesy, ed.), vol. 587 of *ESA Special Publication*, p. 619, Aug. 2005.

[79] K. Bunte, A. Langwost, and G. Drolshagen, "The recent upgrade and future perspectives of the ESABASE/Debris tool," *Advances in Space Research*, vol. 34, pp. 1130–1135, Jan. 2004.

[80] C. Martin, J. Cheeses, N. Sanchez-Ortiz, H. Klinkrad, K. Bunte, S. Hauptmann, B. Fritsche, and T. Lips, "Introducing the esa drama tool," *Science and Technology Series*, vol. 110, pp. 219–233, 2005.

[81] T. Flohrer, H. Krag, and H. Klinkrad, "Esaâs process for the identification and assessment of high-risk conjunction events," *Advances in Space Research*, vol. 44, no. 3, pp. 355–363, 2009.

[82] J. Gelhaus, S. Flegel, M. Möckel, C. Wiedemann, S. Stabroth, M. Oswald, H. Krag, H. Klinkrad, and P. Vörsmann, "Validation of the esa-master-2009 space debris population," in *61st IAC Conference, Czech Republic*, vol. 4, p. 2996, 2010.

[83] P. H. Krisko and S. Flegel, "Ordem 3.0 and master-2009 modeled small debris population comparison," in *6th European Conference on Space Debris*, 2012.

[84] H. Lewis, G. Swinerd, N. Williams, and G. Gittins, "Damage: a dedicated geo debris model framework," in *Proceedings of the Third European Conference on Space Debris*, no. 473, pp. 373–378, The European Space Agency (ESA), 2001.

[85] H.-s. Sim and K.-h. Kim, "Reentry survival analysis of tumbling metallic hollow cylinder," *Advances in Space Research*, vol. 48, no. 5, pp. 914–922, 2011.

[86] H.-Y. Lin and C.-Y. Zhao, "Evolution of the rotational motion of space debris acted upon by eddy current torque," *Astrophysics and Space Science*, vol. 357, p. 167, June 2015.

[87] J. Andres, R. Noomen, G. Bianco, D. Currie, and T. Otsubo, "The Spin Axis Behavior of The Lageos Satellites," in *EGS General Assembly Conference Abstracts* (A. Tzanis, ed.), vol. 27 of *EGS General Assembly Conference Abstracts*, 2002.

[88] J. I. Andres, R. Noomen, G. Bianco, D. G. Currie, and T. Otsubo, "Spin axis behavior of the lageos satellites," *Journal of Geophysical Research: Solid Earth*, vol. 109, no. B6, pp. n/a–n/a, 2004. B06403.

[89] J. E. Cochran, "Effects of gravity-gradient torque on the rotational motion of a triaxial satellite in a precessing elliptic orbit," *Celestial mechanics*, vol. 6, no. 2, pp. 127–150, 1972.

[90] V. A. Sarychev, "Influence of the earth's oblateness on the rotational motion of an artificial satellite," *Planetary Space Science*, vol. 8, pp. 173–178, Dec. 1961.

[91] H. Klinkrad and B. Fritsche, "Orbit and attitude perturbations due to aerodynamics and radiation pressure," in *ESA Worskhop on Space Weather*, 1998.

[92] R. Kanzler, T. Schildknecht, T. Lips, B. Fritsche, J. Silha, and H. Krag, "Space Debris Attitude Simulation - IOTA (In-Orbit Tumbling Analysis)," in *Advanced Maui Optical and Space Surveillance Technologies Conference*, p. 33, 2015.

[93] P. Karrang, B. Fritsche, R. Kanzler, and S. Lemmens, "First results of IOTA (In-Orbit Tumbling Analysis)," in *Sixth International Conference on Astrodynamics Tools and Techniques*, 2016.

[94] P. Bargellini, M. A. Garcia Matatoros, L. Ventimiglia, and D. Suen, "Envisat Attitude and Orbit Control In-Orbit Performance: AN Operational View," in *Guidance, Navigation and Control Systems*, vol. 606 of *ESA Special Publication*, p. 52.1, Jan. 2006.

[95] "Condor service improvements - ucl research computing." `http://blogs.ucl.ac.uk/research-computing/category/condor/`, retrieved 11/02/16.

[96] L. F. B Somodi, "Accuracy of numerical integration techniques for goce orbit determination," EDIS - Publishing Institution of the University of Zilina.

[97] O. Montenbruck, "Numerical integration methods for orbital motion," *Celestial Mechanics and Dynamical Astronomy*, vol. 53, no. 1, pp. 59–69, 1992.

[98] R. Zwanenburg, "The qualification test programme of the ENVISAT solar array mechanism," in *6th European Space Mechanisms and Tribology Symposium* (W. R. Burke, ed.), vol. 374 of *ESA Special Publication*, p. 65, Aug. 1995.

[99] S. Lemmens, H. Krag, J. Rosebrock, and I. Carnelli, "Radar Mappings of Attitude Analysis of Objects in Orbit," in *6th European Conference on Space Debris*, vol. 723 of *ESA Special Publication*, p. 20, Aug. 2013.

[100] D. Kucharski, G. Kirchner, F. Koidl, C. Fan, R. Carman, C. Moore, A. Dmytrotsa, M. Ploner, G. Bianco, M. Medvedskij, *et al.*, "Attitude and spin period of space debris envisat measured by satellite laser ranging," *Geoscience and Remote Sensing, IEEE Transactions on*, vol. 52, no. 12, pp. 7651–7657, 2014.

[101] H. Helvajian and S. Janson, *Small Satellites: Past, Present, and Future*. AIAA, 2009.

[102] S. Kawamoto, T. Makida, F. Sasaki, Y. Okawa, and S. Nishida, "Precise numerical simulations of electrodynamic tethers for an active debris removal system," *Acta Astronautica*, vol. 59, no. 1â5, pp. 139–148, 2006.

[103] C. Finlay, S. Maus, C. Beggan, T. Bondar, A. Chambodut, T. Chernova, A. Chulliat, V. Golovkov, B. Hamilton, M. Hamoudi, *et al.*, "International geomagnetic reference field: the eleventh generation," *Geophysical Journal International*, vol. 183, no. 3, pp. 1216–1230, 2010.

[104] A. Juhasz and M. Horanyi, "Dynamics of charged space debris in the earth's plasma environment," *Journal of Geophysical Research: Space Physics*, vol. 102, no. A4, pp. 7237–7246, 1997.

[105] G. E. Pollock, J. W. Gangestad, and J. M. Longuski, "Analytical solutions for the relative motion of spacecraft subject to lorentz-force perturbations," *Acta Astronautica*, vol. 68, no. 1, pp. 204–217, 2011.

[106] Y. A. Abdel-Aziz and K. I. Khalil, "Electromagnetic effects on the orbital motion of a charged spacecraft," *Research in Astronomy and Astrophysics*, vol. 14, no. 5, p. 589, 2014.

[107] E. C. Whipple, "Potentials of surfaces in space," *Reports on Progress in Physics*, vol. 44, no. 11, p. 1197, 1981.

[108] C. R. Clauer and E. Friis-Christensen, "High-latitude dayside electric fields and currents during strong northward interplanetary magnetic field - Observations and model simulation," , vol. 93, pp. 2749–2757, Apr. 1988.

[109] S. T. Lai, *Fundamentals of Spacecraft Charging: Spacecraft Interactions with Space Plasmas*. Princeton University Press, 2011.

[110] C. Finlay, S. Maus, C. Beggan, M. Hamoudi, F. Lowes, N. Olsen, and E. Thébault, "Evaluation of candidate geomagnetic field models for igrf-11," *Earth, planets and space*, vol. 62, no. 10, pp. 787–804, 2010.

[111] W. Jones, *The Design and Simulated Performance of the Attitude Determination and Control System of a Gravity Gradient Stabilized Cube Satellite*. Lulu.com, 2015.

[112] C. McCullough, S. Bettadpur, and K. McDonald, "Accuracy of Numerical Algorithms for Satellite Orbit Propagation and Gravity Field Determination," *Journal of Spacecraft and Rockets*, vol. 52, pp. 766–775, May 2015.

[113] N. Tsyganenko and M. Sitnov, "Modeling the dynamics of the inner magnetosphere during strong geomagnetic storms," *Journal of Geophysical Research (Space Physics)*, vol. 110, p. A03208, Mar. 2005.

[114] "Space Debris: Isolation of Humankind?: Hira Virdee at TEDxUCL." `http://www.youtube.com/watch?v=fbPgRYIzKzo`, retrieved 24/3/14.

[115] H. S. Virdee, S. Grey, S. Bhattarai, and M. Ziebart, "Non-conservative torque and attitude modelling for enhanced space situational awareness," *American Institute of Aeronautics and Astronautics*, Aug 2014.